Durham E-Theses

Understanding the Growth and Formation of Synthetic Diamond

COLLINS, JACK

How to cite:

Use policy

Understanding the Growth and Formation of Synthetic Diamond

Jack Collins

A Thesis for the Degree of Master of Philosophy

Department of Chemistry

Durham University

December 2023

ABSTRACT

Since ancient times, diamond and its associated properties have inspired both intrigue and fascination. For much of this time, the only source of diamond has been those mined out of the ground, meaning limited or restricted access for many. However, as recently as 70 years ago, it was determined that diamond can be successfully synthesised from the much more mundane graphite, opening a multitude of synthetic possibilities.

Over the course of this report, the current knowledge of diamond's properties and its synthesis at high pressure and high temperature is reviewed, in addition to the properties of graphite. Thermodynamic and kinetic considerations for the formation of diamond are also discussed, as well as the spectroscopic analysis of both diamond and graphite. The synthesis, structure and physical properties of different crystallographic diamond defects are also explored.

Following this, a new type of high pressure, high temperature apparatus for the manufacture of diamond-based materials is discussed, with a particular emphasis on the formation of poly-crystalline diamond composites. Exploration of the high-performance materials that allow this design to efficiently function under the extremely harsh conditions required for diamond synthesis is also undertaken, with a focus on the synthesis of carbon-fibre carbon frameworks. Finally, in light of the results obtained, future research surrounding the understanding of diamond formation, as well as the material considerations of this new approach is outlined.

CONTENTS

DECLARATION

The work outlined within this thesis is based on research carried out at the Department of Chemistry, Durham University, Durham, England; and Dyman Advanced Materials, Sedgefield, England. Throughout the period between October 2019 and January 2023, this project was financially supported by the European Regional Development Fund (ERDF), and was academically and industrially supervised by Dr Karen E. Johnston and Dr Gary Gibson, respectively. No part of this thesis has been submitted elsewhere for any other degree or qualification and it is all my own work unless referenced to the contrary in the text.

COPYRIGHT

LIST OF ABBREVIATIONS

Abbreviation	Definition
AS	Amorphous Silica
AV	Acceleration Voltage
BSE	Back Scattered Electron
C.C.	Carbocation
CCP	Cubic Close Packed
CF	Carbon-Fibre
CFC	Carbon-Fibre Reinforced Carbon
CL	Cross-Linking
Co-MU	Co-doped Mullite Species
CPI	Centre for Process Innovation
CR	Cristobalite
CVD	Chemical Vapour Deposition
DSC	Differential Scanning Calorimetry
EAS	Electrophilic Aromatic Substitution
EDX	Energy Dispersive X-ray Spectroscopy
EPR	Electron Paramagnetic Resonance
ERDF	European Regional Development Fund
EWG	Electron Withdrawing Group
FTIR	Fourier Transform Infra-Red Spectroscopy
GPC	Gel Permutation Chromatography
HMP	Hydroxymethyl-Phenol
HTHP	High Temperature, High Pressure
IBM	Ion Beam Milling
IPA	Isopropyl Alcohol
IR	Infra-Red
MS	Mass Spectrometry
MU	Mullite
NMR	Nuclear Magnetic Resonance

PCD	Polycrystalline Diamond
PCD-a	Polycrystalline Diamond Sample A
PCD-b	Polycrystalline Diamond Sample B
PCD-c	Polycrystalline Diamond Sample C
PXRD	Powder X-ray Diffraction
RC-a	Reaction Chamber used to synthesise PCD-a
RC-b	Reaction Chamber used to synthesise PCD-b
RC-c	Reaction Chamber used to synthesise PCD-c
RC-u	Unused Reaction Chamber
SE	Secondary Electrons
SEM	Scanning Electron Microscopy
SIMS	Secondary Ion Mass Spectrometry
TEC	Thermal Expansion Coefficient
TGA	Thermogravimetric Analysis
TMF	Thin Metal Film
TR	Thermoset Resins
UTS	Ultimate Tensile Strength
WD	Working Distance

Acknowledgements

1 INTRODUCTION AND BACKGROUND

1.1 DIAMOND

1.1.1 The History of Diamond

'Diamond is the most valuable, not only of the precious stones, but of all things in this world'

– Roman Naturalist Pliny the Elder, *c.* 1st Century CE[1]

Diamond has been used and studied extensively since ancient times, with records from India (where it is believed that diamonds were first mined) dating back at least 3000 years to the 1st century BCE.[2] The earliest confirmed use of diamonds was on axes in China, dating to around 4000 BCE.[3] The ancients sought out this precious stone for use in jewellery, primarily due to its lustre, as well as an engraver, owing to its incredible hardness.[4] Since the time of the Romans, diamond has been highly prised, and is often associated with the wealthy. For example, diamonds such as the Cullinan, the largest cut diamond in the world, are used by British monarchs as a vibrant display of power and wealth.

The Roman naturalist Pliny the Elder wrote about diamonds as early as the 1st century CE, and noted its extreme hardness. In the final of his books, he gave a comprehensive description of 'the six types of diamond' and their uses, as well as a detailed account of Indian diamonds octahedral crystal structure.[4] Even in modern times, its uses have varied little since these publications were first produced, and the fascination of this minerals beauty and toughness still persists.

1.1.2 The Structure of Diamond

Polymorphism is the ability of a material to adopt multiple crystal structures. Diamond is known to have two different polymorphs. When referring to diamond, it is typically the cubic structure, also known as 3C diamond that is referred to (Figure 1(a)).[5] The second known polymorph is that of hexagonal diamond, which is denoted as 2H diamond, or lonsdalite (Figure 1(b)).[6] Whilst the structure, formation and properties of 2H diamond are fascinating, the focus here is on the structure and synthesis of 3C cubic

diamond. The structure of 3C diamond is very well known and understood. In fact, cubic diamond was one of the first crystal structures to be determined via X-ray diffraction.[7]

The atomic structure of 3C diamond can be visualised in a variety of different ways. For example, a common description of the diamond lattice considers planes of interlocking six-membered carbon rings. The cubic, 3C polymorph is comprised of these inter-locking hexagonal rings in a chair conformation, which form sheets along the [100] crystallographic plane and repeat every three layers (hence the term '3'-C). These sheets are then connected by more hexagonal rings in a chair conformation, which run in the [111] plane. This results in 3C diamond being structurally identical when viewed along all three spatial dimensions. Moreover, the chair conformation exhibited by the inter-planar hexagonal rings is what distinguishes 3C diamond from hexagonal 2H diamond. In hexagonal diamond, the inter-planar hexagonal rings are present in a boat conformation.

Alternatively, the diamond structure can be thought of as two inter-penetrating cubic close packed (CCP) lattices, with the atoms of one lattice occupying the tetrahedral voids of the other, as demonstrated in Figure 2.[5] The faces of these tetrahedra run along the [111] lattice plane, which also happens to be the natural cleavage plane of diamond, whereby fracture of the crystal is most favourable. Moreover, the [111] crystallographic plane of 3C diamond is identical to that formed by the CCP array of alternating atoms present in the ABC stacking of 3R graphite. This relationship between the two lattices is of great importance when synthesising diamond, and, as such, will be explored in greater detail.
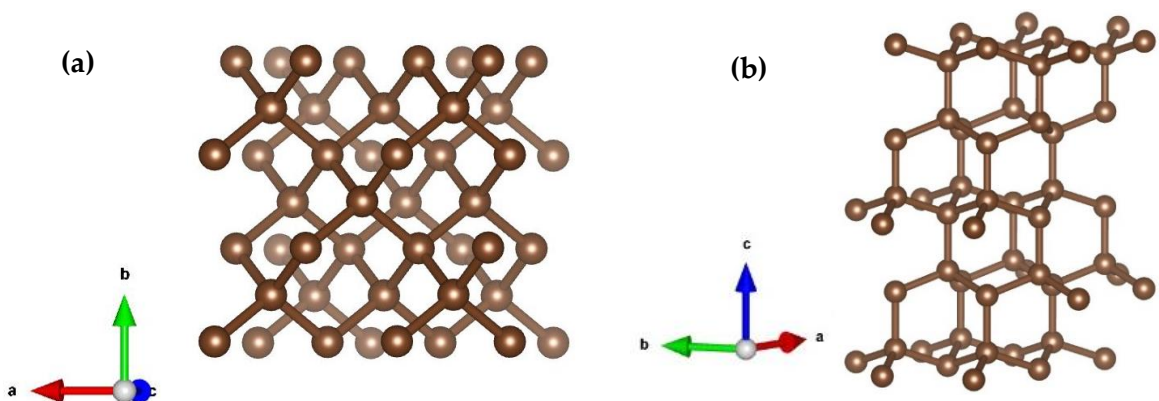
Figure 1: The crystal structure of (a) cubic (3C) diamond, and (b) hexagonal (2H) diamond.[6]

1.1.3 Properties of Diamond

Aside from its physical beauty, there are many other properties of diamond that spark considerable interest. For example, its high refractive index (2.41), as well as its optical transparency to light with a wavelength greater than 225 nm which, when combined, cause the famous sparkle of diamonds cut specifically for use in jewellery. Other notable properties include its incredible hardness and chemical inertness. The hardness of diamond is well documented, with diamond having long been considered to be the hardest known material, until recent speculation that carbon nitride may be harder.[8,9] The Mohs scale of mineral hardness places diamond at the top, giving it the maximum score of 10, meaning it can scratch every other crystal without being scratched itself. This is reflected in its very high Young's modulus (1050 GPa).

Other desirable properties of diamond include a small thermal expansion coefficient (TEC) of $1.2 \times 10^{-6}\,\mathrm{K^{-1}}$, as well as a thermal conductivity of around 20 W cm^{-1} K^{-1}, which is incredibly high for an electrical insulator with a breakdown electric field strength of 10^7 V cm^{-1}, and a band gap of 5.4 eV. This makes it suitable for high intensity electrical insulator applications, where high heat and high voltage would pose issues for other conventional insulators.[10]

A lesser known property of diamond is its incredibly high Debye temperature of 2,200 K. Below this temperature, quantum effects can start to be observed. Graphite, by comparison, has a Debye temperature of only 400 K.[11] Hence, some phenomena manifest
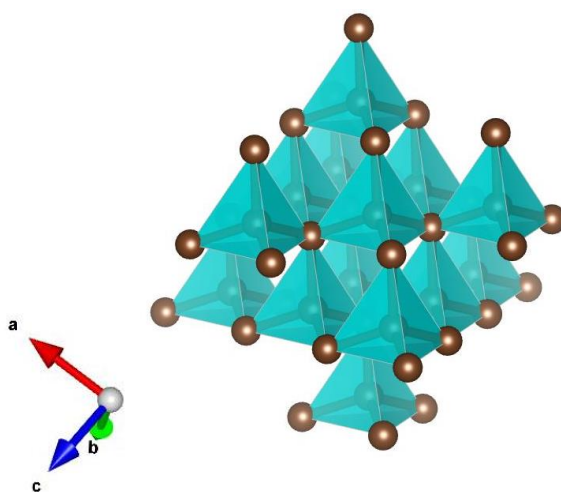
Figure 2: A polyhedral model of diamond. The corners of each tetrahedron form a CCP array of atoms, whilst the atoms in the middle of the voids form their own, separate CCP array.[5]

themselves in diamond that for other materials would have to be cooled in order for them to be observed. It is this selection of properties that make diamond such a sought-after material. These properties arise owing to a number of factors, including its crystal structure, the synthetic method used in its production, as well as any defects that may be present in the crystal.

1.2 DEFECTS AND IMPURITIES IN DIAMOND

A very important aspect of both natural and synthetic diamond is that of any impurities present, as these can impart interesting physical properties into the crystal, *e.g.,* differing colours or electrical conductivities. These tend to be easily identified and analysed as all known impurities, other than hydrogen, have characteristic spectroscopic features.[12] Impurities are also incorporated into the growing diamond crystal at different concentrations, depending on the growth conditions and crystallographic domain, and are thus able to provide information regarding how the diamond has grown during the crystallisation process.[13] Nitrogen and boron are by far the most common impurities in both synthetic and natural diamond. It is noted that whilst hydrogen is a major impurity in chemical vapour deposition (CVD) produced diamond, its occurrence in samples formed under high temperatures and high pressures is extremely rare, and is therefore not discussed in any detail.

1.2.1 Nitrogen

Nitrogen is an extremely common defect in both synthetic and natural diamond. Usually, when present in concentrations of 50 – 500 ppm, this causes the diamond to exhibit a yellow colour. However, this colour fades with heat treatment above 1500 °C.[12] Nitrogen impurities can take 3 major forms, known as A-, B- and C-centres, along with a variety of nitrogen-vacancy defects, such as the N3 centre. Kinetic studies performed on the process of converting one type of defect to another, known as annealing, demonstrated that the A-, B- and N3- centres are aggregates, containing more than 1 nitrogen atom.[14,15] The most common form present in high temperature, high pressure (HTHP) diamond is the C-centre, whilst natural diamonds typically contain a mixture of A and B-centres, with small amounts of N3 also present.

The intentional doping of diamond with nitrogen can have many benefits. Since nitrogen has one extra electron when compared to carbon, it can act as a 'deep donor', producing a donor energy level within the electronic band gap. However, it is noted that it can be challenging to achieve such doping, with the highest concentration of nitrogen dopant achieved using metal catalysts at HTHP conditions topping out at ~800 ppm. By comparison, natural diamonds can have upwards of 1000 ppm of nitrogen present, although non-metallic catalysts such as Na_2SO_4 have been used to synthesise diamonds with concentrations in excess of this.[12] The main influence for the amount of free nitrogen available depends on its solubility in any potential surrounding matrix whilst the diamond is forming, and whether there are nitrogen 'getters' present.[13] Interestingly, the growth temperature can also influence the rate of nitrogen uptake in the growing crystal. Provided no nitrogen reactive species are present in the growth cell, the concentration of nitrogen will decrease as the synthesis temperature increases. If these are present in the growth medium, this trend will reverse.[12] Another interesting observation is that the uptake of nitrogen into the crystal structure is non-homogeneous, with experiments showing that the [111] face takes up the most.[12]

It is noted that the precise properties of the nitrogen defect vary depending on the type of centre that is present. These centres differ in structure, with this difference having a knock-on effect in its characteristics. Specific details of the different centres are discussed in the following sections.

1.2.1.1   A-Centre

This defect is most commonly found in natural diamonds, with examples containing nitrogen present in predominantly A-centres being known as Type IaA diamond. The centre itself consists of a pair of neutral, nearest neighbour nitrogen atoms,[16] which are of trigonal symmetry (Figure 3).[17,18] These substitute for carbon within the lattice framework.[17] This produces an absorption peak in the UV/vis spectrum at 310 nm, and is therefore invisible to the naked eye. If coloured diamonds are annealed at temperatures between 1500 and 2000 °C, then any nitrogen present will aggregate into A-centre pairs, and hence will lose their colour. This process is generally sped up by presence of vacancies.[12,19] This is why natural diamonds, despite containing up to 1000 ppm of nitrogen, are colourless, as they have been heated in the earth's crust. The
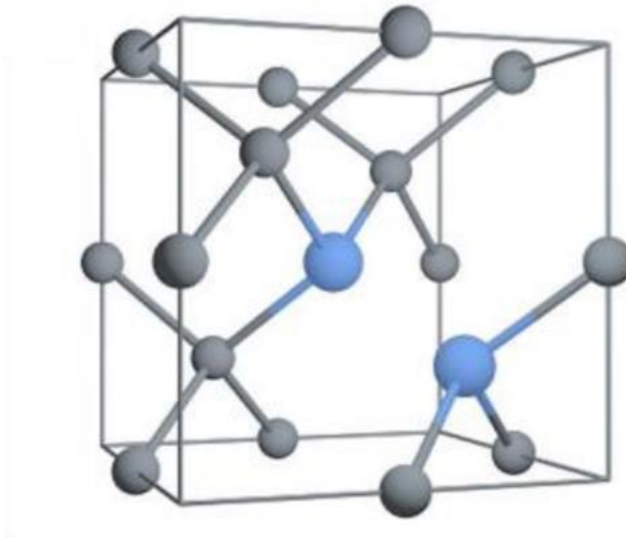
Figure 3: The crystal structure of the nitrogen A-centre within a diamond unit cell.[18]

presence of A-centred nitrogen defects in diamond has also been shown to reduce thermal conductivity.

Unlike B- and C-centres, A-centres produce no sharp IR peaks, although a broad peak is observed at 1282 cm^{-1}. When studying diamond defects, this is often considered to be characteristic of the A-centre, and can further be used to determine the concentration of the defect within the crystal.[20,21] Under standard conditions, the A-centre is diamagnetic, and therefore inactive to techniques such as electron paramagnetic resonance (EPR) spectroscopy.[17] However, it can be ionised, either using light with a wavelength less than 415 nm, or via the addition of deep acceptors into the diamond lattice.[22] In doing so, the double bond between the two nitrogen atoms becomes ionized, giving a single bond along with an unpaired electron present in the anti-bonding orbital between the two atoms.[16] In turn, this results in the centre becoming EPR active. Such a system is analogous to the nitrogen-carbon structure found in the C-centre defect, and possesses C$_{3v}$ symmetry along the nitrogen-nitrogen axis, which can be used to prove the N=N structure.[16]

1.2.1.2   B-Centre

At present, the structure of the B-centre defect remains somewhat of a mystery. However, it is generally believed to consist of a carbon vacancy surrounded by substituting nitrogen atoms, although there's currently no spectroscopic data to corroborate this (Figure 4).[18,23,24] Diamonds containing a majority of this defect are

15

referred to as Type IaB. This type of defect does not produce any colour and no UV/vis absorptions can be attributed to it.[25] Instead, the presence of this defect can be easily determined from a sharp IR peak at 1332 cm⁻¹, along with another broader feature at 1280 cm⁻¹, as well as during EPR experiments.[26,27]

1.2.1.3   C-Centre

Commonly referred to as 'canary diamonds' due to the yellow colour they impart on the crystal, the C-centre is the most common defect in synthetic HTHP diamonds. Those with a majority of this defect are labelled as Type Ib, and as little as 1 nitrogen atom per 100,000 carbon atoms, or 10 ppm, can produce the yellow colour.[12] Here, the nitrogen is present as an isolated atom that substitutes for a carbon atom within the lattice (Figure 5).[18] The yellow colour arises when light with energy greater than 2.2 eV excites electrons from the valence band into the conduction band.[28] Spectroscopically, this defect is easily identified. A sharp IR peak at 1344 cm⁻¹, as well as a broad peak at 1130 cm⁻¹, can be used to determine the presence of C-centre defects. Their presence and structure can also be determined via EPR experiments.[26]

The spectrum obtained for C-centre defects via EPR experiments is easily rationalised. Carbon, having 4 valence electrons, covalently bonds with 4 other carbon atoms oriented in [111] lattice plane.[26] Nitrogen, however, has 5 valence electrons, two of which form a lone pair. This means that a substituting nitrogen atom forms a covalent bond with 3 surrounding carbon atoms, with the bond between the fourth carbon atom
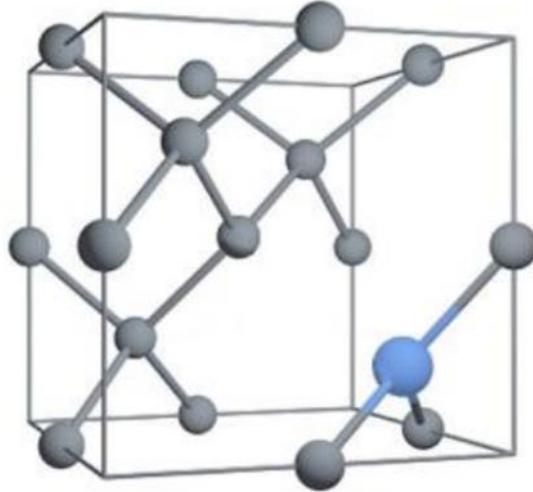
being occupied by the nitrogen lone pair. Hence, this results in the electron contributed by the carbon atom being unpaired in the anti-bonding orbital.[26] Experimentally, this is verified by EPR measurements, which demonstrate that the unpaired electron present in the C-centre defect is found on this carbon atom 67% of the time.[29]

In addition, by adding acceptor defects, such as boron or nickel, into the diamond lattice, the C-centre can become ionised. This forms a C^+ centre, which acts as a deep donor.[27,30] The C^+ defect is also IR active, with the main peak at 1332 cm^{-1}, along with broader, weaker peaks at 1115, 1046 and 950 cm^{-1}.[27]

1.2.2 Boron

Another important diamond dopant is boron, found in Type IIb diamond. Due to it having one less electron than carbon, it is able to act as a 'deep acceptor' by creating an electron hole, and by extension shows p-type semi-conducting abilities.[12] Boron present on its own imparts a blue colour to the crystal, which arises because the holes allow the absorption of low energy red light.[23] However, if the boron is present with a donor atom, such as nitrogen, the diamond will be colourless. This is because the donor atom will fill the electron hole, thereby preventing the absorption of red light.[12] Moreover, these holes can move under the influence of an external electric field, making the diamond electrically conductive. A boron:carbon ratio of only 1:1,000,000 can allow this to occur. As with nitrogen, the inclusion of boron into the lattice is non-homogeneous, and varies with growth area. Here, the [110] face is the most sensitive, whilst the [111] face is the

least sensitive. Extensively boron-doped MPCVD-grown (Microwave Plasma Chemical Vapour Deposition) polycrystalline diamond layers were observed to have a superconducting character depending exclusively on the growth time, *i.e.*, grown under identical experimental conditions.[32]

1.2.3   Classifications of Diamond

Diamonds, particularly those destined for the gem market, can be classified into four different groups depending on the type of impurities present. Type I diamonds are those that contain nitrogen, with these being further divided based on whether the nitrogen defect present is an A-, B- or C-centre defect (*vide supra*). Those containing A- and B-centres are classed as Type Ia. This comprises around 98% of natural diamond, which, for the most part, are colourless. If C-centres are present, then the gem is designated as Type Ib. These are often known as canary diamonds due to their yellow colouration, and includes most HTHP synthetic diamond (Figure 6).[12]

The second category deals with non-nitrogen containing crystals, and is again split into two categories. Type IIa diamonds contain no detectable defects, whilst Type IIb refers to those containing boron. Most synthetic diamonds that are colourless are usually weak Type IIb, although boron has been known to impart a grey colouration when present in high enough concentrations.

Type Ia

Type Ib

Type IIa

Type IIb
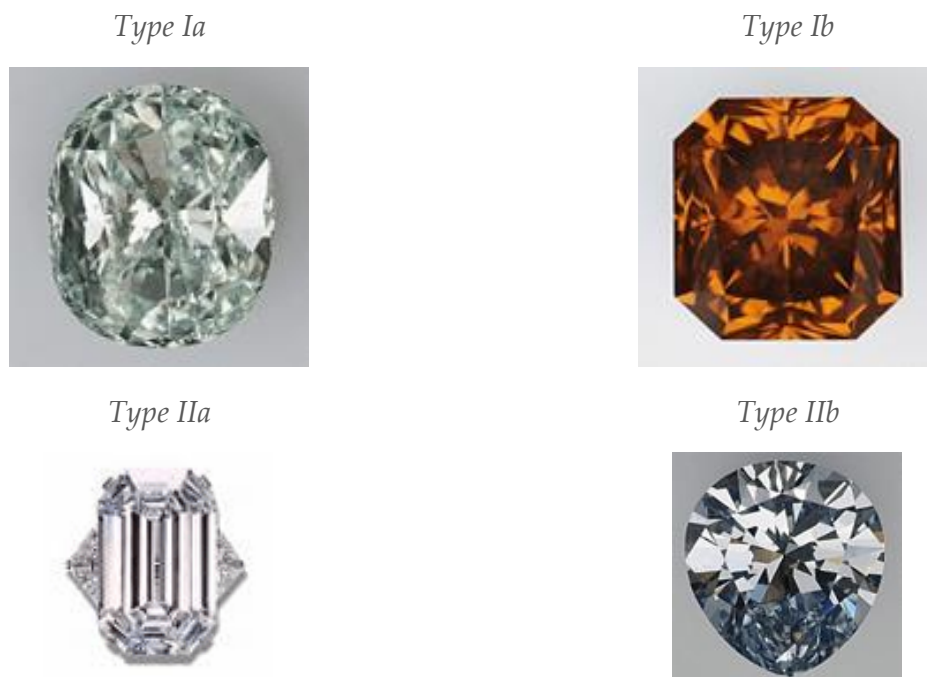
Figure 6: Photographs illustrating the four different classifications of diamond.[31]

1.2.4 Other known Defects

1.2.4.1 Nickel

Usually, nickel impurities are sourced from the metal solvent/catalyst (sol/cat) used during the synthesis process, and are known to exist as point defects within the lattice, whilst larger inclusions tend to be sol/cat that has been encapsulated when growing the diamond crystal.[12,33,30] Single-crystal HTHP diamonds grown from pure nickel are typically green in colour near to the inclusions, and display multiple zero-phonon lines at 1.83 eV and 2.51 eV (when taken at liquid N_2 temperature) as well as another at 1.40 eV, that whilst is apparent in all Type Ib diamonds, is particularly intense in those grown in nickel.[19,34] These have been found to be dependent on both the concentration and structure of the nickel present in the crystal. It is noted that crystals grown from Fe don't show these optical lines, despite having a similar colour.[12,19] Diamond crystals containing nickel also display unique luminescence bands at 2.56 eV and 1.40 eV. Studies involving EPR can be used to determine the concentration of nickel in pre-annealed crystals.[12]

Anionic nickel defects in the form of Ni^- lattice substitutions have also been detected, even at levels of up to 70 ppm, as well as positively charged Ni^+ interstitials. Also, it has been demonstrated that the concentration of the Ni^- defects are proportional to a unique absorption at 2.51 eV.[12] As with many other types of impurity, Ni defects show a strong preference for the [111] growth facet, with X-ray fluorescence experiments indicating they are only located there.

1.2.4.2 Cobalt

Cobalt-containing inclusions, unlike their nickel counterparts, remain relatively under investigated throughout the literature. These impurities can be detected using X-ray fluorescence, and much like nickel, are only found in the [111] plane. One reason for their lack of investigation is that its unique absorption band is rather weak. However, strong luminescence can be observed after heat treatment, giving rise to a yellow colour.[12,19] Any luminescence peaks depend on the degree of A-centred nitrogen.[12]

As well as possessing catalytic activity, phosphorus is also an important dopant. Being in the same group as nitrogen, it also possesses an extra valence electron when compared to carbon, meaning it can act as a donor. Advantageously, the ionisation energy required for this to happen is much lower than for nitrogen, at only 0.6 eV as opposed to 1.7 eV. [35] In turn, this makes phosphorus of great interest for n-type, semi-conducting diamond. Structurally, the phosphorus atom substitutes for carbon within the diamond lattice. Phosphorus has not been identified in samples grown using the temperature gradient HTHP method. However, interesting complexes of phosphorus and nitrogen in diamond grown under static HTHP conditions have been detected via EPR.[12] The presence of phosphorus can be determined fairly easily, showing a unique luminescence peak at 5.18 eV. Secondary ion mass spectrometry (SIMS) has also been used to study this defect.[12,33] SIMS is a Mass Spectrometry (MS) technique whereby an ion beam is used to bombard a surface with heavy particles. This releases an assortment of lighter, 'secondary' ions from the sample surface and subsurface, giving information regarding the type of atoms present.

1.2.4.4 *Silicon*

Silicon-doped diamond is formed when silicon-containing alloys are used as the catalyst during synthesis, and comprises of a single atom located within the double vacancy centre.[33, 36-37] It is important to note that any silicon present must be alloyed with another metal. This is due to silicon's propensity to form carbide phases when used on its own.[33] As with other defects, its presence can be determined using fluorescence and absorbance peaks, both of which can be found at 1.68 eV.[12] Considerable research has centred on this defect as it is a promising single phonon emitter.[33]

1.3 GRAPHITE

1.3.1 The History of Graphite and its Applications

Graphite, much like diamond, has been used since ancient times. Ancient pottery unearthed in south-eastern Europe was found to be decorated with graphite-containing ceramic paint.[38] During the 1500s, a large deposit of graphite was discovered in Cumbria,

England, where local farmers found it useful for marking their sheep.[39] In fact, the word 'graphite' stems from graphein, meaning to write or draw in Ancient Greek.[39,40] From the 16th century, all pencils were made using English natural graphite, a use which is still of importance today. Of the roughly 1.1 million tonnes of graphite mined annually, approximately 7% is used in the manufacture of pencils.[41] Owing to graphite's impressive heat resistance, one of its key uses was as a refractory material to line moulds for cannonballs. This resulted in smoother, rounder cannonballs that could be fired a greater distance, and is believed to have contributed to the strength of the English Navy during this time. As a result of this military importance, graphite mined from this source was under strict control of the Crown.

More recently, the application of graphite as a notable refractory material has been used by various heavy industries since the 1900s, with some 12,500 tonnes having been consumed for this purpose in 2010 alone. However, instead of manufacturing cannonballs for the English Navy, modern day applications of graphite's high resistance to heat are exploited by industrial blast-furnaces and various steel making processes.[41] The majority of modern graphite is produced in China, where it has found use in electronic applications.[42]

1.3.2   The Structure of Graphite

The majority of the properties mentioned in the previous section arise because of graphite's somewhat unique crystal structure. Graphite has a fascinating and well understood structure. It comprises of layers of flat hexagonal sheets of sp^2 hybridised carbon atoms, arranged in a honeycomb lattice. The bonding within the sheets comprises of covalent σ bonds, with a length of 1.45 Å (Figure 7(a)), whilst bonding between the layers is in the form of much longer, weaker van der Waals forces, with a length of 3.35

(a) **(b)**
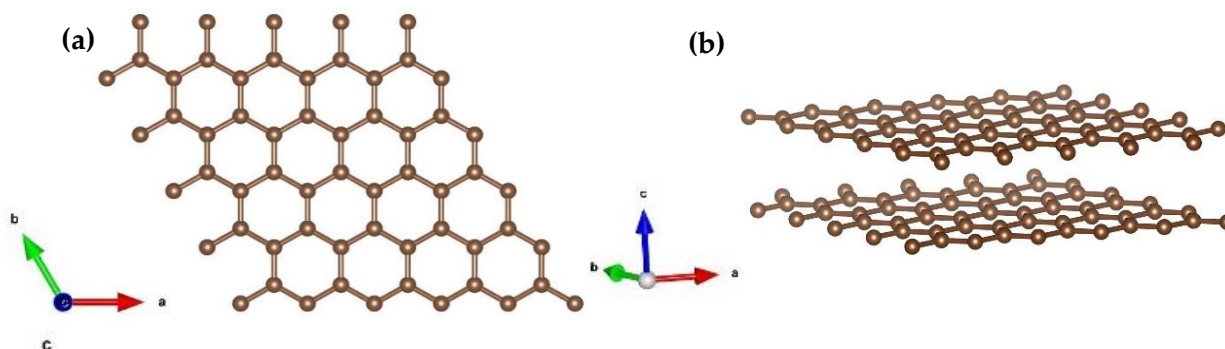
Figure 7: (a) A single layer of graphite, also known as graphene, with covalent sp^2 π bonds between atoms, and (b) two of these sheets superimposed on top of each other, with van der Waals forces acting between the layers.[42]

Å at ambient pressure (**Figure 7**(b)).[43] This stark difference in bonding between the layers accounts for graphite's highly anisotropic thermal and acoustic properties. Phonons can propagate rapidly through the sheets due to the stronger, and much stiffer covalent σ bonding. However, when travelling between the planes, the proliferation of any excitation is hindered by the weaker, more flexible van der Waals bonding. As with simple organic molecules, the extensive network of π bonds present in the graphene sheets of graphite allow the delocalisation of electrons throughout the structure, accounting for graphite's electrical conductance.[44]

Similar to diamond, graphite is also able to exhibit polymorphism. There are two main forms of graphite, 2H hexagonal, and 3R rhombohedral graphite. Hexagonal graphite is characterised by every other carbon layer overlapping, which is denoted as AB stacking, and is labelled 2H, shown in Figure 8(a). The other major polymorph has layers that overlap every three layers, and is represented as ABC stacking, with the designation 3R, shown in Figure 8(b). As shown in Figure 8(a), in 2H graphite, only every other carbon atom within a layer overlaps with that of an adjacent layer. In turn, this means that when the transformation from a flat sp^2 geometry to a three-dimensional sp^3 geometry occurs (as found in diamond), only half of the carbon atoms in a layer are able to join to those of the layers above and below.

(a)   A   B   A   B

(b)   B   A   C

2H Graphite   3R Graphite
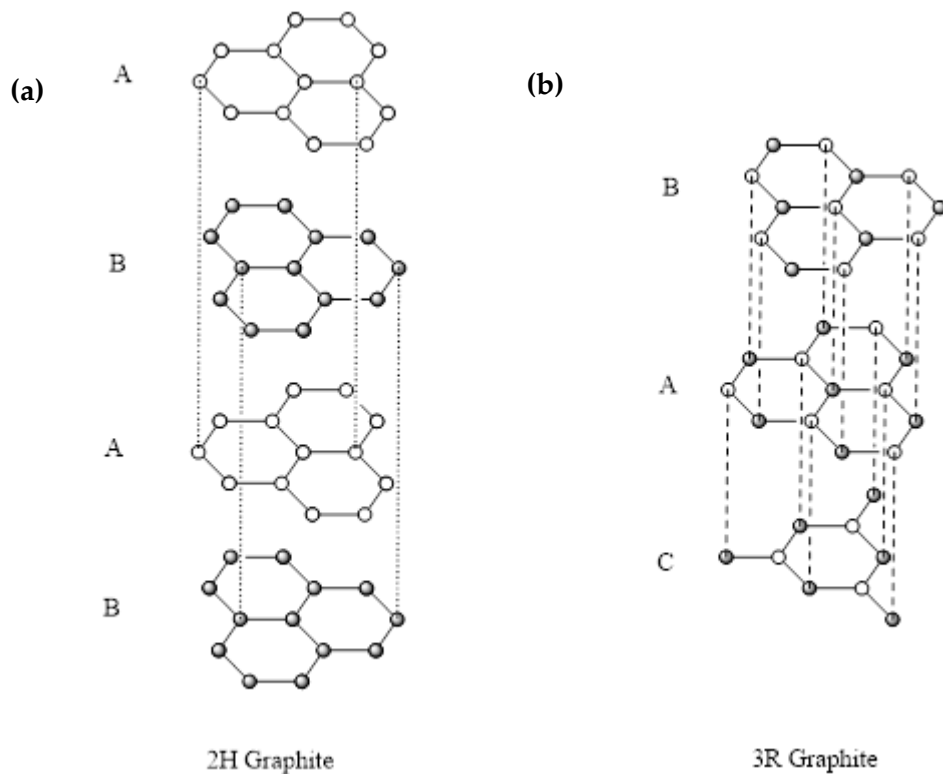
Figure 8: Schematic representation of (a) 2H graphite, and (b) 3R graphite, with the interplanar overlap being represented by the dashed line between the layers (many of these have been omitted in (a) for clarity). Note that in 2H graphite, every other layer overlaps, whereas in 3R graphite, a central layer overlaps with that above and below on every other carbon atom.

3R graphite, on the other hand, has much better overlap, with the central A layer overlapping with both the B and C sheets on alternating carbons (Figure 7(a) and (b)).[45] Importantly, this overlapping pattern produces a CCP array that is identical to that found on the [111] crystallographic plane of 3C diamond. This property of 3R graphite is of great importance in the transformation of graphite to diamond.

1.3.3 Properties

Many of the properties that made graphite an indispensable material during the 1600's are still of great significance in modern times. As previously discussed, the unique combination of van der Waals interactions in one dimension, with covalent bonding present in the other two causes graphite to exhibit many anisotropic thermal and acoustic properties. In addition to this, the high thermal stability and conductivity allow for the aforementioned application of graphite as a refractory material.

Interestingly, the presence of π bonding throughout the covalently bonded frame results in vast electron delocalization along two dimensions via aromaticity.[44]

Consequently, this has led to graphite finding various applications in the construction of electrodes for nickel-metal hydride and lithium-ion batteries. In turn, this has driven the growth of a plethora of portable electronics, such as laptops, mobile phones, smart phones and tablets.[41] Curiously, this also means that graphite is diamagnetic, and hence will float in mid-air above a strong magnet.[44]

1.4 POLYCRYSTALLINE MATERIALS

In the previous sections, the structures and properties discussed relate to the single crystal, or 'monocrystalline' structures of carbon, whereby the crystal lattice is presumed to be continuous and unbroken. The opposite of this highly ordered structure type are 'amorphous' structures, which contain no long-range order, and includes common materials such as glass. It is between these two extremes that 'polycrystalline' materials sit, with the level of order being described as the 'crystallinity' of a sample.

Essentially, a polycrystalline material is a solid that is comprised of many individual, randomly oriented single crystals of diamond and graphite, which are known as grains or crystallites. Each grain can be thought of as a single crystal, within which the atomic structure has long-range order. However, at the boundaries between these grains, any long-range order is interrupted, meaning polycrystalline materials can be considered partway between a perfect crystal and an amorphous solid. Grain boundaries are 2D defects within a single crystal structure, and their presence can have a significant impact on the physical properties of the polycrystalline material formed. For example, decreases in electrical and thermal conductivity are associated with an increase in the number of grain boundaries, and they are also responsible for the onset of corrosion and the formation of new phases in solid state synthesis.[46] The space between grains can be filled with an amorphous solid phase that can often act as a binder, further improving the mechanical strength by several mechanisms. The overall polycrystalline microstructure is characterised by the topology, morphology and crystallographic orientations of the individual grains and by the grain interfaces and microstructural defects, within the bulk grains and at the inter-granular interfaces.[47]

1.4.1 Polycrystalline Diamond

Polycrystalline diamond (PCD) is a super-hard material that possesses favourable properties over conventional cutting tools such as high hardness, abrasive resistance and high thermal conductivity.[48] Due to its superior characteristics, it is used in a variety of demanding cutting operations, including machining of advanced aerospace alloys and rock drilling in the oil and gas industry.[49,50] Diamond, being one of the hardest known materials with very low coefficient of friction, naturally makes it a suitable tribological surface for these applications. These tools are produced by sintering the diamond grains onto a WC-Co cemented carbide cylinder under HTHP conditions, usually with the addition of a binding agent such as cobalt.[46] Among the different diamond types produced using HTHP conditions, PCD stands out for its greater hardness and higher thermal conductivity than monocrystalline diamond.[48,51]

Although PCD can be formed either with or without the addition of a binder, and using any grainsize of diamond powder, the properties of PCD materials are in large part governed by these two variables. Hence, the added effects and interactions introduced by the binding material (if applicable), as well as the nature of the polycrystalline structure itself, and even its intended final use, must all be considered. For example, the inherent high cutting temperature and subsequent chemical reactivity at the machining interface causes both the chemical formation of carbide phases and a generally high amount of abrasive interaction. These can both cause a loss of diamond when in use, leading to significantly shorter tool life, and prohibiting use against certain metals such as titanium, which possesses an incredibly high affinity for carbon.[8,50,52] Fortunately, this can be mitigated by altering the sintering conditions, the initial grain size, as well as the binder species and concentration. For example, better sintering and sintering reactant choice can lower the final thermal conductivity, subsequently inhibiting the build-up of high temperatures and mitigating the increased chemical reactivity. For instance, diamond grain boundaries disrupt the motion of dislocations through the PCD matrix. Hence, reducing the crystallite size is a common way to improve mechanical strength, as described by the Hall–Petch relationship.[53]

The use of a binder metal during the sintering of the diamond bodies has two main advantages; a decrease in the sintering temperature and pressure, and the elimination of graphite adhered to the diamond particles.[54] It is important to remember that the metal matrix is also chosen, in part, based on the abrasiveness of the material to be cut and polished, as this will also have an effect on graphitisation and residual stress level.[48] Currently, most PCD diamond tools use cobalt, iron, or nickel as binders, since they provide good chemical compatibility with the diamond crystallites. However, these elements are also catalysts for graphitisation and other degradations, which are harmful transformations for diamond tools, and research into other metals such as tantalum and niobium is currently being undertaken.[48,50,51]

1.5   CONVERSION BETWEEN DIAMOND, GRAPHITE AND PCD

1.5.1   Early Attempts to Form Diamond

"A diamond is a chunk of coal that did well under pressure"

– Henry Kissinger[55]

During the majority of antiquity, the predominant elemental theory was that proposed by Aristotle, centring on air, earth, fire and water, and so the notion that rarer diamond could be formed from graphite would have not been considered. As our appreciation of science developed, attempts to further our understanding of precisely what diamond could begin. Sir Isaac Newton first proposed a potential structure for diamond after studying the photo-refractive properties of a diamond crystal, suggesting it was composed of a dense, combustible oil.[56] Around the same time, Robert Boyle, another prominent scientist, bolstered Newton's claim by demonstrating that diamond was altered upon exposure to flames. It wasn't until 1772, however, that it was quantitatively shown by Antoine Lavoisier, one of the forefathers of modern chemistry, that diamond was in fact a form of carbon. Lavoisier achieved this by focusing sunlight on a diamond crystal, producing a gas, which he then tested with lime water, and indicated the presence of CO_2.[56] A few years later, in 1786, the French scientists C. L. Berthollet, G. Monge and C. A. Vandermonde also confirmed that graphite, which had previously been thought to have been a form of lead, was actually another form of

carbon.[57] As Lavoisier built his surrounding theory of chemical elements, carbon was listed as its own chemical element in his ground breaking 1789 book titled '*Traité élémentaire de chimie*' (Elementary Treatise of Chemistry), which was translated into English by Robert Kerr the following year.[58] Hence, no attempts to make diamond from graphite occurred until the 1800s, after atomic theory had started to gain traction. It was during this era that it was realised that diamond and graphite were both allotropes of carbon, and hence could be converted from one to the other.

Following this realisation, attempts to convert the relatively cheap and abundant graphite into the much more desirable diamond began. As it was immediately noted that diamond is around 56% denser than graphite, it was speculated the use of high pressure could be one way of successfully changing graphite into other forms of carbon. This, coupled with high thermal energies, was the main line of enquiry for the remainder of the century, with some researchers, most notably J. B. Hannay, claiming to have successfully achieved the formation of synthetic diamond.[59] However, this was later disproved.[56,60]

Despite some initial setbacks, Hannay's experiments proved useful, as they constituted the first recorded attempts to solvate carbon via the use of a metal under high temperatures and pressures, in this case lithium. However, unfortunately for Hannay, the technology required to produce temperatures and pressures high enough to form diamond were not available at that time. It wasn't until 1953 that the first fully synthetic diamonds were conclusively produced, ultimately being accomplished by the Swedish corporation *Allmänna Svenska Elektriska Aktiebolaget* (ASEA; English translation - '*General Swedish Electrical Limited Company*').[61] Despite this initial success, however, it took until 1955 for the first reproducible production of synthetic diamond under HTHP conditions, with this being achieved by the US based General Electric Company.[62]

After the first replicable synthesis of diamond under HTHP conditions, intense research in the area continued. However, as previously discussed, it was noted that diamond is around 56% denser than graphite. Hence, the use of high pressures was key in making the formation of diamond thermodynamically easier.[8] As diamond is the less stable form of carbon, with a $\Delta G° = + 2.895$ kJ mol^{-1},[60] an increase in pressure creates the

negative free energy required for the reaction to occur. However, in order for the reaction to proceed at an appreciable rate, the temperature must be raised to around 1200 °C. Frustratingly, this favours the formation of graphite, therefore inhibiting the growth of diamond crystals. Hence, pressures of around 5 GPa, as well as the use of a catalyst, are required to make the formation of diamond feasible.[63] Such extreme conditions pose a significant engineering challenge, and requires the use of specialist equipment and experimental techniques.

1.5.2 Direct Graphite to Diamond Transition Mechanism

As previously discussed, for graphite to be converted directly into 3C diamond, it must be stacked in the 3R conformation. Unfortunately, natural graphite usually comprises of an average of 85% 2H, and 15% 3R. Therefore, the vast majority of the graphite sample must re-order itself into the correct stacking order. This occurs via the sliding of sheets, and a linear movement of one bond length is all that is required to convert 2H to 3R graphite. The process of sliding is thermally activated, and for non-catalysed reactions, is rate determining.[43,64]

3R Graphite   3C Diamond
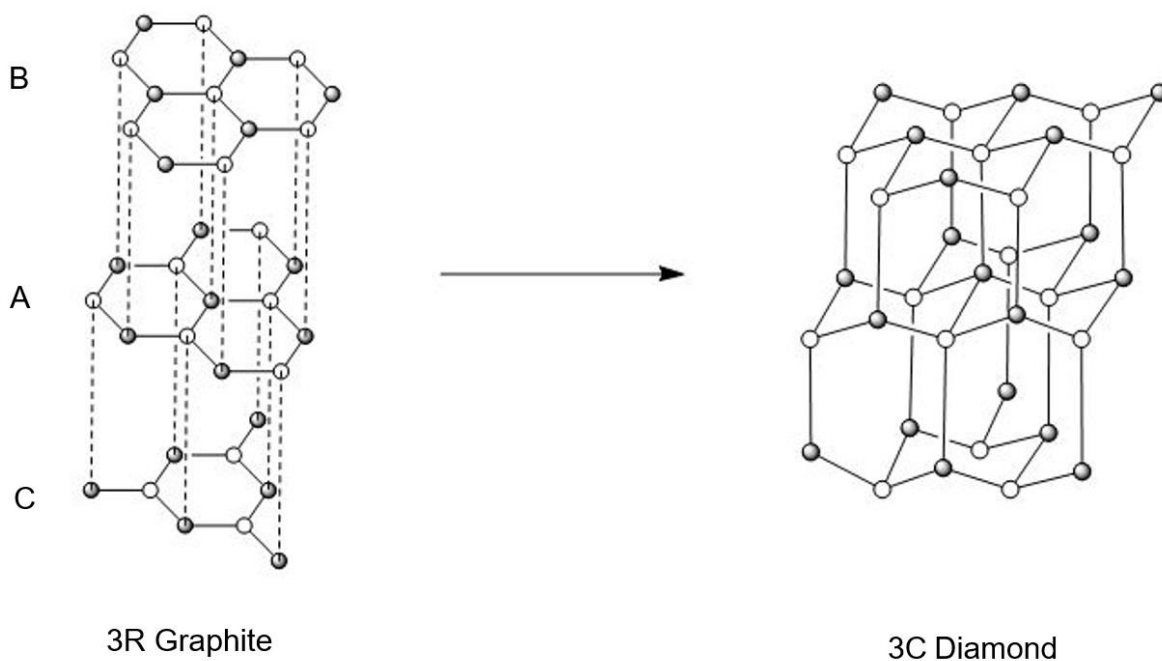
Figure 9: A schematic representation of the direct conversion of 3R graphite to 3C diamond. The different coloured atoms correspond to the two CCP arrays. The dashed bonds indicate where the new covalent bonds form. Note that in the 3C structure, the vertical bonds between the layers are exaggerated for clarity.

Once the sheets have arranged themselves in the correct 3R position, then the flat sp² hybridized sheets can begin to pucker into the likely. However, in order for this to occur, the distance between the graphite sheets needs to be reduced from 3.35 Å at ambient pressure to the 1.54 Å bond length of sp³ carbon. By doing this, calculations have shown that the activation energy, E_a, of the reaction is reduced from a maximum of 0.33 eV at standard pressure to as low as 0.28 eV at 5 GPa, or even 0.23 eV at 20 GPa.[43] Once the layers are close enough that the E_a barrier has been overcome, a wave-like buckling of the sheets propagates through the graphite. As the buckled sheets approach an angle of 30°, the gap between the sheets reaches 2.08 Å, which is roughly equal to the separation of the [111] crystallographic plane in 3C diamond. Recent computational studies have also shown that the slipping and buckling of layers may take place simultaneously. Once the sheets are at the critical angle of 30° for 3C diamond, then the conversion can take place, forming sp³ bonds, and the diamond unit cell (Figure 9).

1.5.3 Catalysed Diamond to Graphite Transition Mechanism

Despite considerable research being undertaken on the catalysed mechanism of diamond formation, there is still significant confusion surrounding the exact chemical mechanism behind catalyst assisted growth. Experiments have determined that a diffusion-type process is the limiting step, with evidence for this occurring via the formation of carbides.[7,65–68] At all times during synthesis, there exists a thin metal film (TMF) covering the growing diamond, with the newly formed diamond growing into the graphite starting material, with various reactions taking place.[69] Overall, experimental and theoretical considerations have identified these to be various interfacial and diffusion-type processes. For the forward reaction, the processes occurring within the TMF are accepted to occur in the following order:[65]

1. Dissolving of carbon from the graphitic starting material into the catalytic metal forming a solution. This is an interfacial process occurring at the graphite-metal interface.

2. As the solvated carbon enters the TMF, it's concentration rises, being highest at the graphite source interface.

3. Diffusion of the solvated carbon through the metal solution to areas of lower carbon concentration. How this occurs is still under significant debate, however the detection of carbide phases in the solution is believed to play an important role.[68]

4. Once thermodynamically favourable for the formation of critical diamond nuclei, growth then occurs outwards, with the deposition of new carbon atoms occurring at the new diamond-TMF boundary.

For the reverse reaction, the same processes occur in the same order. However, it is diamond that is solvated and graphite that is formed. How the solvated carbon moves across the TMF is believed to occur through the presence of carbides.[68] Examination of a Ni-Mn catalyst found that close to the graphite-metal interface, only graphitic carbon fragments along with metal carbides were present, whilst at the diamond-metal interface, the opposite was true. This indicates that graphite does not directly convert to diamond within the TMF, as this would lead to graphite and diamond-like carbon being present side by side, as opposed to being observed in two distinct areas. Furthermore, the composition of the carbides present changed as they neared the diamond phase, with a lowering of the carbon:metal ratio. The lowering of this ratio is most likely due to the formation of diamond around that area, with this being driven by the higher surface energy of diamond.

1.5.4 Catalysts for Diamond Formation

1.5.4.1 *Metal*

When choosing a suitable metal catalyst, the main factors to be considered are the melting point of the catalyst, as well as its reactivity towards carbon. By far, the most widely used catalysts are Fe, Ni and Co, with as little as 1 wt% of Ni initiating growth.[8,12] Other metals such as Pt, Pa, Rh, Ru, Pa, Ir, Os, Ta, Mn, Mg and Cr have also been reported to work for the process.[12,65,70] Aside from lowering reaction temperatures and pressures, the choice of catalyst can also affect the morphology of the crystals formed, as well as the concentration of any impurities.[69]

The way in which metals tend to interact with carbon is by overlapping of the metal's d-orbitals with the carbon p-orbitals. Therefore, the reactivity of a metal towards

carbon is dictated by the number of d-orbital vacancies.[8] This is reflected experimentally. For example, copper, with a fully occupied d-orbital, is inert towards carbon, and will not act as a catalyst. Titanium, on the other hand, with a d^2 electronic configuration, is too reactive, and will form a carbide phase. This essentially 'locks' the carbon into a new phase, preventing it from crystallising into diamond. Finally, iron, which has a close to half-filled d-orbital (d^6), adequately reacts with carbon to form a solid-solution, but is not reactive enough to form a separate carbide phase.[8] Furthermore, if a carbon inert metal such as copper is alloyed with a carbon attracter like nickel, the two effects cancel, and catalytic activity is observed. Although this is not as effective as using a single element, this technique can be exploited in order to lower the melting point of the alloy.[8,12]

The exploitation of the melting point of the catalyst is also of importance. In order for any solvated carbon to move and form a crystalline phase, mobility through the solvent is a must. This requirement for the metal catalyst to also act as the solvent for the reaction is why these systems are often referred to as sol/cat systems. Furthermore, the reaction temperature must be higher than the melting point of the metal carbide in order to prevent an unwanted solid phase forming, which has further implications on the manufacture of PCD. The temperature at which this occurs also increases with the number of d-orbital vacancies present in the metal, hence why titanium is a strong carbide former.[8]

The trends outlined above also apply to nitrogen, and as nitrogen has a greater number of p-electrons, the nitride phase that is formed is more stable than the competing carbide.[13] This effect is known as 'nitrogen getting', as it causes any nitrogen present to be locked into a separate phase, forming perfect Type IIa diamonds. By adding a small amount of metal with a high number of d-orbital vacancies to the catalyst alloy, it is possible to drastically lower the nitrogen content present in the newly synthesised diamond. Typical examples of metals often used for this purpose are Ti, Zr, and Al. By using these 'getting' elements, or 'getters', it is possible to synthesise colourless diamond with a nitrogen content of less than 1 ppm.[12] Furthermore, the choice of metal can also affect other impurities in the diamond (see Section 1.2).[13] The overall effectiveness of an element to act as a nitrogen getter is dictated by the affinity of the metal for nitrogen.

The higher the affinity, the more likely nitrogen is to be locked into the sol/cat material.[12] Moreover, growth temperatures also have an effect on the inclusion of nitrogen, with concentrations decreasing with increasing temperatures if no getters are present. However, if a nitrogen getter is present, this trend reverses.[12] This means that reactions can be performed at lower temperatures, which is not only more cost effective, but can also alter the morphology of the final crystal.

1.5.5 Thermodynamics

1.5.5.1 The Diamond-Graphite Phase Boundary

At the start of the reaction, before the temperature and pressure are altered, graphite is the favoured allotrope. Then, as the temperature and pressure of the reaction vessel begin to increase, a point is reached where this favourability is flipped. Hence, for a given temperature, there is a critical pressure, and for a given pressure a critical temperature, when the free energy is equal to zero, favouring no allotrope over the other. This is known as equilibrium (Figure 10), and there is no net formation of any species
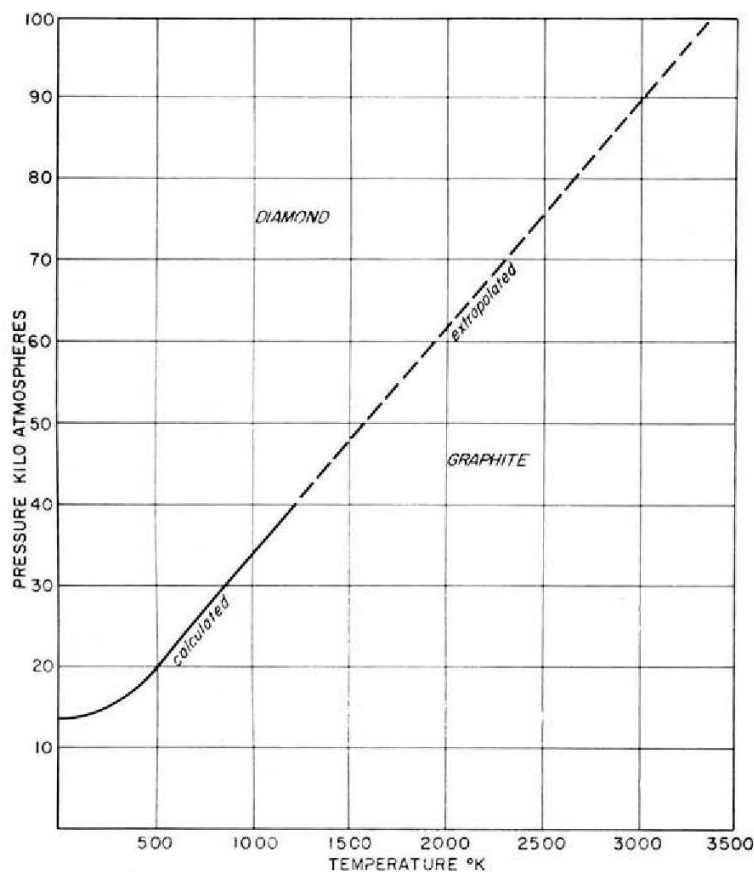
Figure 10: The diamond-graphite equilibrium line calculated by Berman and Simon by plotting the pressure as a function of temperature.[73]

present in this state. Suppose that during synthesis, the corresponding equilibrium values for temperature and pressure are met, *i.e.*, the conditions are at the thermodynamic boundary between the graphite and diamond phase. Here, a slight increase in temperature would also warrant a slight increase in pressure in order to maintain this. Hence, there is a relationship between the temperature and pressure at the boundary.[71] This relationship can be expressed using the Clapeyron equation,[72,73] given by,

$$\frac{dp}{dT} = \frac{\Delta H}{T.\Delta V} \text{ ,} \qquad\qquad (1.1)$$

where dp/dT is the gradient of the pressure-temperature boundary, ΔH is the enthalpy change of transition, T is the current temperature of the system, and ΔV is the volume change caused by the transition (for the conversion of diamond into graphite, this value is negative, with its magnitude depending on the amount of externally applied pressure). Once the thermodynamic conditions have been met, the main factors affecting the formation and growth of diamond become predominantly kinetic.

1.5.6 Diamond Crystal Nucleation and Growth

During crystal formation, two main events occur, nucleation, followed by crystal growth.[65] Simply, nucleation is the step where the solute atoms of carbon begin to gather into a new crystalline diamond phase. This process can only happen when it is thermodynamically favourable for the species in question to be in the solid, crystal form as opposed to in solution. The energy required for this to happen is known as the nucleation barrier, and crossing this is often brought about by changing the conditions of the solution. This change in conditions can be enacted via a temperature change, as exploited by the temperature gradient method, by changing the concentration of the solute in the solution, or by decreasing the solubility of the solvent. There are two main pathways by which nucleation occurs: heterogeneous and homogeneous. Heterogeneous nucleation occurs at sites on surfaces present in the system, hence the use of seed crystals by some, and tends to dominate the overall process.[74] Meanwhile, homogeneous nucleation occurs away from these sites, generally playing a less active

role. The overall process of nucleation is extremely sensitive to any impurities present, and impurities that are too small for even the naked eye can affect the rate at which this process occurs. Usually, it is a random, 'stochastic' process, meaning that two identical systems can nucleate at differing times.[75] Due to this unpredictable nature, the process of changing graphite to carbon is dominated by kinetics.

Once the process of nucleation has begun, forming small, microscopic crystals, these then undergo crystal growth to create larger crystals. Overall, this is when other atoms of carbon exit the surrounding TMF, and take their place in the crystal lattice. At temperatures well below the melting point of the final crystalline product, the interface between a growing crystal and the solution is molecularly sharp. The crystal then grows outwards at this interface one layer of atoms at a time. For the formation and growth of synthetic diamond, the nucleation process is heterogeneous, whilst growth of a pre-existing crystal occurs through the TMF, with these processes happening in competition with each other.[76,65] During this process, the newly formed diamond nucleates at the graphite-catalyst interface, and then grows into the graphite through the surrounding film.[76] The rate at which this process occurs increases with reaction temperature, and/or a steeper temperature gradient. However, this, in turn, can cause more inclusions to be incurred.[12]

1.5.6.1   Nucleation

The nucleation of diamond crystals is the biggest barrier to overcome during synthesis, and is regarded as the rate determining step,[77] as the E_a required for nucleation is much higher than the energy barrier for crystal growth.[78,79] The favourability of new nuclei forming is normally expressed using a quantity called the Gibbs free energy of nucleation, ΔG_n. It is worth noting that, here, ΔG_n is not a molar quantity, and describes the free energy present for any given nucleus as a whole. For a newly formed nucleus to be stable enough to grow, its size, l, must pass a critical value, l_c. Below l_c, random fluctuations, as well as the thermal energy of the system, is sufficient enough to destroy the new nucleus before crystal growth can occur.

Once it is thermodynamically favourable for critical nuclei to form, the rate at which they appear can be found by applying the theory for the kinetics of nuclei

formation.[80] By doing so, the positive effect of temperature on the rate of nucleation can be rationalised, as well as the negative effect of the surface energy. Fortunately, the value for this can be lowered with the use of a catalyst, which accounts for the lower reaction temperatures and pressures required for sol/cat synthesis.

Alternatively, the barrier presented by nucleation can be avoided altogether via the use of seed crystals. However, even when this method has been employed, it has been shown that some new nuclei still form during the reaction. Once this process is complete, the newly formed nuclei are then able to undergo crystal growth.

1.5.6.2 Crystal Growth

Due to nucleation being the rate determining step, the process of growth of existing nuclei is responsible for the majority of diamond formation. Therefore, it is advantageous to explore the variables that affect this. Despite the mechanism for catalysed diamond growth being poorly understood, it is still possible to rationalise various quantities based on the ratio of graphite and diamond present once the reaction has been stopped. Due to mystery surrounding the TMF, it is impossible to derive expressions for the transformation process based on theoretical considerations alone. However, it is still possible to experimentally determine the kinetic relationship present across the system as a whole. In doing so, it has been demonstrated that this process follows well known diffusion laws, specifically Fick's laws of Diffusion.[72] It is important to note that quantities that are determined via experimentation can only represent the overall transition taking place, and not for any intermediate steps that may be occurring. As changes in temperature have been shown to play a very specific role, it is important to explore how this variable affects the growth of diamond nuclei. Note that in the following section it is assumed that the pressure is constant, and only the temperature is varied.

Synthetic diamond has been shown to grow in one of two major crystal morphologies, cubic and octahedral. Hence, as the amount of diamond increases, the volume of these two structures will change. As the volumes of both cubic and octahedral structures depend on the length of their edges, the change in size, and by extension weight, of the growing crystal can be characterised by this one parameter. As such, by

plotting the change in length against the reaction time, it has been experimentally determined that the change in volume of diamond is proportional to the square root of time.[65] As the growth rate, K, varies according to a[2], it can be inferred that the process for growth is dependent on the surface area of the crystal, and is therefore a diffusion controlled, surface interaction. Fortunately, this can be examined by looking at the change in weight of the diamond crystals.[66] Experimentally, evidence has shown that the mass of diamond formed during a certain time frame can be modelled using the following equation (Equation 1.2);[7]

$$\Delta w = \frac{Kt}{\delta} \ , \tag{1.2}$$

where Δw is the change in mass, δ is the thickness of the thin metal film and K is an unknown constant. The value for δ has been shown to remain constant during the reaction, and for a Ni system, is equal to ~100 μm. As outlined above, this is analogous to growth via a diffusion mechanism occurring through the TMF. Importantly, this means that Frick's first law of diffusion can be used to further analyse the process. Fick's first law can be expressed by,[72]

$$J = D\nabla C \ , \tag{1.3}$$

where J is diffusive flux, D is the diffusion coefficient across the TMF, and ∇C is the concentration gradient of carbon across the TMF. By applying this to Equation 1.2, it is possible to derive the following relationship,

$$\Delta w = \frac{D\Delta CAt}{\delta}, \tag{1.4}$$

with ΔC being the difference in solubility between graphite and diamond in relation to the TMF, and A being the surface area in contact with the TMF, and D being a quantity known as the diffusion coefficient. Notably, this gives an expression for K,

$$K = D\Delta CA \ . \tag{1.5}$$

Hence, a deeper understanding of the variables affecting the rate constant, and by extension, the overall formation of diamond, can be explored. The simplest variable to deduce is A, and is merely the surface area of the growing diamond nucleus, and therefore must be a positive value.

36

Following this, the effect of D can be examined. In the simplest terms, D is a measure of how easily solvated carbon can diffuse from one side of the TMF to the other. It is independent of direction, meaning that whether the carbon is solvated from graphite or diamond is irrelevant. The process of diffusion occurs via an unknown mechanism, however, as with any mechanistic process, it has an activation energy, E_a, that must be overcome. This can be achieved using higher temperatures, although its overall effect on diamond growth is nominal.

Finally, the effect of ΔC must be investigated. ΔC is the difference in the solubility between graphite and diamond in relation to the TMF, and is important because above this limit, any excess diamond or graphite will begin to precipitate out of the TMF. In general, how this varies with temperature can be shown using an Arrhenius-type equation,[65]

$$C = C_0 e^{-\frac{Q}{RT}}, \tag{1.6}$$

with C being the concentration of diamond or graphite sourced carbon at temperature T, C_0 being the concentration at ambient temperature, and Q being activation energy required for the solvation of carbon into the TMF, and hence must be positive. As the process of solvation occurs at the interface between the TMF and either graphite or carbon, it depends on the surface energy, σ, present at that interface, *i.e.*, the amount of solvation of a given species must be proportional to the surface energy of the species it is trying to solvate. Therefore, at a certain temperature and pressure, the higher the surface energy, the higher the activation energy associated with the transition. Moreover, the surface energy in diamond, σ_D, is much higher than the surface energy in graphite, σ_G, meaning that the amount of free energy required to solvate carbon at the diamond-TMF interface will be higher, and hence, less likely to proceed than at the graphite interface. These relationships can be summarised by the following,

$$Q \propto \sigma \tag{1.7}$$

$$\sigma_D > \sigma_G \tag{1.8}$$

$$\therefore Q_D > Q_G \ . \tag{1.9}$$

This difference is crucial, because, as can be seen in equation 1.6, a lower value for Q will give a higher value for C. Furthermore, how this solubility limit varies with temperature will also differ. The significance of this can be more adequately explored by linearising Equation 1.6,

$$\ln C = \ln C_0 - \frac{Q}{R} \cdot \frac{1}{T} \tag{1.10}$$

$$\therefore m \propto -\frac{Q}{R} \tag{1.11}$$

By doing this, the rate of change in the mass of a solvated species, m, is solely dependent on Q, as R is a constant ($R = 8.314$ J mol^{-1} K^{-1}). Moreover, m can also be seen to be negative, with a higher value of Q giving a more negative m. As outlined above, Q_D is greater than Q_G, meaning that diamond will be less soluble, and will therefore be more likely to form. Hence, it has been shown that the difference in solubility that is caused by the difference in surface energies is responsible for the majority of diamond formation. By extension, this can therefore be considered to be the main driving force of the transformation.

1.5.7 Morphology

Generally speaking, the overall, macroscopic geometry of the new crystal formed is reflective of the dominant growth face. Cubic crystals are formed at lower temperatures of around 1300 °C, when the [100] face is the most dominant. However, at higher temperatures this changes, with the [111] face becoming the most dominant, with these being determined by their relative surface energies. This occurs at around 1800 °C, causing octahedral crystals to be formed.[12] At temperatures in between, cubo-octahedral crystals are observed. Other minor growth surfaces that have been reported are the [113] and [110] faces. Growth via the [115] face was reported to have occurred when a boron-doped Co-Ti catalyst was used at low temperatures, indicating some dependence on the catalyst.[12] Overall, the morphology is very sensitive to the growth temperature and the composition of the sol/cat.[12] Hence, considerable care is needed during the synthesis process, especially as this can have further implications during the sintering process that takes place during the formation of PCD.

1.6   FORMATION OF PCD DIAMOND

PCD is typically produced by the sintering of diamond powders in the presence of a metallic binder, under HTHP conditions similar to those utilised for diamond synthesis from graphite. Generally, the diamond grit is fixed onto a tungsten carbide substrate, from which binder infiltrates through the diamond grains and acts as a solvent-catalyst in the same manner as during diamond synthesis. This allows for direct diamond to diamond grain bonding, as any crystalline growth will occur inside the diamond stability region. Furthermore, the presence of a fluid phase in the voids between grains allows for the wetting of diamond crystallites, allowing both for their movement relative to one another, and lowering the interfacial energy between the two boundaries. The resulting microstructure is composed of an interlocking matrix of diamond grains, with any metallic binder being distributed throughout the voids in between. The binder can wet both around the diamond grains as if submerging them, as well as becoming trapped between the grain boundaries, and in turn has an important impact on the sintering process.

1.6.1   Sintering

Broadly, sintering is the thermal treatment of a powder or powder compact at an elevated temperature below its melting point, with the goal of providing an increased level of strength via a bonding together of the particles. This can occur via multiple mechanisms, which, depending on the specific example, can encompass both solid and liquid state processes. Fundamentally, this is driven by a reduction in the surface area, and hence surface energy, present in the sample.

For any polycrystalline solid, there are two main environments, the solid crystallites alongside the amorphous spaces, or pores, between them, with the grain boundary acting as the interface between the two. Here the total, macroscopic volume of the polycrystal is composed of the volume of the solid grains, and the volume of the pores. The amount of pore volume present is given by the porosity, which is simply a ratio of the volume taken up by the pores versus the volume of the solid as a whole. In the case of a perfect single crystal, the ratio between these two volumes would be zero, as in all the volume would be solid crystal with zero pores present, and the density

would be the normal crystal density. As pores are introduced into the structure, this ratio will begin to increase, with a coinciding drop in density away from the single crystal value. Hence, the porosity can, in effect, be considered as a measure of the density of the crystalline phases present in a polycrystal, with decreases in this value indicating an increase in the size and packing efficiency of the crystallites. As the grains present begin to grow into the pores and bond together at the boundaries, the required reduction in surface energy can occur either via reducing the pore volume, or by rearrangement of the pore surfaces with no reduction in volume. These two processes are known as densification and coarsening, respectively.

In the solid state, these processes mainly occur via diffusional processes taking place at the grain boundaries, causing these to bond together in a process known as necking (Figure 11).[81] A result of this is that transported matter deposits at the grain boundary, causing the voids between the grains to shrink, and by extension, an increase in the size of the grains. Overall, this causes the initial powder compact to increase in density, hence the term 'densification'.

Depending on the components present in the original powder compact, various liquid state processes can occur alongside the solid-state diffusion mechanisms previously discussed. Primarily, the predominant liquid state densification mechanisms are the spatial rearrangement of wetted solid particles dispersed in a low viscosity liquid such as molten cobalt, as well as solution and re-precipitation of atoms from the grains at the necking boundary. Furthermore, the presence of this liquid can allow the grains to slip past each other and grants them the mobility to find the packing array with the greatest density. As the pore volumes are filled with this liquid, any grain growth occurs
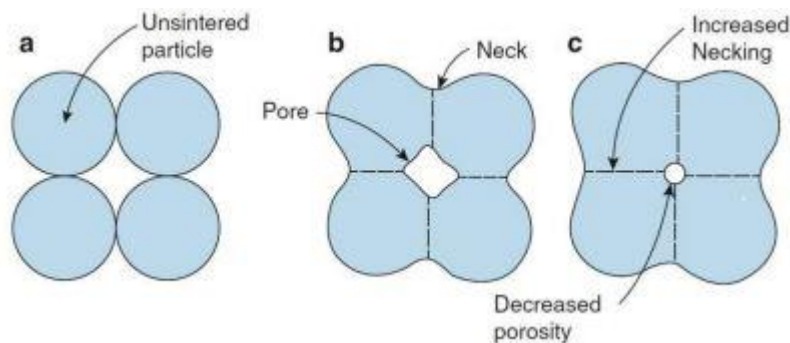
Figure 11: Schematic representation of polycrystalline densification of single crystals via necking of the grain boundaries.[81]

via precipitation onto the growing grain surfaces instead of boundaries, meaning that the overall pore volume is maintained. This causes them to increase in size and packing efficiency, and accounts for the coarsening process. Initially, this causes the smoothening of grains and the formation of grain boundaries, which is then followed by diffusional grain growth and densification, allowing for the necking process to occur. In order to do this successfully, the binding material needs to be able to fully wet the diamond grain, meaning that the particle size of the binding powder added to the initial compact must be a lot smaller than that for diamond powder.[48]

`   Specifically for PCD formation using a cobalt binder, the diamond and binder materials are combined into the polycrystalline structure with two types of bond,[82] the diamond-cobalt bond (D-Co) and the diamond-diamond bond (D-D). D-Co bonding exists at the interface of diamond grains and any pores, whilst the diamond grains themselves are combined by strong D-D bonding.[50] The use of a binder metal during the sintering of the diamond bodies has two main advantages; decreasing the sintering temperature and pressure owing to coarsening, and the elimination of graphite adhered to the diamond particles due to the catalyst effects of solvating carbon, and also by lowering the interfacial energy present at the interfacial boundary when compared to a vacuum or gas.[48]

Following the transportaion of any carbon, either in the solid or liquid states, any deposited material does not have to be in the same phase as that from which it came, meaning that any adhered graphite can be redeposited as diamond, provided that the surrounding conditions thermodynamically lie within the diamond stability region. Moreover, if the surrounding conditions instead favour graphite formation, it is this phase that will be deposited at the boundaries, with this causing unwanted graphitisation in PCD products during use.

1.6.2 Grain Size

The effect that grain size has on the final properties of the polycrystal arise due to the interesting phenomena that manifest at the grain boundaries. As a result of the surface energy present at a phase boundary, it is more energetically favourable for a phase to have the smallest amount of interfacial area possible for a given amount of bulk

phase. This surface energy between two phases is indicative of the amount of energy it would require to create and maintain a new interface between them, meaning the greater the interfacial area present in a system, the higher the amount of surface energy present. Interfacial surface area itself is related to the radius of the grains present, with a smaller grain size corresponding to an increased level throughout the system.[48] In order to combat this, surfaces of the same phase tend to join, decreasing the total surface area present in the system. This tendency of boundaries within a phase to join at the surface also has implications regarding the shape of the surface itself, as interfacial surfaces experience an outwards internal pressure stemming from the bulk, thus making convex surfaces unfavourable, and concave surfaces more favourable. In a concave shape, the outer boundaries are facing each other, meaning that when the two interfaces meet, the forces behind the two are directed towards each other. Convex surfaces on the other hand have internal pressures that face away from two boundaries, essentially keeping them apart and fighting the external pressure. This causes a reduction in the pressure felt at the phase boundary, with the new pressure at this point being known as the Laplace pressure, or capillary pressure.[82] Based on a computational study of the pore shapes formed by diamond particles during the powder sintering step, it is predicted that these capillary forces are directed opposite to external forces.[82] For a perfectly spherical dispersed phase, the Laplace pressure will decrease along with the surface energy of the interface, and increase with a decrease in radius of the dispersed phase, with the effect usually becoming appreciable at < 5 μm. The sintering of diamond powder with particle size of 28 – 40 μm indicates that the Laplace pressure does not exceed 0.16 GPa, in spite of external pressures of 8 GPa. Hence, whilst sintering these grains under the same conditions, the pressure near the pore surface still corresponds to the thermodynamic region of graphite stability, and hence will begin to graphitise at the grain boundaries.[82] Moreover, due to graphite's larger molar volume when compared to diamond, any new deposits will increase the external pressure acting on the pores.

1.6.3 Binder

In essence, the purpose of the metal matrix is to produce a series of physical-chemical interactions with diamond particles so that the disadvantages of pure diamonds (such as low toughness) can be reduced.[48] The use of a binder metal during

the sintering of diamond powder can provide many advantages during synthesis of PCD and, in turn, has many implications on the properties of the final product.[48] The variables governing this are wide ranging, including the chemical nature of the species being used, the particle size and shape of the species in the pre-sintered compact, as well as the amount present. A common example of a PCD binding material is cobalt, the content variation of which has been shown to drastically influence the distribution of diamond and cobalt phases, the wear resistance of the final composites, as well as the thermal stability.[46,83] These advantages are due to cobalt's catalytic ability to promote the formation of D-D bonds among the diamond grains through a dissolution-recrystallisation process in the synthesis procedure, as well as its ability to wet carbon surfaces and reduce the interfacial tension between contacting phases.[46]

Another critical parameter when considering the effect of a given binder is its behaviour in relation to graphitisation, as this undesired reaction impairs the mechanical properties of the compounds obtained.[48] Whilst under the HTHP conditions present in the sintering process, any solvated carbon will be re-precipitated as diamond. However, when the final products are being subjected to the high temperature, low pressure conditions often found in their applications, any catalytic activity will instead lead to graphite deposition. Moreover, the high temperatures often present in applicational settings also create issues surrounding the differing thermal expansion coefficients of the constituent parts.[48,51] Single crystal diamond possesses an incredibly low level of thermal expansion, whilst most metals, especially cobalt and nickel, expand at a much more appreciable rate. This mismatch in expansions means that the diamond grains will begin to be forced apart by the surrounding metal filled boundaries. This is known as 'residual stress', and is a common mode of failure.

One noted way of combating the build-up of residual stress is to use a less reactive metal, with a lower TEC that is closer to that of diamond. Two examples of this are niobium and tantalum.[48,51] PCD products that are manufactured with these as binders showed a decrease in graphitisation due to the formation of carbide phases, as well as a reduced occurrence of inter-granular cleavage fractures.[51] Tantalum especially showed promise, as its other properties include an excellent level of heat and electrical conduction, excellent ductility and a high melting point. All of these properties work

together to help prevent the build-up of heat and residual stress within the PCD structure, which are two main sources of degradation.[51]

Another way to improve the thermal stability and prevent graphitisation is to prevent the interactions that cause graphitisation. Interestingly, at temperatures below 1700 °C, any diamond graphitisation occurs mostly as a result of interactions with oxygen-containing compounds that are found in pores and on the surface of particles.[82] A surprising example of this is the reported use of metallic titanium, which showed a significant improvement over more common examples due the formation of a superficial TiO_2 film in the structure. Despite being a strong carbide former, titaniums' affinity for oxygen is even greater still, thus the oxygen that would have been destined for the formation of CO and CO_2 is, instead, consumed in the film, thereby protecting the PDC against oxidation.[51]

1.6.4 Failure

Generally, the wear and ultimate failure of PCD tools is brought about by the formation of micro-scale cracks within the polycrystalline structure.[50] These cracks can form both inter-granularly as well as trans-granularly. Inter-granular cracks arise due to poor bonding between grain boundaries and surfaces, whilst trans-granular fractures appear along the natural cleavage plane of crystallite grains.[50] The ability of a PCD sample to resist this is quantified by its fracture toughness, and it has been shown that the initial size of the diamond grains, the amount and type of binding materials, the residual stress within the PCD structure, as well as the external dynamic load, all impact on this.[50,84]

Diamond grain size and the amount of binder influence the ability of the grains to interlock, in turn affecting the ability to form grain boundaries and bonds. The size of the diamond grains also has a direct influence on the surface energies present, which has implications regarding the nature of the catalyst used. Some metals, such as Ti, have a strong affinity for carbon, and will form separate carbide phases, whilst others such cobalt and nickel have lower affinities, allowing for both the solvation and deposition of carbon, thereby improving the level of bond formation. The type of metal also has further implications when PCD is used in high temperature applications such as drilling,

as differences in TEC between it and diamond will cause the build-up of residual stress between grains and the subsequent formation of micro-cracks.[46,49]

Residual stress exists at the interface of the diamond and binding material and within the combined diamond grains. External heat and load are the main sources resulting in the residual stress. Residual stress inside the PCD is generated by three processes: sintering, brazing, and grinding.[50,85] Experimental investigation determined that, in PCD cutters, the highest residual stress exists at the interface between the diamond layer and substrate,[86] indicating that the diamond phase reacts with oxygen and forms gaseous carbon oxides at high temperatures.[87]

1.7 PROJECT AIMS

Considering the many desirable properties exhibited by diamond and its related composites, when juxtaposed to the notoriously difficult conditions under which they must be manufactured, this project has focused on developing a novel apparatus for reliable and efficient generation of the high pressures typically required for the high temperature synthesis and manufacture of diamond-based materials. In order to achieve this, high performance materials must be tailored and designed to be used in harmony, so that the desired properties of these constituent components can be put to use to best suit their intended function within the aforementioned apparatus.

The work presented here sets out to use a newly conceived approach to generating the HTHP conditions needed to produce PCD samples for analysis via SEM and Raman spectroscopy. In doing so, it is anticipated that diamond-based powder starting materials, in the presence of a catalytic cobalt binding material, will be converted into a network of bonded diamond grains suitable for use as a drill bit for the manufacturing and fabrication sectors. In order to further corroborate results gained form the PCD produced, evidenced-based analysis has been conducted to estimate the pressures achieved by the new set-up, and its' new approach to generating high pressures whilst under high temperature conditions.

Alongside the investigation into the diamond-based materials produced, further exploration of the materials used to form the apparatus will be undertaken. This will aim

to improve any short comings identified following the synthesis of PCD, as well as to improve both the overall efficiency and efficacy of the newly developed method.

The overarching aim of this project is to achieve the reproducible production diamond products that possess the desired properties, providing high-performance, specialist products for use in specialist areas, that are above and beyond what is currently available from standard industry products.

2 METHODOLOGY

2.1 CURRENT SYNTHETIC TECHNIQUES

The most common and widely used method for the catalytic preparation of diamond is to place alternating discs of graphite and catalyst into a central reaction cell, which is subsequently surrounded by a pressure medium such as NaCl or pyrophyllite.[12,76,88,89] This enables the pressure to remain constant through the entirety of the reaction chamber. Heating of the reaction is usually achieved via an external source such as a furnace.

For this general set up, there are a few accompanying techniques that can be used. For example, the temperature gradient method, which was used by De Beers to grow a record setting 34.8 carat diamond.[12] This method exploits the differing solubility of carbon in the catalyst at differing temperatures. By placing the graphite at a higher temperature, it is able to saturate the catalyst with carbon. The solvate is then able to diffuse through the molten catalyst to a cooler part of the reaction chamber, where the solubility of carbon drops. This, in turn, enables the carbon to crystallise out of the molten catalyst as diamond.[12]

Another variation of the HTHP method is the use of diamond seed crystals. This provides a pre-existing diamond surface for new growth to occur. The free energy for the formation of diamond with seeds is -20 kJ mol^{-1}, whilst without seeds it is -50 kJ mol^{-1}. Further compounding this, it has been reported that diamonds grown using a Fe-Ni catalyst and seed crystals are 10 – 20% larger, and are also more consistent in size than those grown without.[65]

2.2 NEW APPROACH

2.2.1 High Pressure High Temperature Synthesis Equipment

In order to achieve the high pressures and temperatures required for diamond synthesis, a new type of anvil apparatus has been developed, which utilises four tungsten carbide anvil cells that, when assembled, form a central, cylindrical channel in which the reaction vessel is placed. Each anvil piece is supported by a surrounding
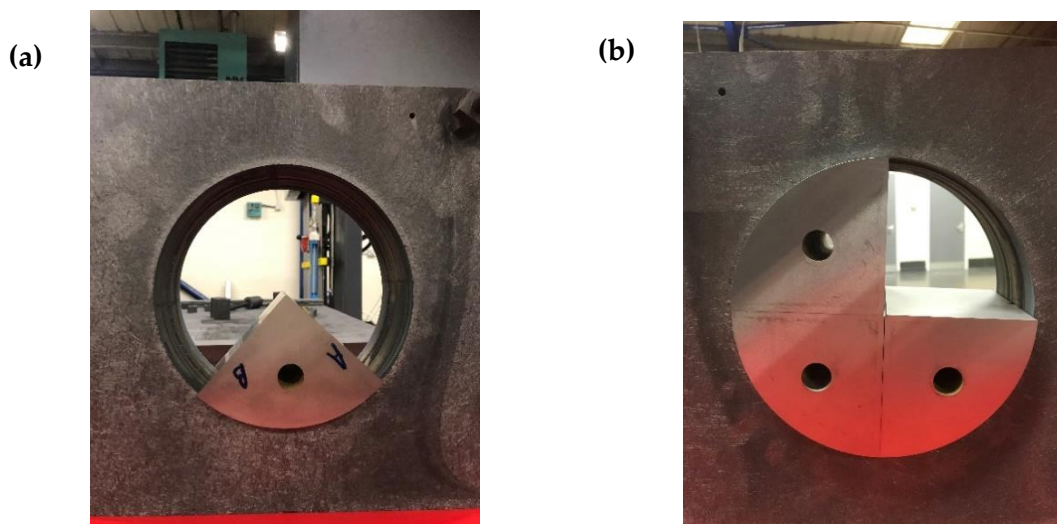
Figure 12: The anvil cell of the HTHP apparatus used for the synthesis of diamond. In (a), a single section of the anvil cell is shown, supported in the CFC framework. In (b), three sections of the anvil cell are shown, with the reaction chamber running down the centre.

framework of carbon-fibre reinforced carbon (CFC), which has a low TEC.[90] Upon heating, the tungsten carbide anvil will expand to a much greater extent than the surrounding CFC framework. This setup allows for the build-up of pressure within the reaction chamber in which the reaction vessel is placed. The reaction vessel itself consists of a zirconium tube, and houses the graphite starting reagent, along with the metal catalyst and two tantalum end caps that act as a pressure medium, a pictorial representation of which is shown in Figure 12.

Once the four anvil pieces are placed in the CFC framework, two tungsten carbide end caps are placed either side of the set-up, and the centre set up is secured using CFC rods and bolts, as shown in Figure 13. Altogether, the apparatus weights 100 kg, and must be moved using a pneumatic lift. Once assembled, it is placed into a high temperature furnace. Prior to any reaction taking place, the furnace is evacuated and flushed with argon three times in order to achieve an inert atmosphere. It is under these conditions that the reaction takes place.

2.2.2 Theoretical Considerations of New Approach

As previously outlined, the apparatus that is currently being developed is composed of a circular, cobalt cemented tungsten carbide, Co-WC, anvil in which the
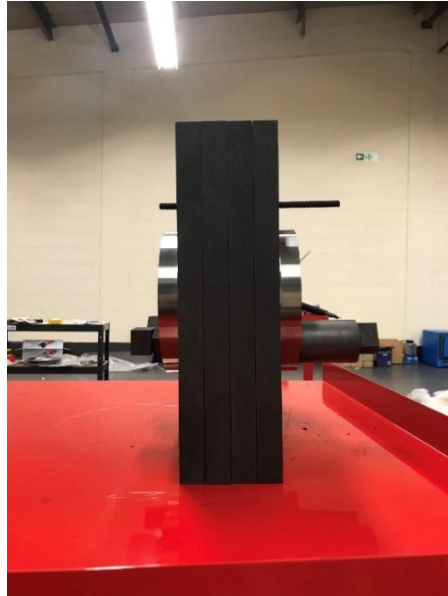
Figure 13: The fully assembled HTHP apparatus.

reaction chamber is placed. At the high reaction temperatures required for the rate of formation of diamond to be appreciable, thermal expansion of these materials will occur, with the level of expansion differing between each material, with this being characterised by their respective TEC's. In essence, it is this disparity between the TEC of the materials that allows this technique to work.

Tungsten carbide is famous for its incredible toughness, so much so it is utilised as armouring for military vehicles, and like most metallic substances, expands at an appreciable level. These properties, when combined, mean that it is able to produce and exert an incredible amount of outward force during this expansion. Whilst this occurs in all directions, it is the radial expansion that is of importance to this process, and thus, this radial force must be contained in order for it to affect the central reaction chamber. One way of achieving this is to place the anvil inside a form of 'belt'. This belt needs to be able to withstand the high temperatures of the reaction, and still be able to withstand the immense levels of exerted stress, σ, whilst also displaying a low level of strain, ε, maximising the miss-match in expansion, and subsequently causing the greatest pressure difference. Moreover, it must also be able to do this elastically, without yielding (aka breaking), which would cause a sudden loss of pressure. These two properties are summarised using a quantity known as Young's modulus, E, with these being defined using the following equations,

$$\sigma = \frac{F}{A} \tag{2.1}$$

$$\varepsilon = \frac{\Delta L}{L} \tag{2.2}$$

$$E = \frac{\sigma}{\varepsilon} \, . \tag{2.3}$$

Here, F is the force that is being exerted over the area, A, and is measured in Pa, highlighting its importance regarding the build-up of pressure. L, meanwhile, is the original length, with ΔL being the length of extension whilst under a given stress. Any increase in ΔL will increase the area A, thus lowering σ, and by extension the pressure. These are both taken into account by E, which, ideally, should be as high as possible for the best result (*i.e.*, a lot of stress with little strain).

One material that possesses the necessary qualities is CFC, which is noted for its low TEC, and high strength, resulting in a high Youngs Modulus.[90] This property makes it the ideal candidate for the belt described above, and, as shown in Figure 14, allows for the forces generated to be contained within the anvil and reaction chamber. This makes the CFC framework a critical component, with the entire concept relying on its ability to withstand the immense tensile stresses required, as well as its resistance to extreme temperatures. Moreover, when the diameter of the reaction chamber is increased, these forces increase dramatically, further exacerbating the already extreme application the framework is subjected to.

Despite having no importance in the actual synthesis of diamond, CFC is very lightweight, and, as such, has been used in many varied applications, such as cars and aircraft, as well as other areas where steel, or similar materials, would otherwise be used.
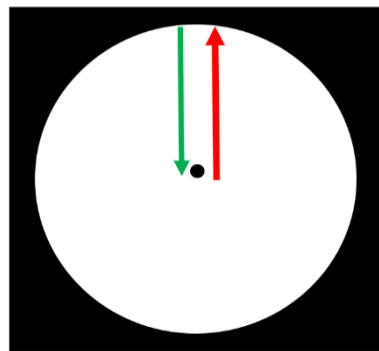

Figure 14: A schematic, cross-sectional representation of the function of the CFC framework (surrounding black square) to contain the outward expansive force (red arrow) of the WC anvil (white circle), and reflect it inwards (green arrow) toward the reaction chamber (central black circle).

Just like other materials, it's construction can be tailored to better exploit the desired property, with this also applying to the diamond synthesis process being developed here.

2.2.3 Materials Used

2.2.3.1 CFC

CFC composites, in the simplest sense, are a network of carbon-fibre (CF) threads that have been adhered (or 'glued') together via a surrounding carbon matrix. This matrix is often formed via the use of a carbon-containing mixture, that is applied in a liquid state, and subsequently cured via various heat treatments. This initial malleability also allows the pre-formed composite to be shaped in various ways, including those with curved surfaces, making them a very versatile material. As a result, the properties of the final product largely depend on the type of carbon fibre used, and the material used to bind this together.

Carbon-fibre, as the name suggests, are fibrous strands of carbon, and can be manufactured in various lengths and thicknesses. This is due to them mainly being composed of hexagonal sheets of graphitic, sp^2 hybridised carbon, enabling them to withstand high amounts of tensile stress. Moreover, they have a good resistance to changes in temperature, with very little change to their properties even at incredibly high temperatures. Much like fibres used for clothing, they can be woven into fabric, in a number of different ways, and have many uses aside from CFC composites. Due to the multitude of potential applications, carbon-fibre is produced on an industrial scale, meaning their cost is far from prohibitive, and they are readily available from many non-specialist suppliers.

Unlike the raw carbon-fibre, CFC tends to be supplied only as the final product. This means that the binding agent used has already been applied and cured, with its composition, method of application and curing process being a closely guarded secret.[91] This is presumably because it can have a significant effect on the quality of the final product, and hence affect the properties of the CFC sample. Despite this secrecy, based on the intended use of CFC in this process, the following properties are required:

- resistance to decomposition at the high temperatures required for diamond synthesis, whilst retaining its strength and rigidity;
- be able to withstand incredibly high pressures;
- resistance to chemical attack in the form of diffusion of metals.

Whilst there are many different types of material that can meet this purpose, a set that particularly stands out is that of thermo-setting polymers. These can be applied in a liquid resin form, and subsequently set to produce the final composite product, making them ideal for this application.

2.2.3.2   Thermoset Resins

Thermosetting resins (TR) were developed during the early 1900's, and were actually the first class of mass produced synthetic polymers in the form of Bakelite.[92–96] Hence, they are of considerable historical importance, far beyond their use as carbon refractory materials, and have helped to shape the world in which we currently live. Generally speaking, TR's are very well researched and documented, with a wide range of uses, including many commonly known materials, such as epoxy resins and vulcanised rubber.[95] A defining characteristic of this class of materials is the irreversible hardening of the starting reagents when subjected to some form of initiator, such as UV light, the addition of a chemical agent, or simply applied heat, during a process known as curing. This irreversible hardening occurs both due the increase in degree of polymerisation, as well as the formation of bonds between adjacent polymeric chains, which is known as cross-linking (CL).[92]

Typically, the initial, uncured polymer chains have a relatively low molecular weight, M_W, of < 1,000 g mol^{-1}, meaning they're often low-medium viscosity fluids or solids. These properties are dependent on the specific molecular structure of the polymer, with the main factors being the initial degree of polymerisation and level of cross-linking present before curing, as well as any additives that are used.[93,95] Due to the fact that there is already a degree of polymerisation present in the pre-cured phase, these compounds show very low levels of mobility, and are unlikely to flow away from where they were originally applied.[92]

TR's, following the curing process, are renowned for their stiffness, rigidity and chemical resistance.[94] The degree at which a given TR displays these traits depends on the chemical structure of the TR, as well as the type of bonding between monomers. Unlike other, none cross-linked polymers (referred to as thermoplastics), once they have started to cure, thermoset polymers do not re-exhibit a plastic or molten state, instead undergoing thermal decomposition once within a given temperature range. This results in products with a high 'green' mechanical strength, which is the strength of the sample whilst only part way through curing, meaning the partially formed composite is able to reach a maximum degree of polymerisation prior to any pyrolysis. Moreover, the semi-processed sample is able to keep it's shape and be safely handled, which is crucial as the initial, lower temperature treatment can take place in a standard furnace, whilst the final high temperature treatment must take place in an inert atmosphere, and can be safely stored for a period of time between these steps. Furthermore, this high green mechanical strength proves advantageous when using the cured resin as a binder for more typical, metal oxide refractory materials, allowing for the generation of a comparatively significant carbon yield after the full heat treatment.[97,98]

The char yield is a measure of the mass of residual carbon present following pyrolysis when compared with its initial weight, and is a crucial quantity when analysing the effectiveness of any potential compound. As outlined above, the higher the carbon yield, the better suited the TR is as a carbon source whilst forming the CFC composite.[99] Another crucial factor is structure of the monomers, as well as the backbone connecting these together. For example, any oxygen or aliphatic carbon portions highly favour the formation of volatile compounds, which, upon formation, can rupture the polymeric network, lowering the resulting char yield.[100–102] Hence, for the best possible char yield, polymers formed using symmetric, oxygen free monomers, with multiple polymerisation sites should be chosen. This will limit the level of carbon lost due to the evolution of volatile compounds, and will promote a high level of CL, resulting in a more extensive, compact carbon network upon curing, and a higher char yield following pyrolysis.[103] Based on these requirements, phenolic based TR systems are the most favourable for the formation of CFC composites, giving the highest char yield when compared to different types of polymers, with experimental evidence confirming this.[99]
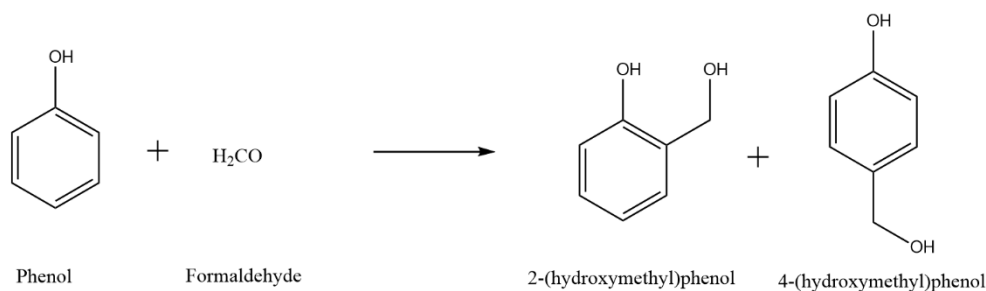
Figure 15: The initial condensation reaction between phenol and formaldehyde, giving two differing isomers.

Furthermore, when choosing a carbon-based refractory material for other, industrial applications, phenolic TR's are by far the most used.[97,98,104] As shown in Figure 15, they're easily synthesised via a condensation reaction, using cheap, easily attainable materials.

2.2.3.3   Formation of Pre-polymer Resin

When forming phenolic resins from phenol and formaldehyde, it is, in reality the (hydroxymethyl)phenol (HMP) isomers that act as the true monomers within the process. As multiple isomers can be formed depending on the position of substitution, this poses some interesting implications on the precise condensation process that forms the resoles. In the broadest sense, the addition of formaldehyde to phenol is a process known as electrophilic aromatic substitution (EAS), the mechanism of which presents some interesting insights when forming HMP isomers (Figure 16). Generally speaking, EAS comprises of two main steps, electrophilic attack of the aromatic ring, forming a carbocation (C.C.) intermediate, followed by an elimination step, forming the final product.
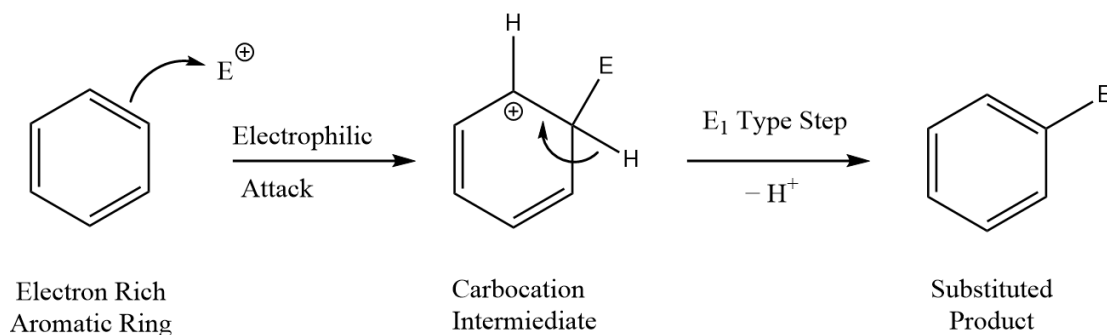
Figure 16: The general mechanism for electrophilic aromatic substition between an electrophile, E^+, and unsubstituted benzene.
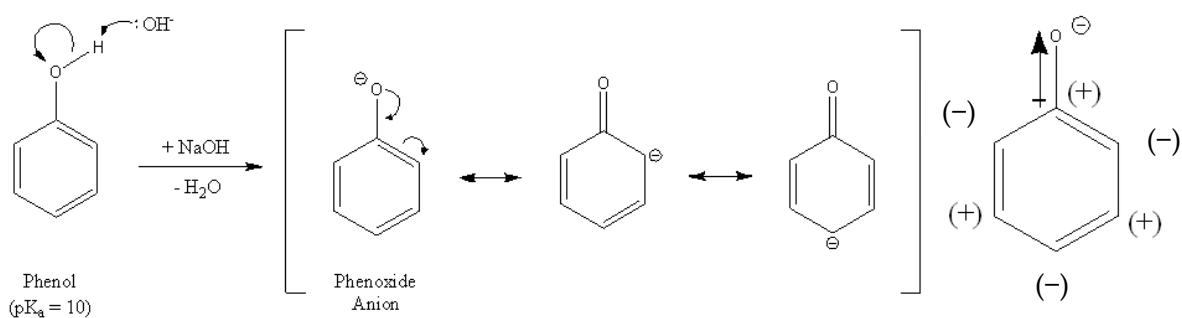
Figure 18: Hydroxide mediated formation of the phenoxide anion, and the resultant effective charge on the aromatic carbon ring.

When using phenol, the EAS mechanism is further complicated by the presence of an oxygen atom bound to the aromatic. Here, the oxygen p-orbital resonance stabilises the ring by taking part in conjugation and 'activating' the ring. This has the effect of increasing the electron density of the *ortho-* and *para-* positions, making them much better suited to attack the electrophile. Owing to the high electronegativity of oxygen, there is a dipole moment present across the molecule, meaning the upper three carbon atoms will have a higher level of electron density than the lower two. This means that the (+) carbon bonded directly to the oxygen will produce a more stable C.C., hindering the deprotonation step, therefore lowering the reactivity of the *ortho-* sites compared to *para-* (Figure 18). This is reflected in the addition rate constants, as the rate of formation of the 4-isomer is approximately double that of the 2-isomer (10.5×10^{-6} vs. $6.2 \times 10^{-6}\,M^{-1}\,s^{-1}$).[91]

Figure 17: A schematic representation of the electron withdrawing effect of the hydroxymethyl group (EWG), alongside the resulting effective charge on the aromatic carbon ring.

55

Following the addition of formaldehyde and the formation of a hydroxymethyl group bound to the ring, further inductive effects arise. Due to the electronegative oxygen atom bonded α to the ring, the hydroxymethyl group acts as an electron withdrawing group (EWG, Figure 17). As such, sigma effects ar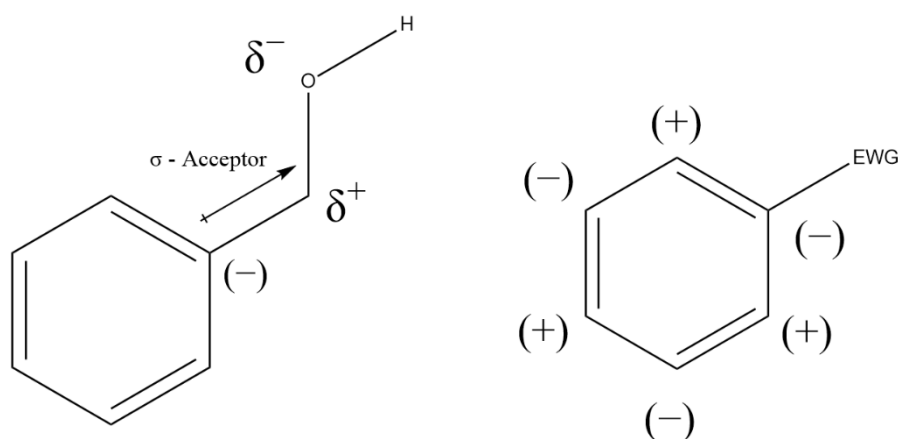ise, and further impact the electron density throughout the ring. When amalgamating these two different relative inductive directions to find a resultant dipole, the two HMP isomers produce two different results. For 2-HMP (Figure 19(b)), these are both pointing 'upwards', in directions that are offset by 120°. Combining these two vectors roughly gives the arrow in red (note the phenolic O will have a stronger effect on direction). This creates two separate areas in the molecule, one side with a higher electron density. Whilst this will have little effect on the electrophilic attack during addition reactions, this will have a considerable effect on the stability of the C.C., and therefore the corresponding elimination step. This, in part, explains the higher reactivity of this isomer.

4-HMP, however, has these inductive effects in different directions, meaning the vectors will cancel (Figure 19(a)). This will result in a higher electron density throughout the ring, and will therefore stabilise any carbocations that form. This will not only hinder addition of formaldehyde and therefore the amount of substitution, but also the
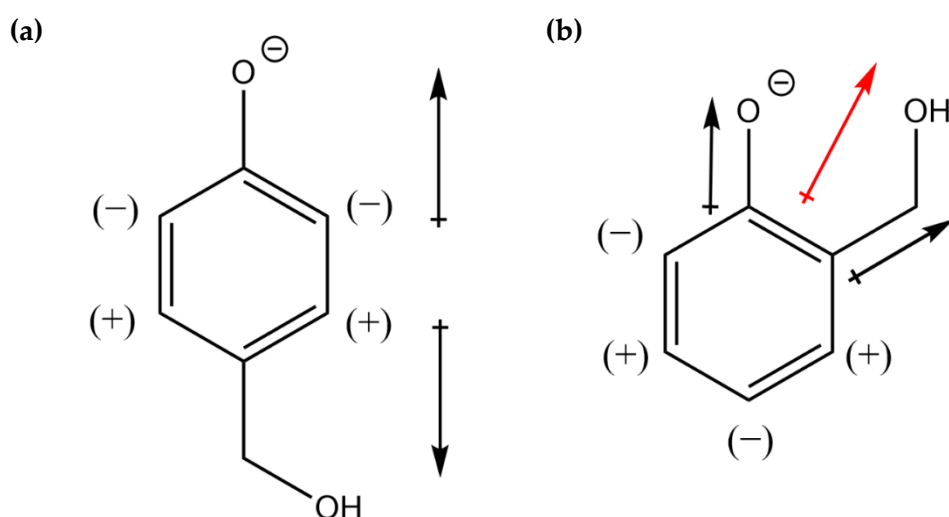
Figure 19: The overall electronic effects of hydroxy methylphenol on a phenoxide ring when in the (a) para position (4-HMP), and (b) ortho- position (2-HMP). Here, the black arrow represents the pull of electron density by the bonded groups, with the red arrow indicating an additive, overall effect of the two groups combined.
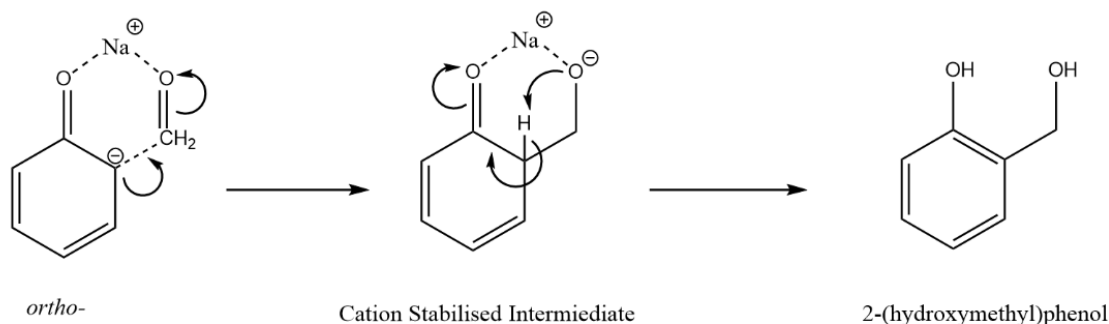
Figure 20: A general mechanism for the EAS of formaldehyde to phenol in the presence of a co-ordinating sodium cation.

formation of methylene bonds. Ether linkages, however, will be unaffected. This difference in structure causes a different starting reactivity and will therefore have a knock-on effect on the products produced. Note that for the addition of formaldehyde to phenol, the 4-isomer product, 4-HMP, is kinetically favoured and will form in a higher quantity.[91]

These addition and condensation processes will also be influenced by the type of catalyst present. Any cation present can co-ordinate with the oxygen lone pairs present in the formaldehyde, phenolic oxygen, or hydroxymethyl species present (Figure 20). In doing so, it is acting as a Lewis acid, and will further pull electron density towards these atoms, and away from any adjacent carbon systems, further exacerbating the effects mentioned above. Once the HMP species have been formed, they then undergo
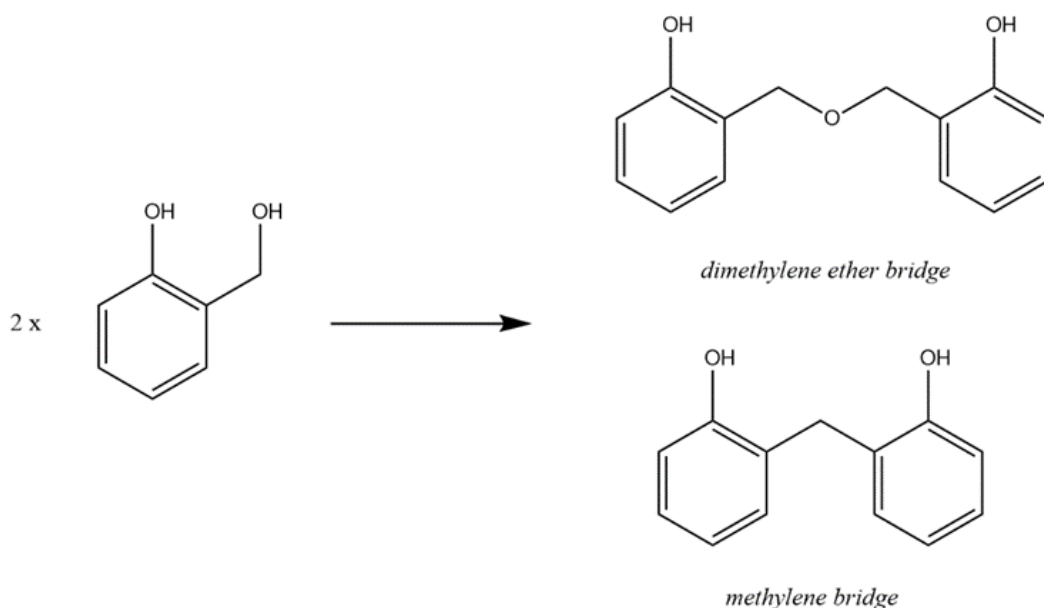
Figure 21: The two possible products that form following the condensation of two HMP monomers.

polymerisation via a condensation mechanism, that ultimately forms the desired phenolic resin. During the addition phase, two differing process can occur, either, a hydroxymethyl group can react with a free benzene position, or it can react with another, already substituted hydroxymethyl group (Figure 21).

Unlike the EAS process forming the active hydroxymethyl sites, these are condensation reactions, involving nucleophilic substitution of the -CH$_2$OH sites, resulting in the formation of H$_2$O as a by-product. Whilst the precise mechanism for the formation of both bonding types differs slightly, at the lower temperatures usually used when synthesising phenolic resins, they are both most likely S$_N$2 processes, meaning that a transition state is formed during the process. Importantly, when performed in the presence of a catalyst, this will have the most pronounced effect on the *ortho-* positions. However, during the condensation phase, this will have a larger effect on polymerisation at the *para-* position (Figure 22). Moreover, this structural difference and associated electronic effects pose potential differences when HMP monomers are condensing together, as, in order for the methylene bridges to be formed, there must be an empty addition site at the 4-isomer. Interestingly, it is reported throughout the literature that *ortho-ortho* methylene bridges are generally not formed, with ether bridging being much more common in this position.[105,106] The mechanism resulting in ether bridges is, on the other hand, somewhat debated. However, at temperatures above 120 °C, it is believed to proceed through *ortho*-quinone-methide in a two-step process, and occurs via the intra-molecular loss of H$_2$O.[105] This can be offset by using a M(OH) catalyst, such as NaOH, as well as by lowering the amount of formaldehyde used, as this will reduce the level of unwanted condensation reactions between hydroxymethyl groups. However, both methylene bridges, as well as ether bridges, will be formed during the polymerisation
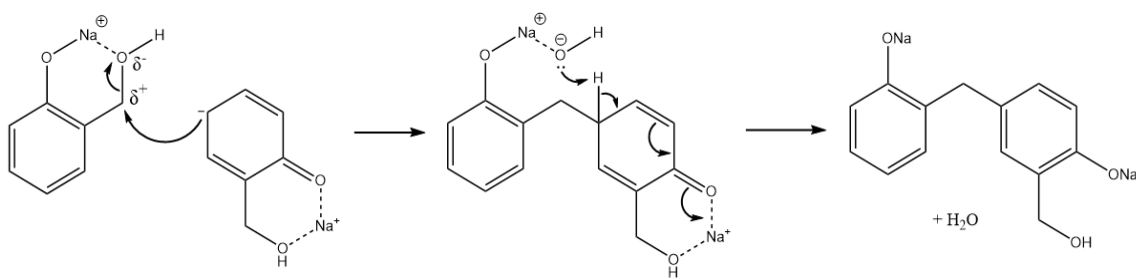

Figure 22: A general reaction mechanism for the NaOH catalysed condensation between two 2-HMP monomers to form a methylene bonded dimer.

process, with the latter being detrimental to formation of graphitic carbon networks following pyrolysation. As such, when synthesising resins for use in the manufacture of CFC, the reaction conditions must be modified and optimised to maximise formation of the desired methylene bridging.

2.2.3.4   *Phenolic Resin Formulation and Curing*

Once the pre-polymeric resin has been synthesised, this must then be applied to the CF and fully cross-linked in a process known as 'curing'. The ability of a sample to do this efficiently is dictated by the rheological properties of the resin being applied, and visco-elasticity measurements give an indication of the pliability of a resin onto a fibrous substrate. For example, the recommended viscosity for synthesised phenol-formaldehyde resin that makes it easily applicable on fibre as a laminating material was approximately 400 – 600 cP.[107] Achieving this can be done in a variety of ways, and by altering different reaction parameters. All of these must be taken into account simultaneously, as it has been shown that different formulations required different synthesis times to achieve a specific viscosity, whilst others alter the ratio of starting materials in relation to the reaction temperature. For example, it has been shown that increasing the formaldehyde molar ratio will shorten the gel time or the time required by the resin to cure.[107]

Generally, it is accepted that the largest influences of fluid properties are the molar ratios of phenol and formaldehyde used in the starting reaction, the synthesis temperature and time, as well as the pH of the mixture (determined by the amount of base added). This is owing to the possible rapid changes in viscosity due to the known exothermic nature of the reaction, particularly at high temperatures.[108] Synthesised resins with a viscosity in excess of 600 cP were found to be very viscous and, by extension, very difficult to be applied to the CF material. Therefore, during the actual synthesis process, the reaction time can be tailored accordingly based on the required viscosity, which defines the molecular weight of the oligomeric resin produced, provided that the temperature and molar ratio of phenol to formaldehyde are given. Conversely, this must be done at the correct temperature for the molar ratios used, as if the heat supplied is not sufficient to overcome the activation energy of the

polycondensation reaction, then the cross-linking network might not occur entirely, resulting in a thin solution of linear phenolic resin pre-polymer with low molecular weight.[109] This is shown by the shear thinning behaviour of resins produced at 40 °C when compared with the shear thickening behaviour of the same resins made at > 60 °C.[107]

2.3   CHARACTERISATION METHODS

A common technique used to determine the structure of carbon-based materials is Raman spectroscopy. Alongside the similar, and often complementary technique of infra-red (IR) spectroscopy, Raman spectroscopy exploits the quantum mechanical nature of inter-atomic bonding, and is useful in the analysis of gases, liquids, and solids. Often referred to as vibrational spectroscopy, particularly experiments involving infra-red, both techniques utilise the molecular vibrational behaviour of a system, which broadly depends on the masses of the atoms present, as well as the strength of the bonding between them. Hence, despite diamond and graphite both being allotropes of carbon, and therefore having the same atomic mass, the differences in bonding between the atoms can be exploited and characterised using spectroscopic methods.

2.3.1   Vibrational Spectroscopy of Carbon Samples

A number of factors affect the spectra obtained via Raman spectroscopy. The difference in energy of the incident photon and the scattered photon is known as the Raman shift, and is often quoted in wavenumbers. A key factor affecting this is the temperature of the sample. At low temperatures, the energy change that causes the Raman effect is a stokes process caused by the emission of a phonon. Therefore, the emitted photon will be lower in energy. At higher energies, the thermal energy in the crystal will cause phonons to already be present, with their energy allowing an anti-stokes process to occur.[110] For experiments at room temperature, the dominant process occurring is the stokes process.

Generally speaking, the number of peaks present in a spectrum depends on the number of Raman active modes. This, in turn, is dependent on the symmetry of the compound being analysed, with lower symmetries corresponding to a higher number of

peaks. The symmetry of a crystal is characterised by its point group, which is used to determine the vibrational modes it can exhibit, with the Raman (and IR) activity of these vibrational modes also being determined by this.[111]

As Raman activity requires a change in polarisation of the bonds present, the light source used tends to be slightly higher in energy than for IR activity. Often, the energy used will be on the order of the electronic transitions of the bonding electrons, which is roughly on the order of visible light (400 – 750 nm).

2.3.1.1   Experimental Raman Spectra

Diamond

Specifically, diamond belongs to the cubic space group *Fd3m*, and has two atoms in its primitive unit cell. As a result, this means that there is only one, triply degenerate vibrational mode present with T_{2g} symmetry. As diamond has a face centred cubic lattice, its' point group is O_h, which indicates that this mode is Raman active. Conversely, there are no IR active modes.[112] The associated Raman shift occurs at 1332 cm^{-1}, and appears as a sharp, well defined peak (linewidth ~ 2 cm^{-1}) in the Raman spectrum, as demonstrated in Figure 23.[112–114]
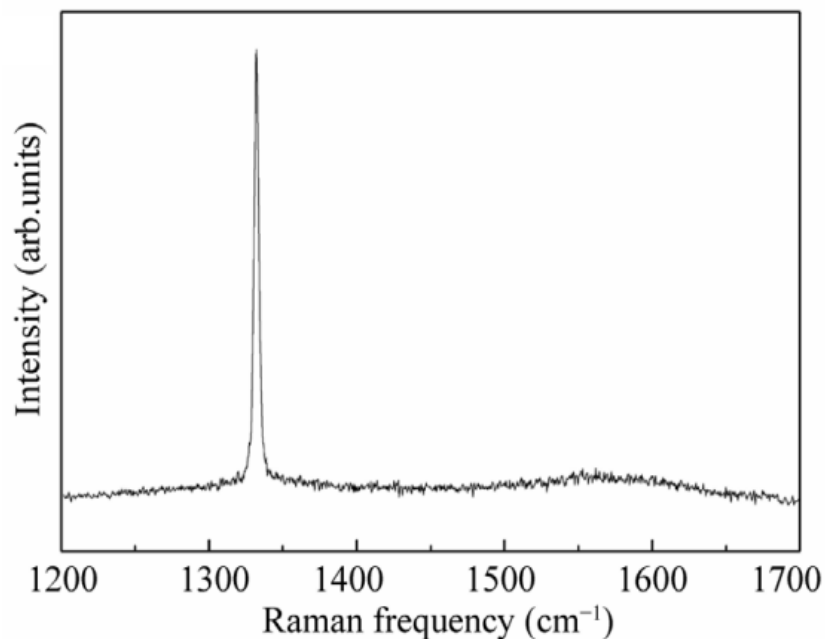
Figure 23: Raman spectrum obtained on the surface of a [001] diamond crystal.[113]
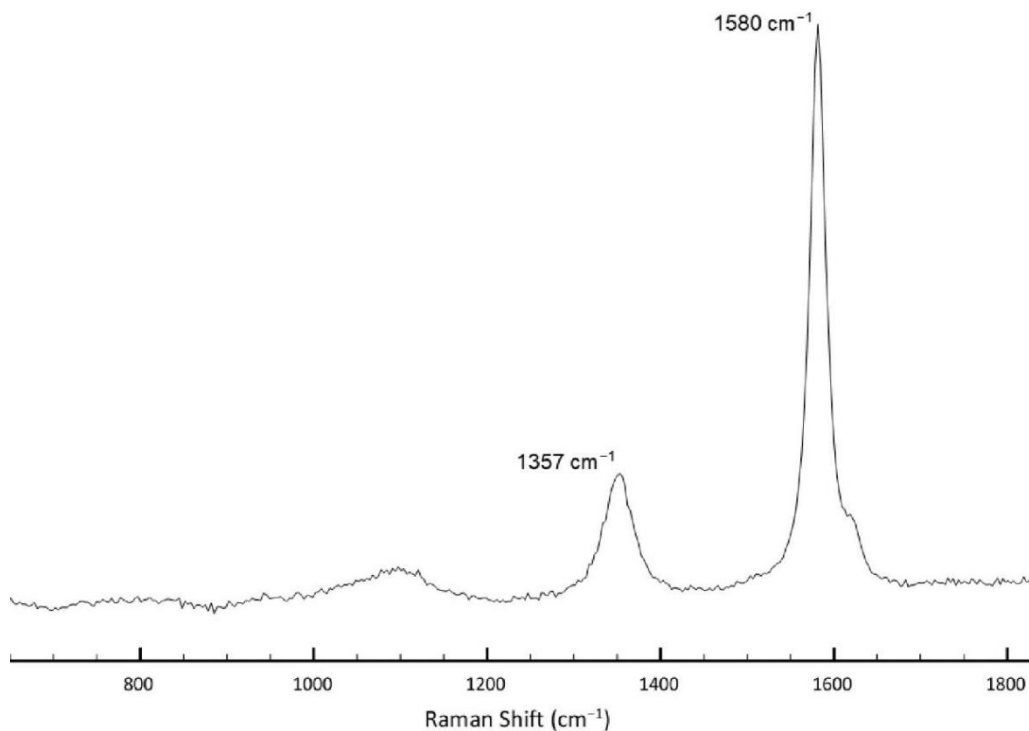
Figure 24: An example of a Raman spectrum of a polycrystalline graphite sample. The main peak at 1332 cm^{-1} is due to the E$_{2g}$ stretching mode, whilst the smaller peak at 1357 cm^{-1} is due to a break down in symmetry at the crystal boundaries.

Graphite

The structure of graphite can be characterised by the space group *P6$_3$/mmc*, and belongs to the point group D$_{6h}$. Examination of the space and point groups for graphite reveal that there is a single, doubly degenerate, Raman active mode present, with E$_{2g}$ symmetry. This vibration occurs along the graphene planes, and is therefore independent of the stacking sequence. This causes a sharp peak at 1580 cm^{-1} in the Raman spectrum. Interestingly, for polycrystalline samples, another smaller peak is observed at 1357 cm^{-1}, as shown in Figure 24. Initially, this caused considerable debate in the literature as to why it occurs, however, it has since been attributed to a loss in symmetry at the crystal boundaries.[112]

PCD

The ability of Raman spectroscopy to easily differentiate between allotropes of carbon lends itself nicely to the analysis of PCD. For instance, the ability to identify different phases within a sample can be used to confirm the presence of any

graphitisation[50] of the diamond surface caused by high temperatures. In contrast to single crystal diamond, the Raman linewidths produced by PCD are usually much broader, with the observed Raman shift value differing depending on various factors.[86] For example, peaks tend to be very sensitive to the sintering temperature used to produce the PCD sample, as well as the initial diamond grain size and the inclusion of any additives.[115]

In addition to this, as the Raman effect is based on the bonding between atoms, things such as bond stress can also be quantified by examining any differences between measured and theoretical peaks. For example, the quality of PCD tools is usually evaluated by scanning electron microscopy (SEM) for surface roughness, sharpness of cutting edge and facial defects such as fracture and cracks. However, otherwise invisible defects of residual stress and graphitisation can considerably affect the quality of the machined PCD surface.[50] Whilst under a given level of external or thermal stress, the expected peak could be shifted away from the equilibrium position as the local environment of the carbon atoms is altered by the reduced or extended atom distance.[86]

2.3.2 Electron Microscopy

Alongside Raman spectroscopy, the experimental characterisation of PCD has traditionally been based on scanning SEM.[47] Briefly, this technique uses a focused beam of electrons to produce detailed, high-resolution, magnified images of a surface. The electrons are produced via an electron gun, which are then accelerated via a positively charged plate placed behind the sample, and are focused using a series of electromagnetic coils onto a point of ~10 nm. Due to the de Broglie wavelength of this electron beam being much shorter than that of visible light, a much higher level of magnification and resolution can be reached. This lends itself to the inspection of topography at very high magnification levels, often up to 300,000 times, and can be used to analyse cracks and fracture at surfaces, as well as minute physical defects or the sizes of micron sized particles. The voltage used to produce this acceleration is known as the 'acceleration voltage' (AV), and is of great importance. Often, energies between 200 V and 30 keV are used, with a higher AV enabling greater penetration into the sample,

making the interacting volume of the sample greater, with this coming at the expense of the final resolution.

Choosing the correct AV is critical in obtaining a good, clear image, with this mostly depending on the type of sample being analysed. Generally speaking, the more electrically conductive the sample, the higher the required AV. Higher voltages generally allow for higher resolution and magnifications, often at the risk of rapidly damaging the sample if it is not highly conductive. For example, when imaging polymers and ceramics, AV's of less than 10 keV are used. Another negative consequence of using higher voltages is a loss of surface structure detail.

Another factor to consider when utilising SEM is the working distance (WD), or the distance between the final aperture of the focused beam and the sample. Generally, a WD of ~10 mm will allow for a good depth of field within the final image whilst simultaneously maintaining good resolution, although a reduction in this value may be desirable when working with lower AV's. Alongside this is the spot-size of the focused beam on the sample. This restricts the beam current, thereby causing alterations to the brightness and contrast. Smaller spot sizes will require higher brightness and contrast, with this ultimately acting as a lower limit. Typically, smaller spot sizes allow for higher resolution and a greater depth of field.

Upon interacting with the sample, two differing processes occur, producing either high energy back-scattered electrons (BSE's), or lower energy secondary electrons (SE's), with these requiring different detectors. SE's are re-emitted by the atoms present at the surface of the sample, as their much lower energy (< 50 eV) limits their ability to penetrate through a sample to a few nanometers.

BSE's, on the other hand, are electrons that have been reflected following the interaction between the primary electron beam and atoms contained in the sample. Originating from within the sample itself due to their much higher energy, BSE's arise from elastic collisions, and can give information about the composition of the sample that produced them. As a consequence of their higher energies, these can originate from within a sample, with this conversely causing a drop in resolution of the image produced

when compared with SE's, but are still able to resolve topological atomic nuclei down to around 1 μm.

When imaging a sample, there are many factors that can influence the quality of the final image. Often, improper sample preparation and external influences such as magnetic fields and mechanical vibrations are the most common problem sources. These disturbances can manifest in several ways, such as a lack of sharpness, signal noise and subsequent image deformations, as well as a general low-quality image, although these can be identified and corrected with relative ease.

2.3.2.1 SEM of PCD based samples

Due to the qualities outlined previously, this technique lends itself to the analysis of HTHP produced PCD diamond samples. SEM can be used to observe the micro morphology of the diamond layer and the diamond/binder phase interface.[49] In addition to this, due to the high levels of magnification in conjunction with a good level of resolution, SEM can also be used to analyse the particle size of diamond grains within a powdered sample (Figure 25). In turn, this provides a quick analysis method for the screening of precursors prior to undergoing the sintering process, as both of these qualities are of importance to the properties of the final product.
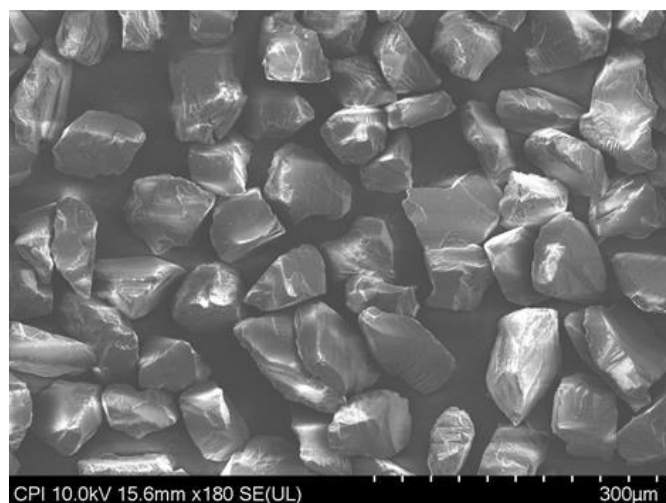
Figure 25: SEM image of natural, 270 μm diamond powder used in the manufacture of PCD.

3   EXPERIMENTAL AND SYNTHETIC METHODS

3.1   PCD SYNTHESIS

Four cobalt cemented tungsten carbide anvils were placed into a surrounding FS740 carbon-fibre carbon framework (sourced from CFC Design). A central reaction chamber comprised of wonderstone pyrophyllite was filled with 99.8%, 2 μm cobalt powder (15 wt.%, sourced from APC Pure), alongside 8 – 12 μm diamond powder (42.5 wt.%) and 230 – 270 μm diamond powder (42.5 wt.%), both placed at opposing ends. This was heated in an inert argon atmosphere to 1540 °C, where it was held for 10 minutes, and subsequently allowed to cool naturally to room temperature. Following this, both the PCD composite, labelled PCD-a, as well as the pyrophyllite reaction chamber, labelled RC-a, were retrieved for further analysis.

Following analysis of PCD-a, the process detailed above was repeated using an identical apparatus set-up and ratio of starting materials. However, the heating profile was altered slightly to include an additional hold at 1000 °C for 35 minutes prior to heating to the maximum temperature of 1540 °C, producing another PCD sample, labelled PCD-b. The PCD-b composite was then laser-cut, and the resulting surface polished via ion beam milling (IBM) at an offset of 88°, with a power of 6 kV for 1 hour. The pyrophyllite reaction chamber, labelled RC-b, was also retained for analysis.

This altered process was repeated using pure tungsten anvils in place of the previous cobalt cemented tungsten carbide anvils. The sample produced, labelled PCD-c, was retained for analysis alongside the pyrophyllite reaction chamber, labelled RC-c.

3.2   RESOLE SYNTHESIS

3.2.1   Preliminary Testing

NaOH (1.6 equiv.) pellets were dissolved in distilled water (10 mL) at room temperature under constant stirring, forming Solution 1. Phenol (10 g, 0.106 mol) was added to a round-bottom flask, alongside 37% aqueous formaldehyde. This was then fitted with a Dean-Stark condenser, and the mixture was heated to the desired reaction temperature (70 or 90 °C) under stirring, and Solution 1 was added to the vacant neck

whilst under heavy argon purging, starting the reaction. As this occurred, the reaction mixture went from colourless to a pale yellow, and then to a deep ruby red. After 40 minutes, the reaction was removed from the heat source, and allowed to cool naturally. A yellow/red solution remained. Any remaining water and other volatiles were removed via rotary evaporation, leaving a pink, powdery solid in the reaction vessel. This was then mixed with dichloromethane (50 mL) forming a slurry, with the solid precipitate being removed via filtration, and the solid being allowed to dry under vacuum. The solid product was then washed with methanol (3 × 50 mL) to remove any unreacted starting materials, and again allowed to dry under suction. The solid was then transferred to a vacuum desiccator, and allowed to dry overnight, leaving a soft solid lump of pink material, which was collected for further use and analysis. This process was then repeated using 2-HMP and 4-HMP, both as separate starting reagents, and as a 1:1 mixture.

3.2.2 Synthesis of Pre-resin

2-HMP or 4-HMP (1 equiv.) was added to a beaker, alongside NaOH pellets (1.2 – 1.6 equiv.) and equipped with a stirrer bar. To this, isopropyl alcohol (10 – 20 mL) was added, with this mixture being heated under stirring to 60, 70 or 80 °C. Once the desired temperature had been reached, 37% aqueous formaldehyde (1 – 2.5 equiv.) was added, and then allowed to react for 30 minutes. Following this, the mixture was removed from the heat source, and collected in a sample vial for further analysis and application to the CF tape.

3.3 CFC MANUFACTURE

To test the adhesive strength of the binder samples, opposite ends of unidirectional CF strips (30 × 5 cm) were looped round a metal sheet, and bound together to form a lap-joint with an aimed overlap of 1 cm. The ends of the test strips were saturated with uncured mixture of adhesive, and once correctly aligned, were compressed under another metal plate with additional mass applied. These were then kept under compression whilst air dried overnight, and subsequently cured at 130 °C for 4 hours, followed by a further 2 hours at 260 °C. Following this, the fully glued samples were then allowed to cool naturally to room temperature for further strength testing.

Strength testing was performed on an internally designed and manufactured testing rig, with the samples being pulled under tension until breaking. The maximum force was recorded, and used to determine the highest tensile stress before failure.

3.3.1 Commercial Glue Testing

A mass (M_g) of Graphibond 551 N was added to a beaker, and mixed with isopropyl alcohol (IPA, V_I) according to the manufacturers instructions. The volume of IPA added was calculated to give volume percentages (%V) of 30, 35, 50 and 75%V. Once diluted, samples were taken for further rheological testing, with the remainder being applied to CF tape.

3.3.2 Internal Glue Testing

When investigating the *in-situ* use of the resole pre-resin, the samples produced in Section 3.1.1 were applied to CF tape following the same method outlined above.

3.4 CHARACTERISATION

3.4.1 IR

All samples were analysed using a PerkinElmer Frontier FTIR with a Specac extended range diamond puck ATR accessory. All phenolic resin samples were applied in their unadulterated liquid state, whilst all cured Bakelite samples were ground into a fine powder prior to analysis. Analysis of the pyrophyllite gasket materials, both before and prior to use in the HTHP apparatus, were also ground into a fine powder prior to analysis.

3.4.2 NMR

Liquid state nuclear magnetic resonance (NMR) spectra were recorded on a Bruker Avance III-HD-400 spectrometer with operating frequencies of 400.07 MHz for ^{1}H, and 100.60 MHz for ^{13}C. Acquisition times for ^{1}H and ^{13}C were 1 and 10 minutes, respectively.

Methanol-d_4, 99 atom% deuterated methanol (purchased from Apollo Scientific) was used as a solvent. The signals produced by the resins were referenced to the central

resonance line of methanol, with a value of $\delta = 49.0$ ppm.[116] The solvents containing aromatic groups could not be used because of a possible overlap in the aromatic region and possible reactions with the samples themselves.[117]

3.4.3   Powder X-ray Diffraction

All powder X-ray diffraction (PXRD) patterns were acquired using a Bruker AXS D8 Advance GX003410, fitted with a Lynxeye Soller PSD Detector. The X-ray source was provided by a Cu tube, that produced a mixture of both $K_{\alpha 1}$ and $K_{\alpha 2}$ with a wavelength of $\lambda = 1.5406$ Å. The samples were ground into a fine powder, and the reflected X-ray beam was passed through a Ni filter equipped with variable slits set at 6 mm, with the reflected data being recorded in Bragg-Brentano θ-θ mode.

3.4.4   Raman Spectroscopy

All Raman spectra were acquired by the Centre for Process Innovation (CPI), NetPark, Sedgefield. Raman spectra were obtained using a Renishaw inVia Qontor Confocal Raman spectrometer. The best conditions obtained during this work was using the 532 nm laser source at 50× magnification with laser set to 10% power, accumulation time of 4 s. Higher powers induced too much background fluorescence and risked burning the sample.

3.4.5   SEM Imaging

Samples were prepared for SEM imaging by coating an adhesive carbon tab with a small amount of sample material. A Hitachi SU8300 FEGSEM was used in secondary electron mode at 5.0 kV and approximately 8 mm working distance to take a range of images.

4 RESULTS AND DISCUSSION

4.1 PCD SYNTHESIS

All analytical work involving Raman spectroscopy and SEM was carried out at CPI, based in The Neville Hamlin Building, NetPark, Sedgefield, UK.[118]

4.1.1 SEM and Raman Analysis

Initial experiments to prepare PCD used a reaction temperature of 1540 °C, as this is known to be well above the melting point of the cobalt catalyst at 1490 °C.[119] This ensures that it is able to fully liquify and adequately spread through the mixture, wetting the diamond particles and fulfil its role as a binder. Following this initial trial run using the new apparatus, the composite product produced, PCD-a, was analysed via SEM and Raman spectroscopy (Figure 26) to try and ascertain its composition and quality. SEM imagining of the unadulterated sample surface showed evidence of diamond crystals, although clusters of surrounding cobalt (indicated by brighter areas in the back scattered electron (BSE) image in Figure 26(b)) made it difficult to establish whether any diamond growth occurred, or if diamond-diamond bonds had been formed. Despite this, it was a good indication that the cobalt catalyst had managed to disperse thoroughly throughout the mixture, making it suitable for its intended use as a binding material.

By combining the data collected from the BSE images with a technique known as energy dispersive X-ray spectroscopy (EDX), it was possible to determine the relative amounts of carbon and cobalt present in the unadulterated PCD-a sample. This resulted
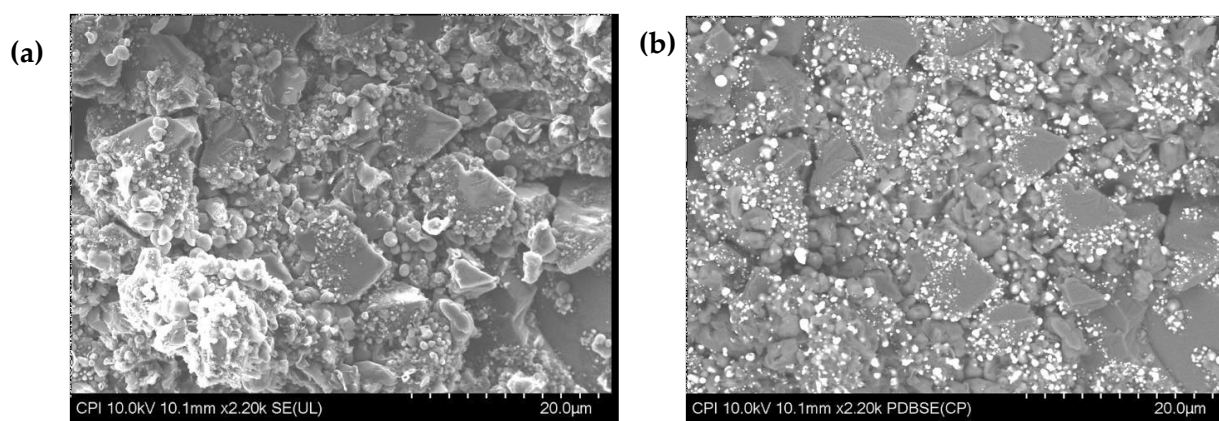

Figure 26: SEM (a) SE image, and (b) BSE image, of the unadulterated PCD-a surface.

in an initial composition of 94.6 wt.% of carbon, alongside 5.1 wt.% of cobalt, with the remaining 0.3 wt.% being comprised of various impurities. As outlined in Section 3.1, the actual cobalt composition of the material loaded into the reaction chamber was much higher, at 15 wt.%, meaning that the composition of the unadulterated surface is not fully representative of the sample.

To determine the exact nature of the carbon identified via SEM and EDX, a Raman map of a random section of the unadulterated sample was obtained (Figure 27).[118] A diamond peak was observed at 1332 cm^{-1}, as well as a much more intense peak at 1580 cm^{-1}, also indicating the presence of graphitic carbon throughout the sample.[112] By comparing the ratio of the peak areas of these two signals, it is possible to determine the quantity of diamond vs. graphitic carbon within that particular piece, with a higher number representing a lower proportion of unwanted graphitisation. Using this method, it was determined that this ratio varied between 0.25 – 0.56 throughout the mapped area, meaning that a considerable amount of graphitic carbon was present. However, it is noted that Raman spectroscopy is only suitable for analysis of the sample surface up to approximately 90 nm. As such, any diamond present below the cobalt covered surface would not be detected via this method, meaning this is also not fully representative of the entire PCD sample. When combined with the short comings identified following the compositional determination via SEM analysis, it became apparent that further processing of the sample was required to accurately characterise the composition of the PCD piece produced.
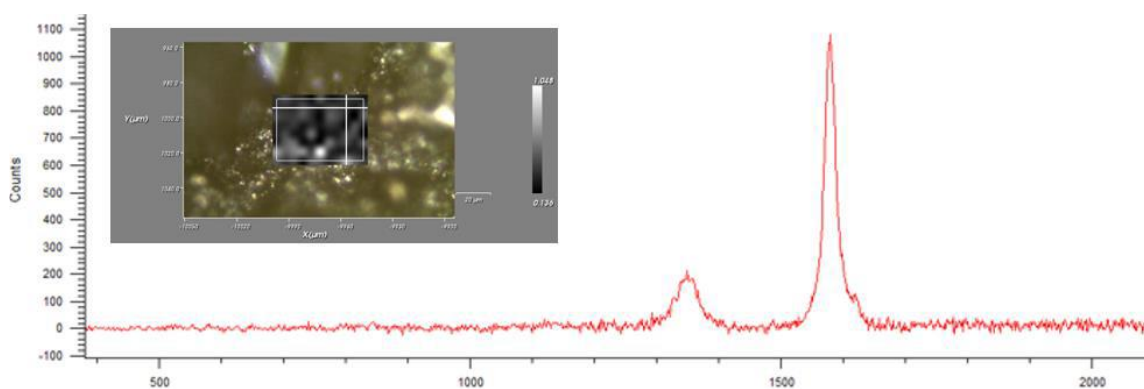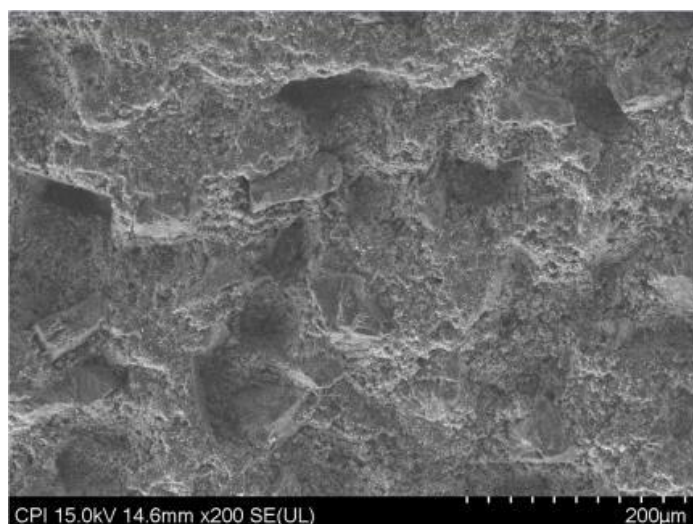

Figure 27: The Raman spectrum obtained for the flat, unpolished PCD-a surface showing both the characteristic peaks for diamond (1332 cm^{-1}) and graphitic carbon (1580 cm^{-1}).

Figure 28: An SEM image of the PCD-a surface following abrasive polishing with a silicon-carbide abrasive, showing apparent voids across the sample.

Whilst there are various methods that can be used to better prepare the sample for analysis, there are several factors that must be considered when choosing the most suitable method. Due to the incredible hardness of diamond, simple abrasive polishing would present various issues, as the material used to accomplish this will inevitably be softer. Whilst this was attempted on our samples using silicon carbide based sandpapers, SEM images of the produced surfaces indicated that the diamond grains had simply been torn away from the matrix, causing multiple voids to be generated, as shown in Figure 28.[118] This also results in poor definition in the SEM. This is evident when the images obtained in Figure 26 are compared to those in Figure 28, where diamond grains are no longer distinguishable in the sample. This presents additional problems, as the PCD sample was initially synthesised with both smaller 8 – 12 μm and larger 230 – 270 μm diamond powder. Hence, the lack of resolution to adequately focus on the smaller diamond grains in the sample hinders any accurate analysis.

Based on the previous SEM and Raman analysis for the unpolished PCD-a surface, it was determined that a flat cross section was needed to improve the quality of these measurements, and to provide data that is more representative of the sample. One of the ways to achieve this is a polishing technique known as ion-beam milling (IBM). The main benefit of IBM is that it is able to remove even the hardest materials, leaving a flat, clean surface.[120] Hence, the previous abrasively polished cross section was milled using static flat milling at an offset of 88°, with a power of 6 kV for 1 hour in an inert argon
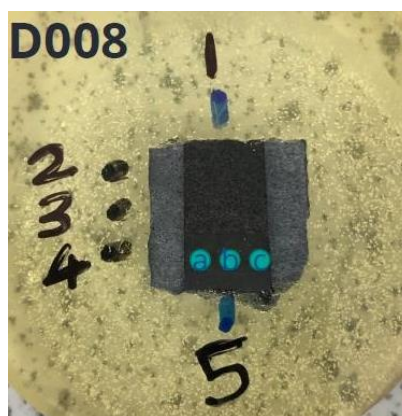
Figure 29: An image of the resin embedded PCD-a sample following abrasive polishing, with the analysed sections marked out. The dimensions of the scanned sections were 50 μm × 35 μm (l × w), giving an area of 1750 μm².

atmosphere. The newly milled surface was then split into sections to allow for a more in-depth analysis. A photograph of the prepared sample is shown in Figure 29.

SEM images of the new surface indicated an improvement in the quality of image produced, as shown in Figure 30. IBM was determined to be an effective method of revealing the presence of smaller diamond particles within the sample, and by extension, improving the composition data to more closely reflect those of the expected values (Table 1).

Areas 2 and 3 exhibited peaks in the Raman spectra at 1332 cm⁻¹ and 1558 cm⁻¹, whilst also showing a much lower diamond:graphite peak area ratio than areas 4 and 5 (Figure 29). This was also in-keeping with SEM analysis of the same area, that indicated a greater intensity of smaller sized diamond. Raman analysis of sections 4 and 5 also displayed peaks at lower wavenumbers (~ 500 cm⁻¹), which is likely attributable to the presence of cobalt oxides.[121]

Figure 30: SEM images produced using BSE's from (a) region 1 and (b) region 5 of the polished PCD-a sample following IBM.

Table 1: The elemental composition in wt.%, as determined by EDX for PCD-a regions 1, 2, 4, and 5, following surface treatment with IBM. Note that residual argon levels are due to the inert atmosphere used during the IBM process.[118]
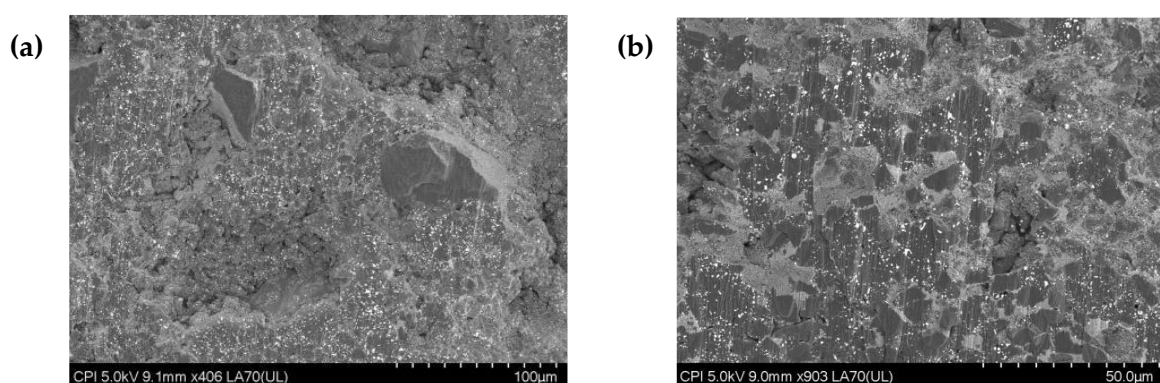
Element	Region 1	Region 2	Region 4	Region 5
Carbon	81.67	82.75	84.82	83.40
Cobalt	16.74	15.63	13.09	14.69
Aluminium	0	0	2.04	1.91
Argon	0.05	0.05	0.05	0

It is also noted that aluminium was observed in the lower sections of PCD-a. A possible source of this contaminant could be the pyrophyllite material used to construct the reaction vessel, which would further indicate that some form of chemical interaction is taking place between the reaction chamber and its contents. Alongside the presence of aluminium, there was also a decrease in the levels of cobalt present in these areas. As cobalt was found to have diffused throughout the reaction chamber (see Section 4.1.2), it is possible that diffusion of cobalt between the reaction mixture and the pyrophyllite chamber could also have occurred.

Whilst IBM was successful in improving the acquisition of the compositional data above, voiding remained present in the samples, and thus still posed an issue. As the PCD-a sample was initially polished using abrasive action with silicon carbide, the voids produced by the tearing of diamond grains from the matrix were too large to be smoothed over via the use of IBM. Hence, another technique of removing the rough, unpolished outer surface is needed. As such, a revised method of initially laser cutting the sample, followed by IBM was conceived. Owing to the issues presented by the formation of metal oxides, the experiment was repeated, this time including an extra hold period at 1000 °C for 35 minutes. This was to try and remove any oxygen that had potentially adhered to the powder surfaces, and thus prevent the formation of the oxide species detected previously.

CPI 10.0kV 7.5mm x612 PDBSE(CP)　　　　　　　　50.0µm
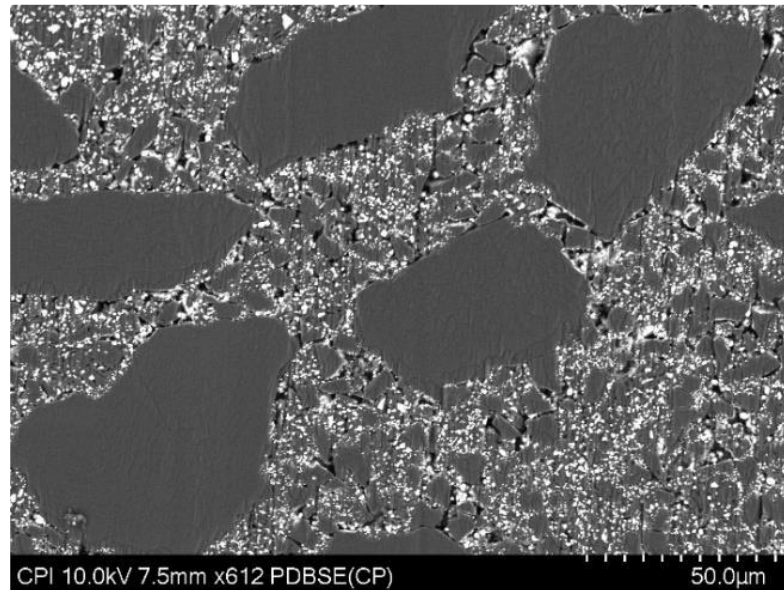
Figure 31: BSE SEM image of the PCD-b surface following processing via laser cutting and IBM showing a greater definition of diamond particles. Note the difference in magnification of this image relative to similar imagers presented within this chapter.

The PCD sample produced, PCD-b, was then laser cut and subjected to IBM treatment. SEM images revealed that this produced a much better surface, and that the smaller diamond grains that were previously unable to be imaged were clearly visible (Figure 31). One disadvantage of the IBM process is that displaced material can become deposited further down the sample as it travels away from the beam. This is seen on the SEM images as white striations that run across the image, obscuring the diamond grain dimensions, with this being particularly prominent for those of smaller sizes. As previous BSE images demonstrated, the heavier cobalt particles appear as bright white regions, with carbon-based areas appearing much darker. Hence, based on this, the chemical make-up of these striations must be cobalt. Compositional data obtained using EDX confirmed this, as the proportion of cobalt ranged from 11 wt.% up to 20 wt.%,

Figure 32: SEM-EDS images of lower, central and upper (left to right) regions of the PCD-b sample, showing an increase in visible dust and cobalt content across the sample. Here, blue represent carbon, with cobalt being represent by red. From left to right, the composition of cobalt is 11, 15 and 20 %wt.[120]

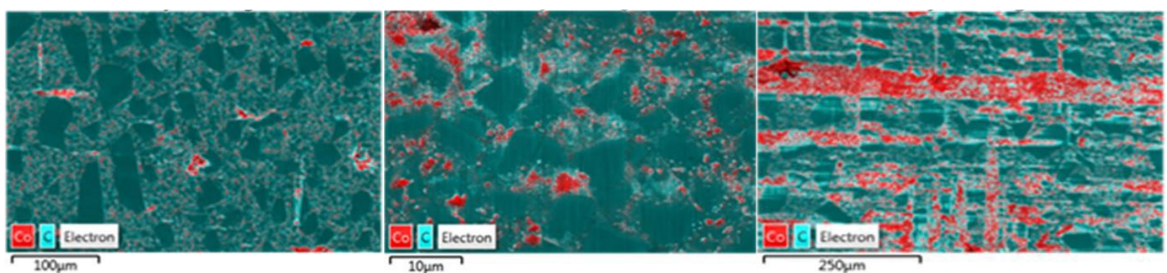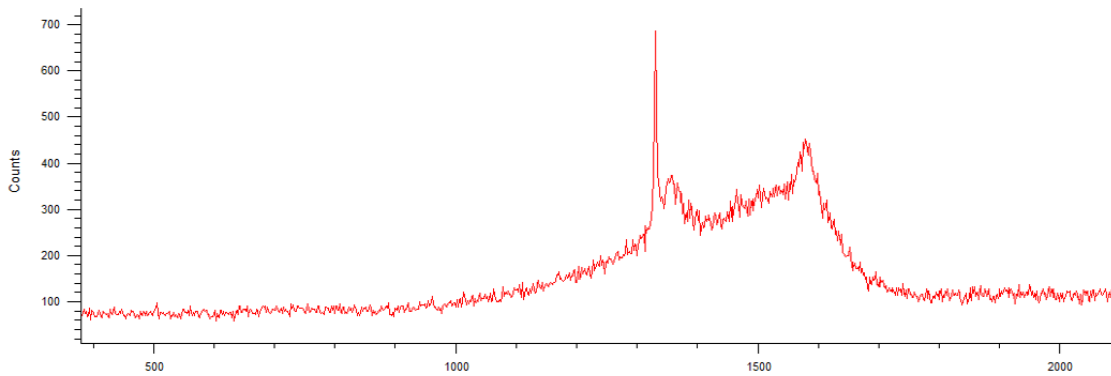*Figure 33: A Raman spectrum obtained for the PCD-b sample following laser cutting and IBM.*

indicating a gradual increase as images further away from the IBM beam source were sampled (Figure 32).

As with the previous PCD-a sample, the PCD-b sample was divided into regions and analysed using Raman spectroscopy, with the aim of ascertaining the exact nature of the carbon-based regions present (Figure 33). Whilst not all of the peaks present were able to be allocated to a specific species, Raman mapping scans taken across the sample showed overlapping peaks of diamond and amorphous carbon. In turn, this made defining peak areas incredibly difficult, and hindered this method of analysis. Despite this, it was noted that, alongside the diamond peaks, there was also a significant signal centred around 1580 cm^{-1}, which is associated with the presence of graphitic carbon. When considering that only diamond-based carbon was placed into the reaction chamber, the occurrence of graphitic carbon following exposure to the high temperature reaction conditions indicates that some level of graphitisation of the diamond grains is occurring. This is contrary to the overall aim of sintering the diamond particles together, and forming diamond-diamond bonds throughout the sample.

To try and shed more light on the presence of graphitic carbon within the sample, more detailed and rigorous Raman analysis was undertaken. Using MATLAB, the Raman data acquired was extracted and processed against reference points within the map that the data was originally collected from.[118] This produced topological heat maps for both diamond and graphitic carbon across the surface (Figure 34). Using these maps, it was determined that diamond was highly localised, and generally didn't appear much across the map, whilst graphitic carbon was readily observed. This is contrary to the

SEM data shown in Figure 31, which displayed a clear abundance of both large and small diamond grains.

One possibility for these conflicting results could be the surface topography of the sample, as a confocal microscope was used. This would only allow light that is in the focal plane to be observed, and would therefore struggle to detect the smaller diamond grains if the sample surface was of a certain roughness. However, despite these issues, it can still be seen that areas with a high intensity of diamond appear to be adjacent to areas with a high intensity of graphitic carbon, *i.e.*, one domain appears at the edges of another. This would suggest that graphitic carbon is located on the surfaces of the diamond grains, and that the experimental set-up is achieving conditions that can alter the composition of the diamond in the reaction chamber.

Whilst the Raman data was insufficient to analyse both the large and small grains present in PCD-b, due to the high quality of image produced by the laser cut and IBM process used to prepare the sample surface, it was possible to analyse the particle size. As the ultimate aim of the sintering of diamond particles is to produce PCD composites with a network of diamond-diamond bonds, it stands to reason that an increase in the size of the diamond grains present should be seen when compared to their starting size. In order to make this comparison, the average particle size of the diamond grains in the
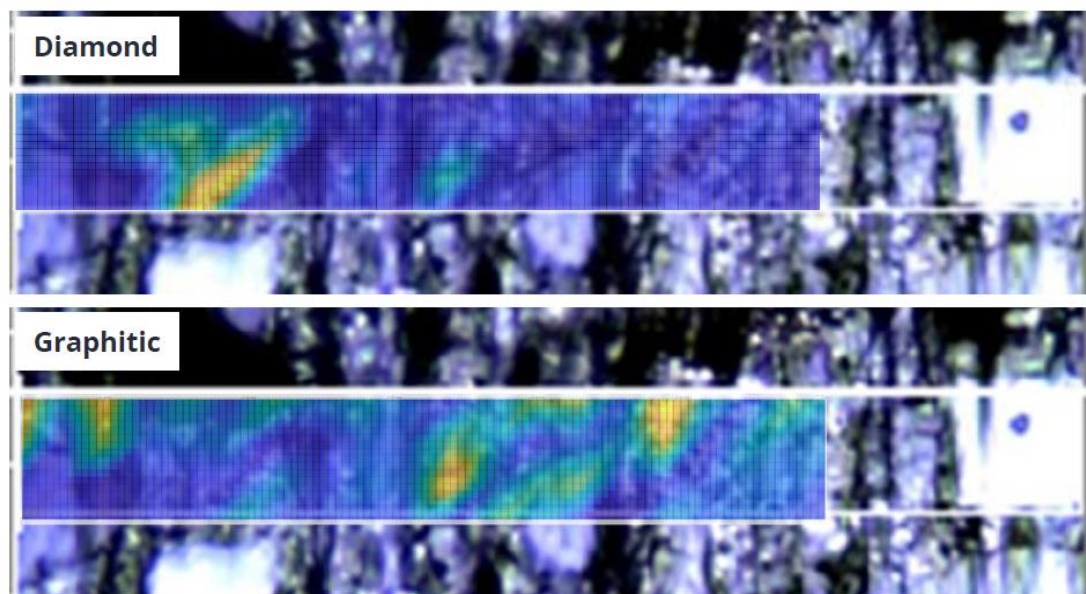

Figure 34: A Raman map taken from a central region of the PCD-b sample. The top shows the diamond peak intensities, with the bottom showing the peak intensities of graphitic carbon. Yellow indicates more intense peaks.[118]
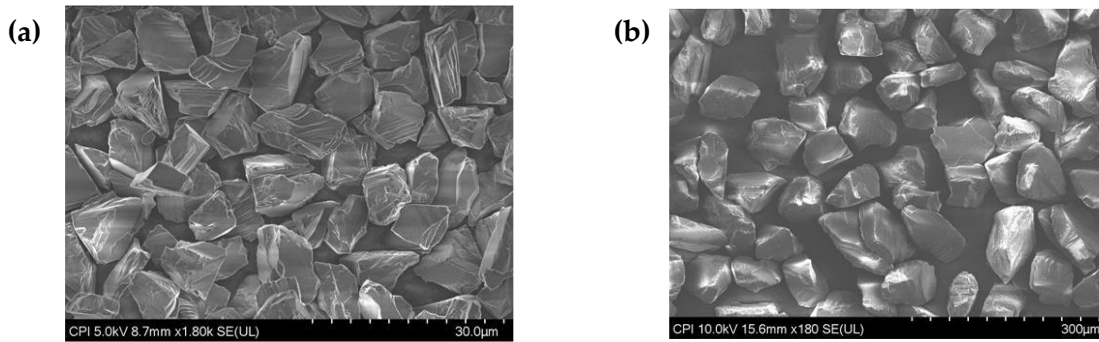
Figure 35: The SEM images used to analyse the particle size of (a) the 8 – 12 μm powder and (b) the 270 μm powder.

two starting materials were analysed via SEM, with the purpose of verifying their starting size (Figure 35). Manual measurement of the grains was undertaken and used to determine a size distribution. For the 8 – 12 μm diamond powder, the mean and median particle size was determined to be 9.2 μm and 9.3 μm, respectively. With respect to the larger 230 – 270 μm powder, the observed particle size varied considerably from that stated by the manufacturer, with a mean value of 93 μm, and a median value of 88.3 μm. It was further noted that the larger powder grains exhibited an irregular shape, alongside a wide range of aspect ratios.

When determining the particle size of the diamond grains in the PCD-b sample, two methods were used, manual sizing similar to that done for the starting powders, as well as sizing performed by an image analysis software known as ImageJ (Figure 36). Utilising the technique known as 'pixel classification', it is possible to obtain better analysis of the smaller particle sizes in a sample, as well as collect a much larger data set. By comparing the results of the two methods, the validity of the results produced by the software can be checked and validated.

The total count for the manually determined distribution was 139, however only 32 of the large diamond grains could be accurately measured. The optimised ImageJ process was applied to a range of images. Ultimately, data was collected for 6828 small diamond structures, and 71 large diamond grains. Data for each of the 5 regions of the PCD-b sample determined that a reduction in the small diamond particle size from the initial 9.2 μm towards 2 μm had occurred, with a similar size reduction also being observed for the larger grain size of diamond, decreasing from 93 μm to around 40 μm.
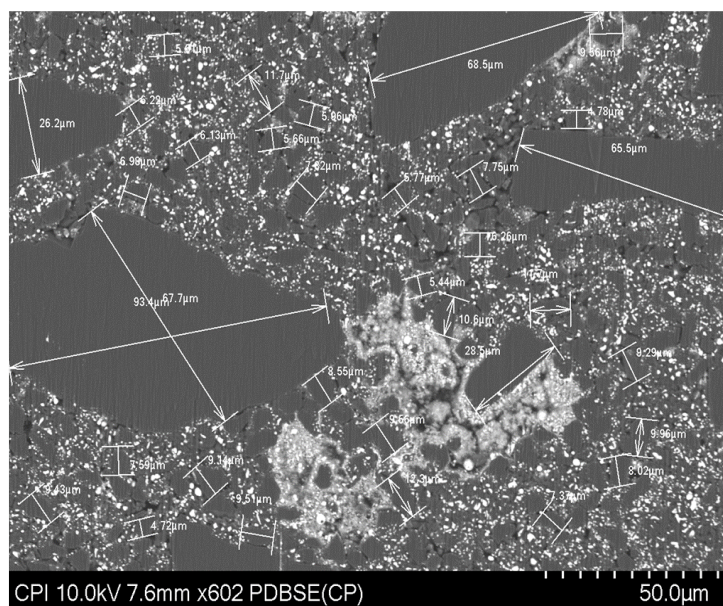
Figure 36: Examples of the particle sizes determined by the ImageJ software.

Taking this size reduction in conjunction with the confirmed presence of graphite throughout the sample, it appears that the current apparatus set-up is not achieving the high pressures required for diamond growth, thus allowing graphitisation to occur. Whilst analysis of the PCD materials produced indicate that pressures are too low, the data is insufficient to give any information about the actual pressures achieved. As such, further analysis of the pyrophyllite reaction chambers was undertaken.

4.1.2 Analysis of Pyrophyllite Reaction Chamber

In order to ascertain a more precise temperature-pressure range achieved by the apparatus during the synthesis of the PCD samples, analysis of the compositional changes of the pyrophyllite reaction chamber material was undertaken. As a material, pyrophyllite is generally well studied and understood, as are the phase changes that occur when it is subjected to the HTHP conditions present in our experiment. Two well documented analysis techniques of the pyrophyllite structure and its degradation products are PXRD and IR spectroscopy. The pyrophyllite structure can be described as a hydrated, aluminous, phyllosilicate mineral whose ideal chemical formula is $Al_2Si_4O_{10}(OH)_2$, and has an octahedral layered structure based on an octahedral sheet of Al^{3+} ions layered between two tetrahedral silicate sheets.[122] It is closely related to talc, in both structure and appearance, and shares many of its properties, including hardness, and, because of this, it has found use in many similar applications.[123,124]

When used as a reaction vessel, several phase changes occur as external temperatures and pressures increase.[124–126] Initially, a dehydroxylated phase forms, which further decomposes into a binary aluminosilicate and silica phases, according to the simplified chemical equation;

$$Pyrophyllite \rightarrow Aluminosilicate + Silica + Water \qquad (4.1)$$

$$3\,Al_2Si_4O_{10}(OH)_2 \rightarrow 3\,Al_2O_3.SiO_2 + 9\,SiO_2 + 3\,H_2O \ . \qquad (4.2)$$
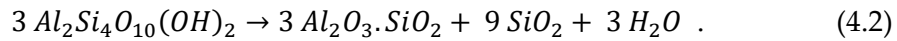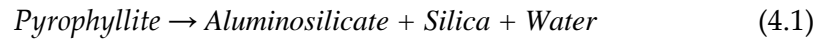
The structure of the aluminosilicate and silica phases can vary depending on the exact temperatures and pressures the pyrophyllite was subjected too. Studies investigating the HTHP decomposition of pyrophyllite have shown that the SiO_2 phase produced can be one of three polymorphs, amorphous silica, coesite and stishovite.[124] Amorphous silica (AS) is the lowest pressure polymorph, with coesite only being known to form when pressures are above 2.5 GPa. Stishovite is reported to form at pressures > 8 GPa.[127,128] Whilst AS is stable at atmospheric pressures, both coesite and stishovite are not, and both will degrade into cristobalite (CR) when pressures are below 2.5 GPa. Moreover, this transformation is known to be appreciable even at temperatures as low as 400 °C.[128] Due to the way in which the apparatus generates pressure by exploiting thermal expansion, this means that pressure can't be maintained as the apparatus cools, and will subsequently drop as a function of the decreasing temperature. As such, any coesite or stishovite formed is likely to degrade into CR as the apparatus cools, with this only being possible if the pyrophyllite chamber had previously been subjected to pressures of greater than 2.5 GPa.[124,127] Hence, it is possible to use the presence of a CR phase as a marker for the *in-situ* pressures achieved during the experiment.

For the temperature and pressure range expected in the experiment, $Al_2O_3.SiO_2$ can also be present as one of three structures; sillimanite, andalusite, or kyanite.[124] Of these three phases, kyanite is the most stable at high temperatures and pressures, whilst andalusite is the most stable at lower temperatures and pressures. Sillimanite is the most stable structure at high temperature and low pressure.[129] However, whilst these phases might be present under the HTHP conditions such as those found in the experiment, none of them are known to exhibit metastability, and will degrade into mullite (MU),

another known aluminosilicate, when outside of these conditions, according to the equation;[130]

$$3\ Al_2O_3.SiO_2\ \rightarrow 3(Al_2O_3).2(SiO_2) + SiO_2\ . \qquad\qquad (4.3)$$
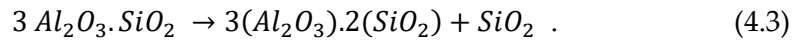
Mullite is the only $Al_2O_3.SiO_2$ system that is stable at atmospheric pressure, and its formation as a degradation product is associated with the formation of another silica phase, which can be either AS or CR.[125] The exact structure of this new silica phase is again dictated by the exact temperature and pressure conditions present during its formation, with CR generally being associated with temperatures above 1150 °C.[126,131] Below this, the formed silica phase will be amorphous in nature. Unlike the various silica polymorphs discussed above, these polymorphs of $Al_2O_3.SiO_2$ are stable at pressures on the order of 100's of MPa, and will therefore be stable at lower temperatures when the apparatus is in use. As such, when the degradation of these phases occurs, the temperature will be below the 1150 °C required for the formation of CR, and, consequently, will only produce AS.[131] Due to this lower pressure degradation of the aluminosilicate phase formed into MU, alongside the temperature dependence of the associated silica phase, it is not possible to use this phase change as a marker of the pressures achieved during the experiment.

Initially, a sample of unused pyrophyllite (RC-u) was ground into a powder, and an IR spectrum and PXRD pattern were obtained in order to ascertain the presence of any potential impurities (Figure 37(a) and (b)). The PXRD data obtained was compared to a calculated model of pyrophyllite obtained from Rayner *et al.* (Figure 37(a)).[132] Visually, good agreement is observed between the calculated model and the PXRD data obtained, which suggests that pyrophyllite is present, as expected.

This data is also in agreement with that obtained via IR spectroscopy (Figure 37(b)), which shows a characteristic OH stretching at 3675 cm^{-1} that can be assigned to the Al$_2$OH stretching mode, alongside intense peaks below 1150 cm^{-1} that are in agreement with data reported throughout the literature.[126] Hence, based on this data, the material used to construct the reaction chamber in our apparatus is believed to be composed of high quality pyrophyllite, with what appears to be little to no impurities present.

(a)
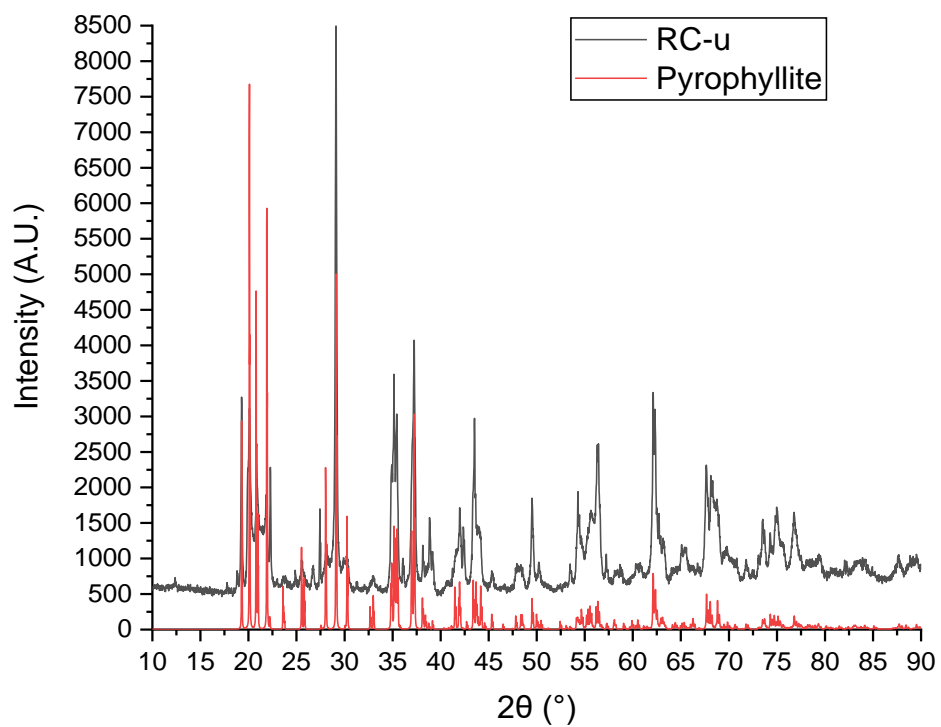
(b)
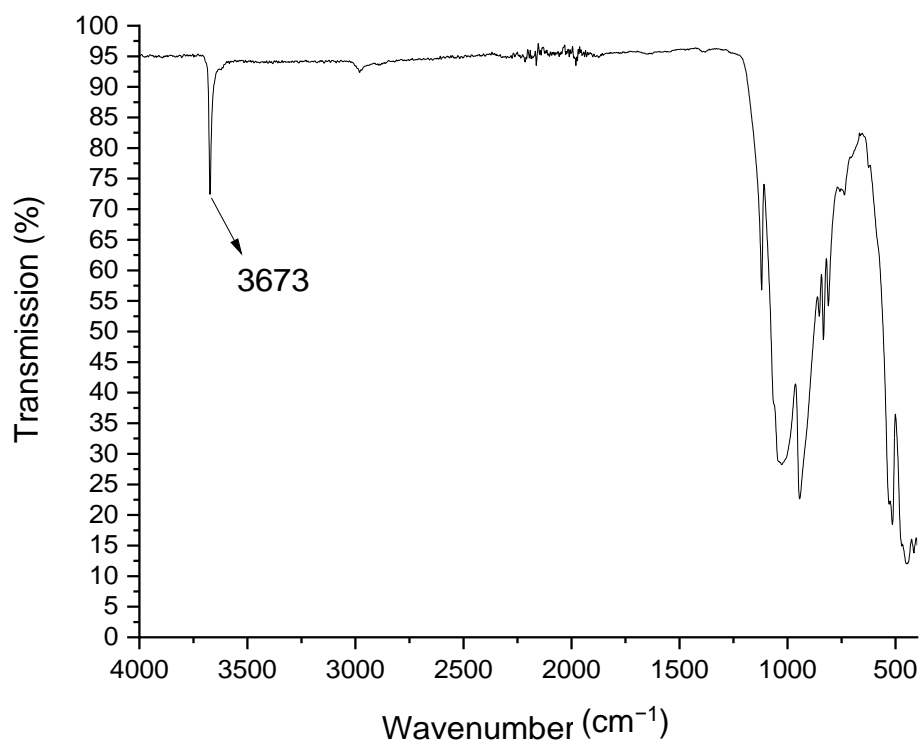
Figure 37: The (a) PXRD pattern obtained for RC-u compared to the calculated pattern for pyrophyllite,[132] and the (b) IR spectrum of RC-u.

Following the initial synthesis of the PCD sample using the new apparatus, a sample of the used pyrophyllite reaction chamber used to synthesise PCD-a, RC-a, was analysed using the same techniques described above, and compared to the data shown in Figure 37. Significant differences were observed in the PXRD and IR data when compared to the unused sample. The data suggests that there is a significant change in the composition of the sample.

The IR spectrum obtained for RC-a (Figure 38) exhibits distinct changes in the functional groups present, with the characteristic hydroxyl peak at 3673 cm^{-1} no longer present. As this signal was characteristic of pyrophyllite, its disappearance indicates the sample has fully dehydroxylated, and by extension, that a phase change has occurred. According to literature analysis performed by Wang *et al.*,[126] during the dihydroxylation stage, the hydroxyl peak first splits into two at similar wavenumbers. These two peaks then fully disappear for samples subjected to 900 °C for over 15 minutes, indicating a phase change from pyrophyllite into MU and its associated silica phase. Regarding the nature of the aluminosilicate and silica phases present in the used samples, the IR spectra obtained was able to provide some key structural insights (Table 2).

Table 2: Tabulated IR values obtained from the RC-a pyrophyllite sample used in the synthesis of PCD-a compared against literature values of pyrophyllite samples subjected to similar temperatures and pressures.[126]

Sample (cm^{-1})	Amorphous Silica and Mullite (cm^{-1})	Cristobalite and Mullite (cm^{-1})
458 – 408	467	381
549	526	445
722	732	476
817	823	519
956	901	574
1077	1110	617
1277	1248	736
		794
		884
		1091
		1168
		1201

Figure 38: The IR spectrum obtained for the pyrophyllite used in RC-a (red) compared to that obtained from RC-u, an unused pyrophyllite sample (black).

Comparing the IR peaks between both our sample, as well as that analysed in the literature, the presence of cristobalite within the sample is unlikely, despite being within the temperature for its formation. This is most likely due to the short hold time (10 minutes) at 1540 °C, compared to the 5 days reported in the literature.[126] Based both on the number and position of the peaks present, it is more than likely that a combination of both MU and AS are present, as the tabulated IR values are in general agreement to within a few wavenumbers of those reported in the literature. Furthermore, two unassigned peaks appear in the region that usually corresponds to CH_2 deformations (3000 – 2850 cm⁻¹), with these not belonging to either the pyrophyllite or silica phases. It is possible that these could correspond to an oxide species, as the IR spectra obtained from the RC-b sample that was subjected to an off-gassing step when used in the synthesis of PCD-b, lacked these peaks (Figure 39). Moreover, CO_2 that has been absorbed into the pyrophyllite structure has been shown to exhibit IR peaks as high as
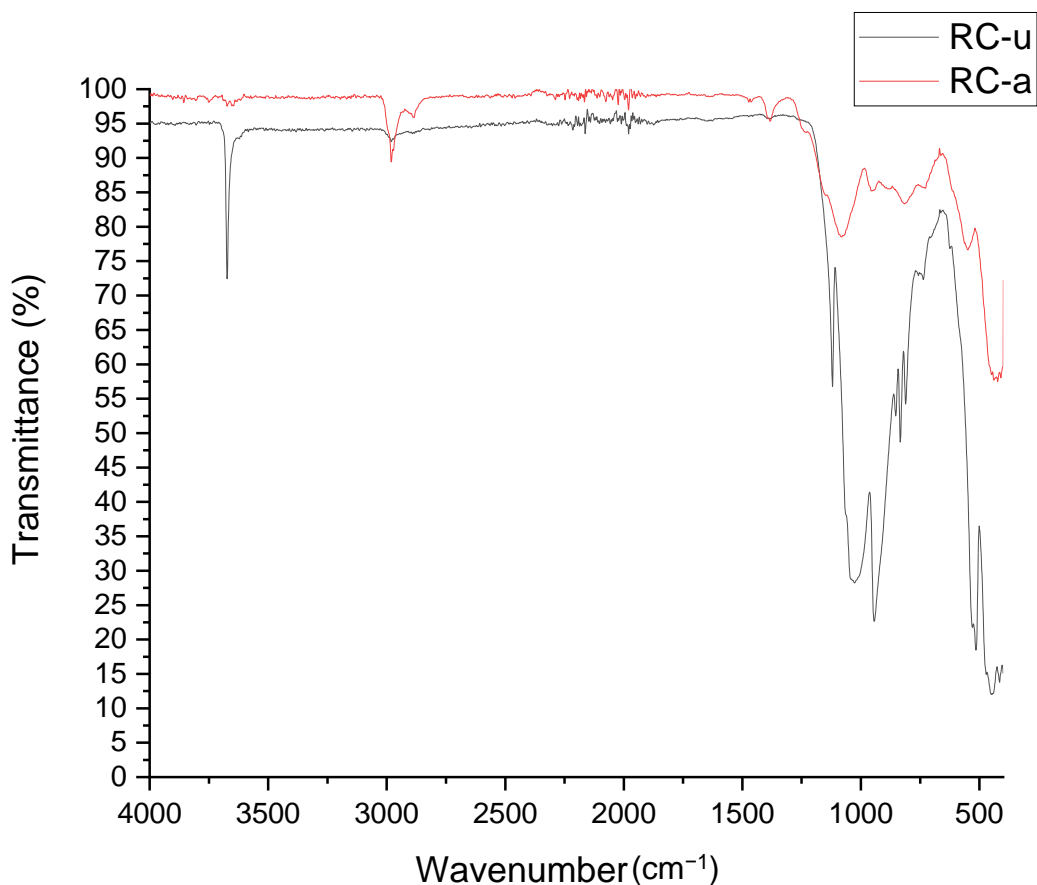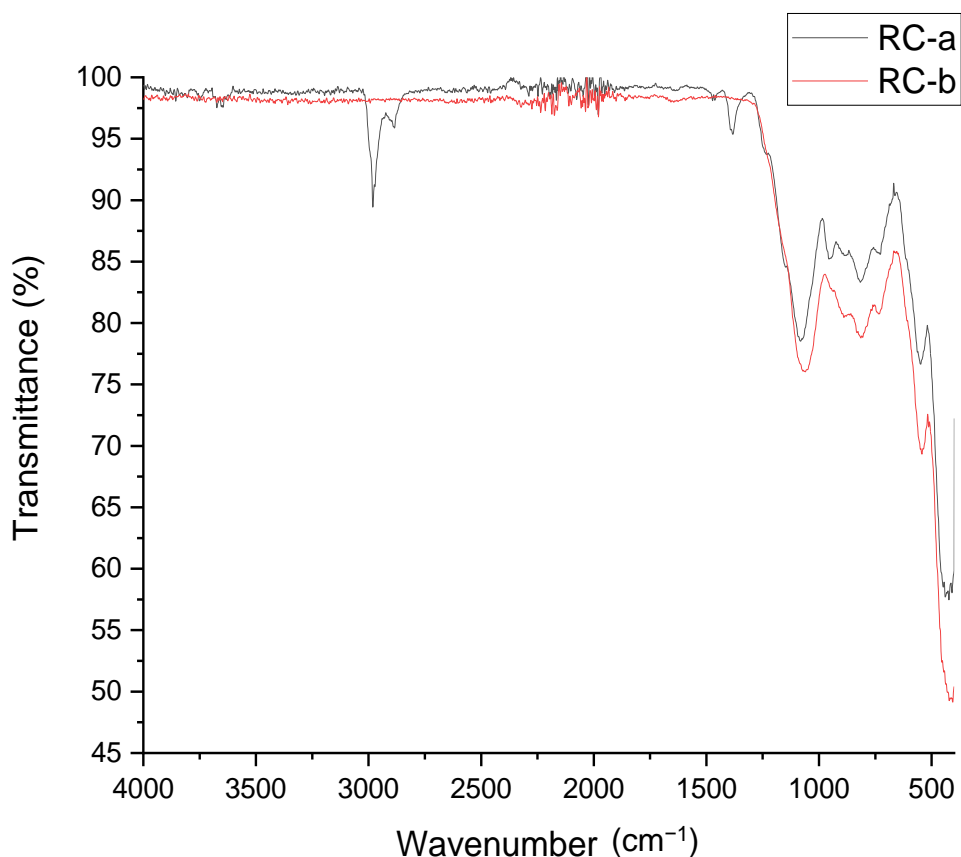
Figure 39: The IR spectrum obtained from the pyrophyllite sample RC-a (black) compared to that obtained from RC-b, a pyrophyllite sample that underwent an added off-gassing step (red), showing the disappearance of the unknown peak at ~2900 cm⁻¹.

2500 cm⁻¹.[133] However, it is noted that these would be outside the range of those in our data.

Alternatively, based on PXRD analysis (Figure 40), it was found that metal diffusion of the Co catalyst into the surrounding chamber had occurred, producing a Co-doped mullite species (Co-MU), alongside a corundum (α-Al_2O_3) by-product.[134] However, at present, it is difficult to confirm the precise cause of these unknown vibrations.

Overall, the PXRD pattern obtained for RC-a was in good agreement with the IR spectrum, and indicated that, alongside the MU-based species, AS is also present in the sample (Figure 40). The presence of AS is evident by the characteristic broad background centred around 22°, occurring between $2\theta = 10 - 35°$.[135] The exact nature of the MU phase is difficult to differentiate via solely PXRD, as both MU and Co-MU possess incredibly similar diffraction patterns that differ only in the intensity of certain reflections, with

Figure 40: The PXRD pattern obtained from RC-a (black), alongside the calculated patterns for Co-MU[134] (red) and corundum (α-Al_2O_3)[136] (blue).

both the number and position of reflections being very similar.[134] However, it is noted that the calculated PXRD pattern for MU was unable to account for all of the observed reflections. For example, the peak at $2\theta = 43.15°$, which was only able to be explained by the presence of corundum within the sample.[136] As this happens to be a by-product of the Co doping of MU, the presence of this extra phase provides further evidence that a Co-MU phase has formed to some extent.[134] It is noted that the overall intensity of the peaks attributable to corundum is much lower than that observed for the MU reflections, and is therefore likely to be present in lower quantities. As such, it is likely that both MU and Co-MU phases are present in the sample, as not all of the MU formed could have been sufficiently doped. To confirm whether this is the case, higher resolution diffraction data would be needed that would enable detailed Rietveld analysis to be undertaken.

In addition to the IR data, a PXRD pattern was also obtained for RC-b (Figure 41). The similarity of the peaks present in the IR spectra of RC-b and RC-a, indicated that MU and AS phases were also present in this case (Figure 39). This was confirmed via analysis of the PXRD data obtained. Whilst it was noted in the IR spectrum that there were some structural differences due to the disappearance of unknown peaks at ~2900

cm⁻¹, there was no discernible difference in the phase composition when comparing the PXRD patterns of the two samples.

Overall, the results obtained from analysis of the pyrophyllite material used to make the reaction chambers RC-a and RC-b are in-keeping with those relating to the PCD-a and PCD-b samples produced, and are consistent with a loss of pressure during the experiment. A lack of cristobalite present indicates that, whilst temperatures were high enough for it to from, the pressure could not have exceeded 2.5 GPa when at the synthesis temperature of 1540 °C.

Following the realisation that some form of pressure loss was occurring within the apparatus during synthesis, possible reasons were explored as to what could be causing this. One avenue explored was the composition of the Co cemented WC anvils. It was noted that the 1540 °C used during the experiment was in excess of the generally accepted melting point of cobalt at 1495 °C.[119] Hence, whilst at this temperature, the cobalt binding material present in the anvil will begin to liquify, weaking the integrity of the anvil, and allowing for deformation to occur. As such, it was decided to change
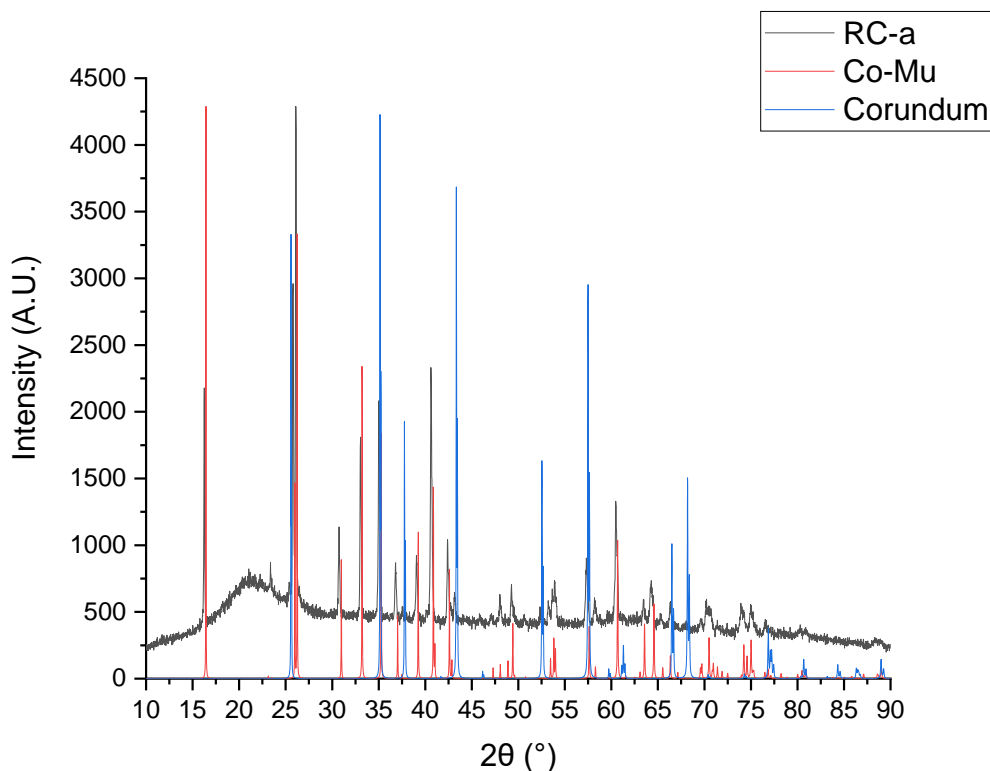

Figure 41: The PXRD pattern obtained for RC-b (black), alongside the calculated patterns for Co-MU[134] (red) and corundum[136] (blue).

the material used for the anvils to that of one which possessed a higher melting point. One such candidate was pure tungsten, which exhibits the highest melting point of any metal at 3422 °C.[137]

In order to ascertain if this made a difference, a new experiment following the same method as previously outlined was conducted using the new tungsten-based anvils. The pyrophyllite reaction chamber was again ground into a powder, and a PXRD pattern obtained, which is shown in Figure 42. It was immediately noted that the number of reflections had increased, indicating the presence of multiple phases within the sample. Whilst there was still the raised and noisy baseline characteristic of AS, it was noted that there was a large peak present at 22°, where previously there had been none. Based on the literature, this was determined to be indicative of a CR phase. As outlined previously, the slight presence of AS in the sample is most likely due to the degradation of higher-pressure polymorphs of $Al_2O_3.SiO_2$ when forming mullite.[130] However, the presence of CR can only be accounted for by the degradation of high-pressure polymorphs of SiO_2, such as coesite or stishovite. Moreover, these could only have
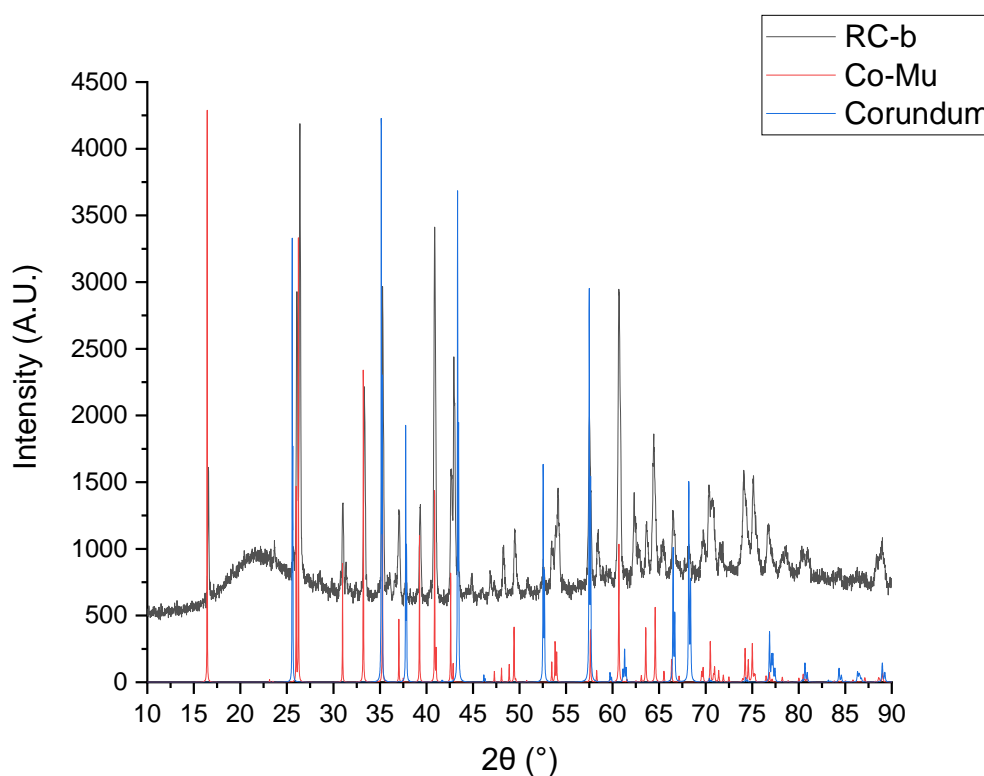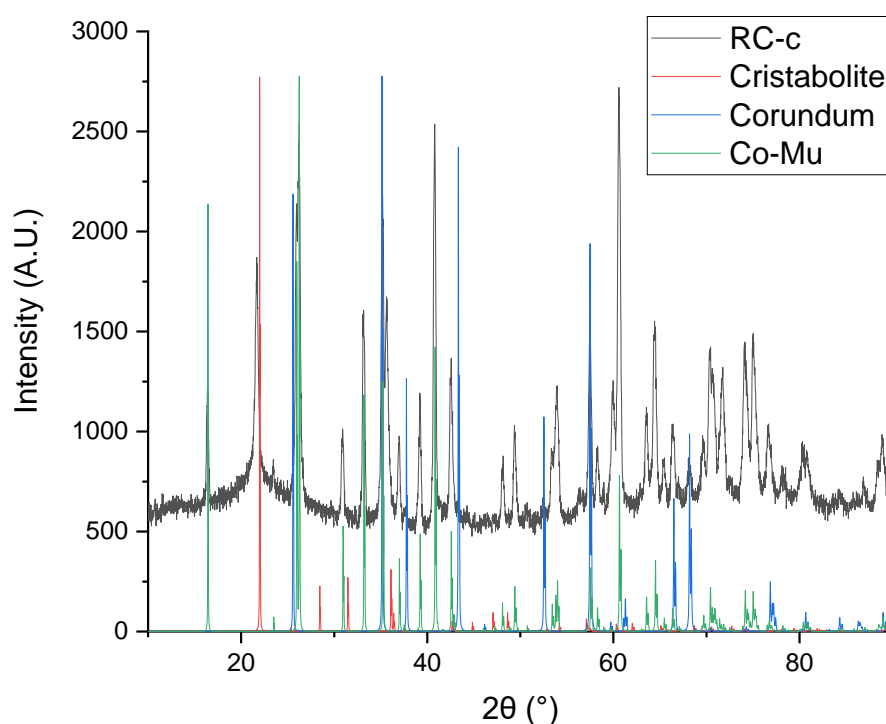

Figure 42: The PXRD pattern obtained for RC-c (black), alongside the calculated patterns for CR[154] (red), corundum[136] (blue), and Co-MU[134] (green).

formed if the pressures achieved during the synthesis stage were in excess of 2.5 GPa,[127] and its presence here suggests that the revised tungsten-based anvils are capable of achieving higher pressures than the previous Co-WC-based apparatus.

Similar to previous analysis of the RC-a and RC-b samples, the other phases were determined to be MU and Co-MU, as well as corundum. These are most likely formed in the same way as before, and all phases relate to the formation of MU following the degradation of higher-pressure aluminosilicates. Interestingly, there were still several peaks that were unable to be accounted for by CR, MU and corundum, such as those at $2\theta = 59°$ and $65°$. Following further investigation into the potential phases present, it was determined that another, less commonly synthesised by-product of the cobalt inclusion in MU is a cobalt oxide doped Al_2O_3 ($CoAl_2O_4$).[134] Comparison of the PXRD pattern of RC-c and the calculated peaks for this phase indicated a good match, although some of the peak positions are off by fractions of a degree. This could be due to several factors, including the relatively small amount of literature data regarding this phase.
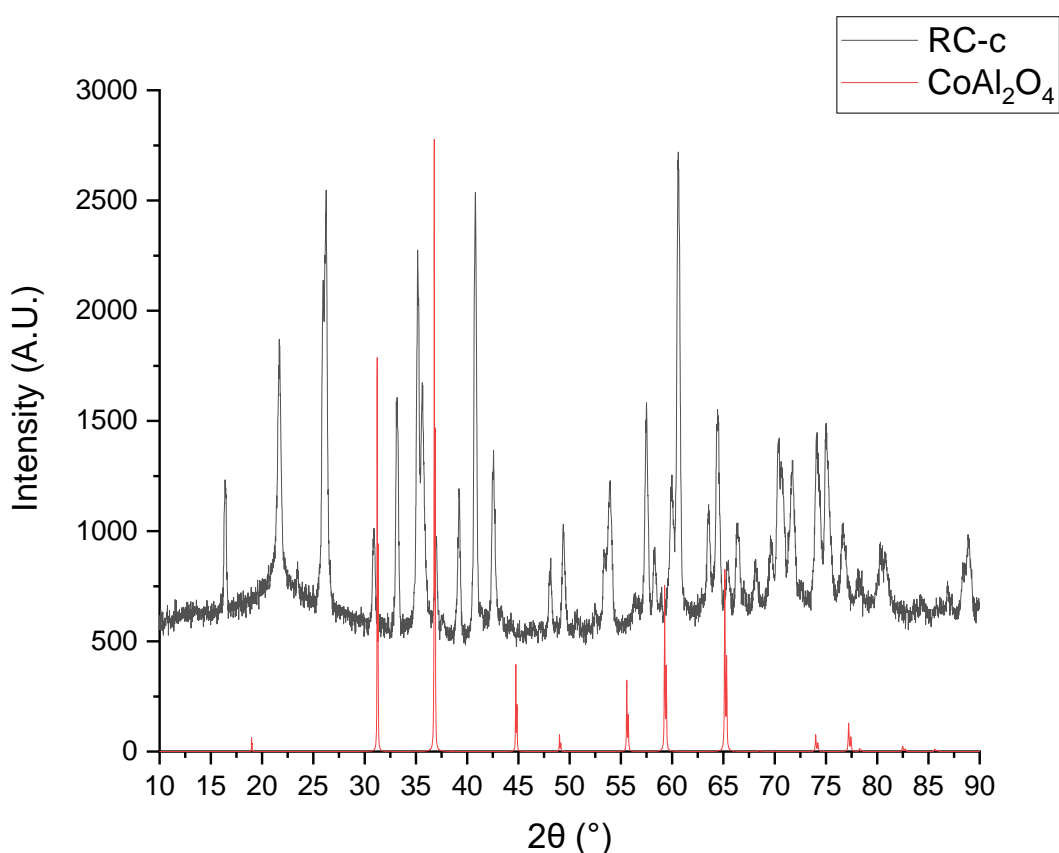
Figure 43: A comparison of the PXRD pattern observed for RC-c (black) and the calculated pattern for CoAl₂O₄.[134]

Alternatively, lattice deformations that occur when materials are subjected to high pressures can also cause the peak positions to shift to lower 2θ values, which was also observed for selected reflections in other phases.

Essentially, this indicates that the main difference between the composition of RC-c, and the composition of RC-a and RC-b is the presence of CR. Hence, the change to tungsten-based anvils appears to be preventing the pressure loss that occurred previously, although more comprehensive data relating to the composition of the PCD composite produced by RC-c is needed to confirm this. In order to shed more light on this possibility, further work to analyse the IR spectrum of RC-c, as well as the SEM and Raman data of PCD-c sample formed during this experiment, would be required.

4.2 BINDER SYNTHESIS

Alongside the material used to create the central anvils, another area of potential improvement identified was the surrounding CFC framework in which the anvils are contained. As outlined in Section 2.2.3, CFC is produced by embedding CF fibres in a surrounding phenolic resin matrix, which is then pyrolised. Phenolic resin was identified as the most suitable matrix material due to its high carbon content, as well as its ease of manufacture via the resole route.

Initially, the synthesis of resole resin was carried out using phenol as the starting reagent, as this route is well understood, and easily performed. Moreover, this would allow for the direct comparison between samples that are synthesised with HMP under the same reaction conditions. NMR and mass spectrometry (MS) were carried out on the isolated product, and indicated the presence of the expected oligomeric species. This was highlighted via ^{1}H NMR, and the resonances observed at δ_{iso} = 3.5 and 4.5 ppm indicated the presence of methyl and ether bonding between phenolic units, respectively. MS analysis indicated peaks at regular intervals ranging from m/z ~200 to 700 Da, demonstrating the presence of oligomeric species of differing chain lengths, and that the correct monomer chain lengths had been achieved.

A potential issue that was identified was the large range of molecular weights exhibited, which extended beyond 1000 Da, although the generally low intensities of

these signals suggest that their presence is minimal. As outlined in Section 2.2.3, chains with a M_w of above 1000 g mol^{-1} begin to demonstrate a large increase in viscosity beyond that which would be suitable for application to CF fibre, and the formation of solid particulate begins to occur.[93,95] Such transformations are detrimental to the intended use of the resole product as a binding material, and hence the presence of these larger chains is unfavourable to the overall process.

Following this initial trial, the process was repeated with both 2-HMP and 4-HMP, using the same ratio of starting reagents, as well as the same reaction length and conditions. This was done to assess whether the HMP isomers produced a product similar to the more widely studied phenol and formaldehyde route. ^{1}H NMR analysis showed the same range of peaks between at δ_{iso} = 3.5 and 4.5 ppm, suggesting that, in both cases, a resole oligomer had formed. MS analysis of both samples also indicated the presence of oligomeric chains, giving similar spectra to that in Figure 44. Lengths of m/z ~200 to 700 Da were dominant, again with some observed lengths being in excess of 1000 Da. Due to this success in producing the same products, additional synthetic experiments were undertaken using only the HMP isomers, with this being due to their much lower toxicity when compared to phenol.[138]
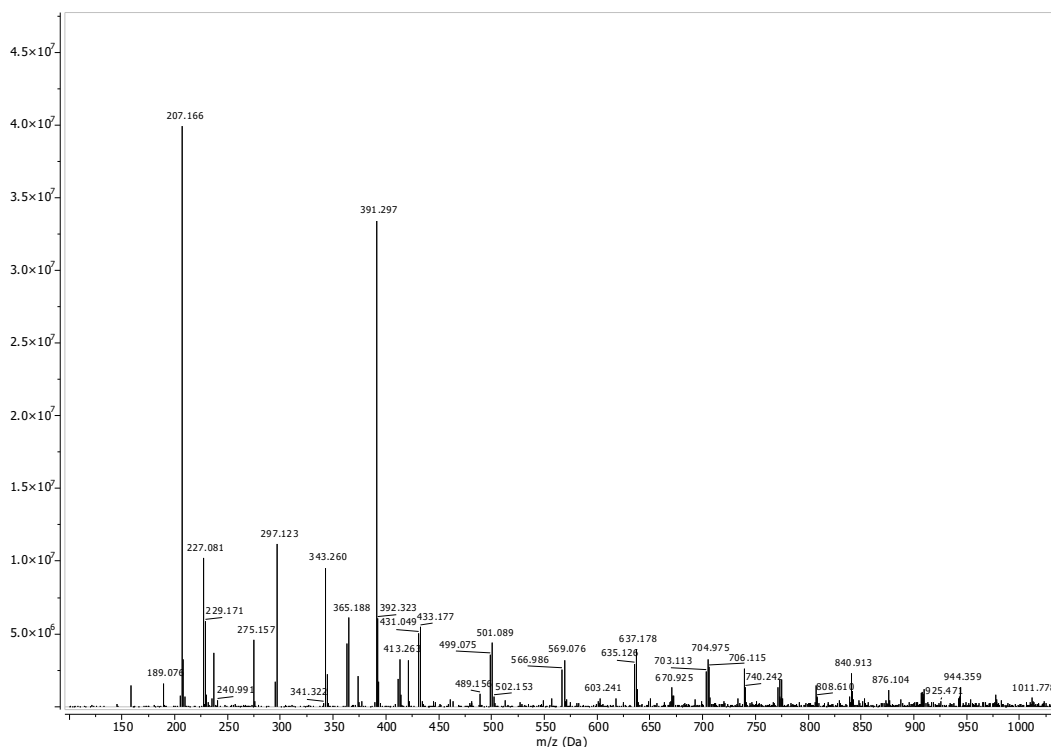
Figure 44: Mass spectrum obtained for a resole oligomer synthesised using phenol.

It is noted that both phenol and HMP starting reagents produced a range of chain lengths that exceeded 1000 Da, which is ultimately of detriment when using the products for the intended role of a pre-resin, primarily impacting the rheological properties that influence the ability of the resin to properly wet the CF strands prior to curing. It is important to note that whilst mass spectrometry can work well for masses below 1000 Da, it tends to be poorly suited for values exceeding this, with GPC normally being used in its place. However, because of the interaction with the solvent and the inter- and intra-molecular hydrogen bonds created, a complete characterisation of the resole resin molecular weight using GPC is extremely difficult. Hence, this technique was not pursued here.[139,140]

4.2.1 Effect of HMP Isomer

Following the confirmation that using HMP as a starting material still produced the resole structure, more comprehensive experimentation into the factors that affect the product produced was undertaken. The swap to using HMP as a starting material poses an issue as most, if not all, of the literature focuses on using phenol as a starting reagent. As discussed in Section 2.3, this is further exacerbated by the fact that the two different mono-substituted isomers have different reactivities, and will therefore behave differently during the early stages of the reaction, and by extension, will impact the final resole products (as outlined in the Introduction). Overall, it was noted that alongside the specific isomer used during the synthesis of the resins, the relative proportion of NaOH and formaldehyde could also be easily altered, as could the reaction temperature. Hence, the effect that these had upon the structure and properties of the produced resole was investigated with the aim of optimising these for our specific purpose.

To be able to compare the specific influence of the HMP isomer against the results obtained in the previous section, the same reaction conditions were employed. Here, different resole oligomers that were synthesised under the same starting ratio of starting materials (2 equiv. of formaldehyde and 0.6 equiv. of NaOH at 90 °C) are discussed.

One shortcoming identified with the analysis methods used in the previous section was the unsuitability of MS when characterising larger oligomers, and as such, alternative forms of analysis were investigated. Due to the different functional groups present, the resole structure lends itself ideally to analysis via IR spectroscopy, with this technique being able to provide a relatively complete structural analysis of the oligomers present. Moreover, as the relative area of the absorbance peaks is known to be proportional to the concentration of the species causing them, using this technique, it is possible to comment on the relative amounts of the species present.[141] IR spectroscopy is an incredibly versatile technique, that is able to be performed on both liquid and solid samples, meaning that highly polymerised samples that contain both liquid and solid fractions can still be analysed. This flexibility further extends to species which possess unfavourable properties in relation to other techniques, such as MS and GPC, meaning the issues outlined previously can also be circumvented. Furthermore, a large amount of structural data can be obtained, including preliminary information on factors such as the extent of polymerisation that would be otherwise difficult to comment on using techniques such as NMR.[139]
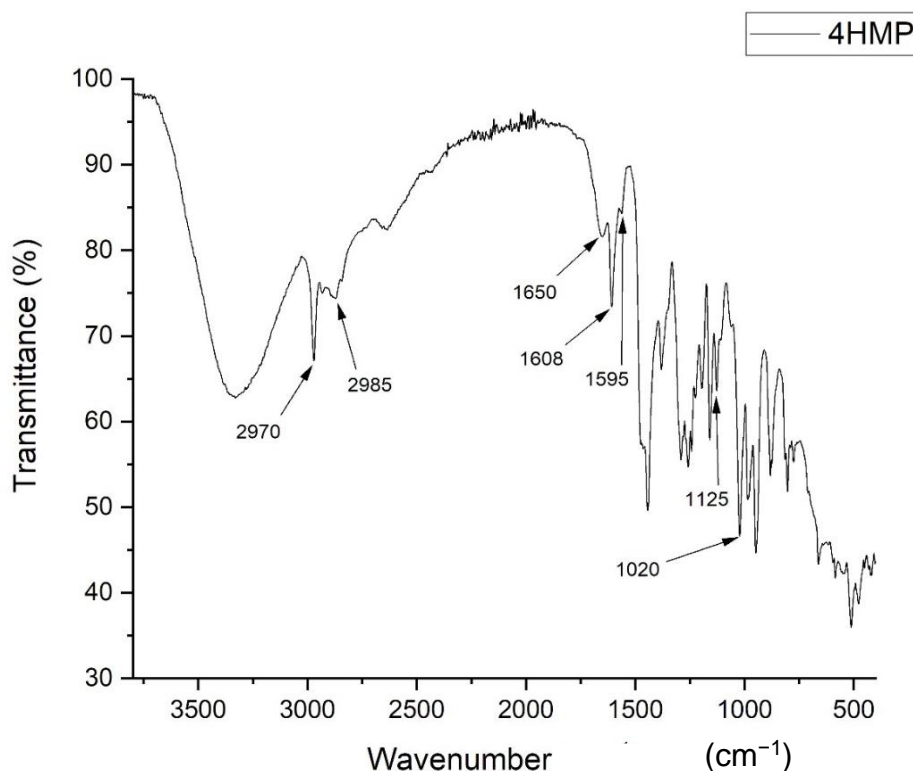
Figure 45: An example IR spectrum taken from resole synthesised using 4-HMP, alongside 2 equiv. of formaldehyde and 0.6 equiv. of NaOH at 90 °C for 30 minutes.

Wavenumber (cm⁻¹)	Vibration	Functional Group
3800 – 3000	$\nu(OH)$, Free	Phenol and hydroxymethyl
2975	$\nu_s(CH_2)$, Symmetrical	Aliphatic methylene
2885	$\nu_a(CH_2)$, Asymmetrical	Aliphatic methylene
1700 – 1650	$\nu(C=O)$	Formaldehyde
1610	$\nu(C=C)$, Aromatic	Aromatic
1595	$\nu(C-C)$, Aromatic	Aromatic
1480, 1460, 1450	$\nu(C=C)$, Aromatic $\nu(C_{Ar}-C-C_{Ar})$, Aromatic methylene bridge	Phenol, Methylene Bridge
1150	$\nu(C-O-C)$	Dimethylene Ether Bridge
1125	$\nu(C-O-C)$	Dimethylene Ether Bridge
1060	$\nu(C-O)$	1° Alcohol
1020, 995	$\nu(C-O)$	1° Alcohol

An example spectrum labelling the peaks detailed in Table 3 is shown in Figure 45. Whilst all of the peaks are of use to varying extents, some bands, such as that between 1500 and 1400 cm⁻¹, exhibit a significant overlap of functional groups, and can therefore make identification of the vibration quite difficult. Furthermore, some of the vibrations that represent the same functional groups are present as shoulders alongside the more dominant peak. Peaks at ~1607 cm⁻¹ correspond to the C=C tension vibration of the aromatic ring, whilst the smaller peak at 1595 cm⁻¹, which is often present as a shoulder (Figure 46), corresponds to the C-C single bond of the same moiety. Depending on the type and level of substitution in the aromatic ring, this accompanying shoulder can appear at varying intensities, with an increase in intensity of the accompanying shoulder being reflective of the level of polymerisation within a resole sample.[139] As such, when resoles have been fully cured into the final solid product, the only aromatic peak observed is that at 1595 cm⁻¹.
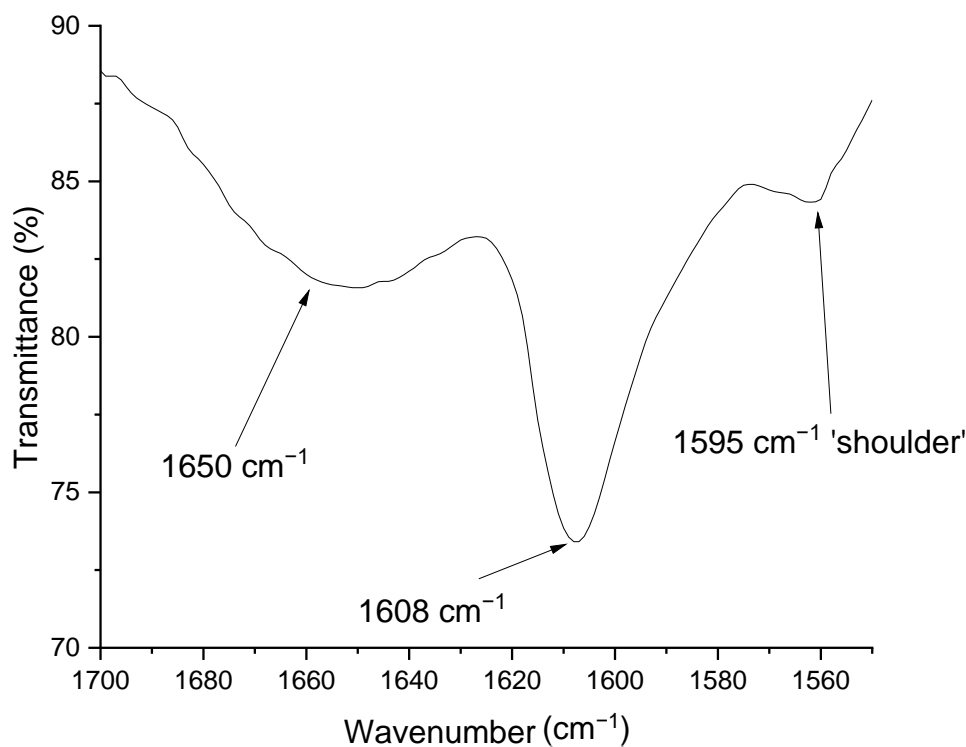
Figure 46: An expanded section of Figure 42, highlighting the aromatic shoulder at 1595 cm⁻¹ in relation to the main aromatic peak at 1608 cm⁻¹, as well as the formaldehyde peak at 1650 cm⁻¹.

Based on this method of analysis for IR spectra, samples of resoles synthesised with both 2-HMP and 4-HMP, as well as a mixture of both isomers were investigated, with a comparison of the corresponding IR spectra being shown Figure 47. Generally speaking, the more the resin preparation protocol favours advancement of condensation, the more distinct the methylene bands become, and the signals from unreacted hydroxyl groups are less pronounced. This can be seen by comparing the relative sizes of the methylene signals when compared to the broad band at $3700 - 3200$ cm⁻¹, which corresponds to free -OH stretches.[142]

As is shown in Figure 47, 4-HMP has the highest relative concentration of methylene bridges. Theoretically speaking, this may be due to lower reactivity of the 4-HMP isomer. Under the standard alkaline reaction conditions, and a formaldehyde to HMP ratio of ≥ 1.5, the formation of the unwanted ether bridge is much more kinetically favoured than the methylene alternative.[105,143] Furthermore, *para-para* linkages are by far the most likely to form carbon bridges, followed by *para-ortho* methylene bonds, with *ortho-ortho* linkages being much more likely to contain the ether moiety.[144] As the 4-isomer is, in theory, less reactive, this means the kinetic advantage of forming ether
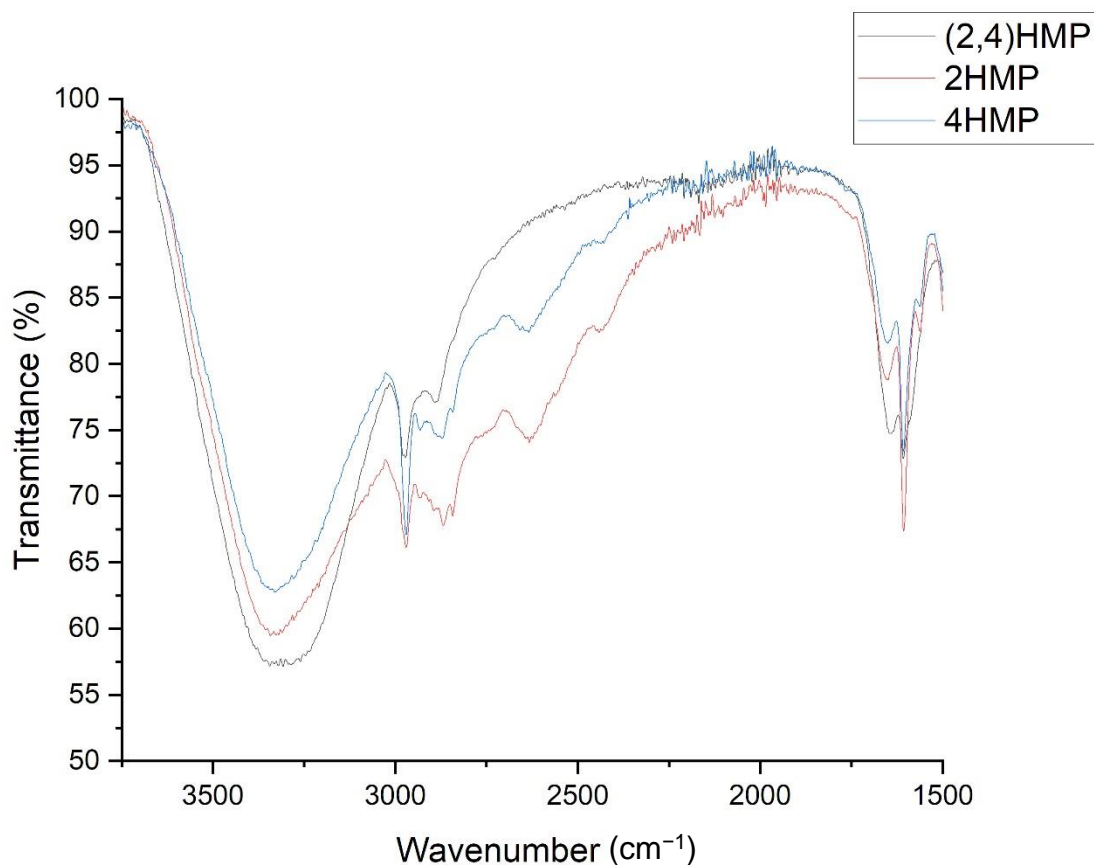
Figure 47: Comparison of IR spectra obtained for resoles synthesised with different HMP isomers (note that (2,4)-HMP indicates a 1:1 mixture of 2-HMP and 4-HMP).

bonds will be much less pronounced. Alongside this, due to already containing a hydroxymethyl moiety in the preferred *para-* position, 4-HMP is essentially set up for the formation of methylene linkages.

Conversely, (2,4)-HMP, which is a 1:1 mixture of the two isomers, has the most intense -OH peak, as well as the least intense -CH_2- peaks, indicating the lowest concentration of methylene bridging. Alongside this, it also possesses the largest peak at 1650 cm^{-1}, which corresponds to the carbonyl functionality (from residual formaldehyde), and less intense and distinct band at 1595 cm^{-1} corresponding to C-C stretches of the aromatic rings, which, in turn, is known to be indicative of a lower level of polymerisation.[139]

Finally, the 2-HMP isomer presents the most distinct aromatic band, indicating that this isomer has the highest level of polymerisation across the three resoles, with this being further indicated by the more distinct shoulder at 1595 cm^{-1}.[139] Despite this, it has

a less intense stretch within the methylene regions, alongside a more distinct peak for the ether region at 1150 and 1125 cm^{-1}, suggesting that there is a higher level of ether bonding present that is produced by the 4-HMP starting material. This is most likely due to the increased reactivity allowing for a higher level of polymerisation, however the *ortho*-position of the hydroxymethyl group kinetically favours the formation of ether bonding, providing a possible explanation as to why this is the most prevalent linkage seen.[105,143]

Overall, three distinct trends have appeared across the investigated resoles. 4-HMP had the highest level of methylene bonding, with the IR spectrum displaying a modest shoulder at 1595 cm^{-1}, and thus a moderate level of polymerisation. 2-HMP, on the other hand, demonstrated a larger extent of polymerisation, however this was mostly in the form of unwanted ether bonding. The resole synthesised with a 1:1 mixture of 2 and 4-HMP indicated the lowest extent of polymerisation, as well as low amount of methylene bonding when compared to ether. As such, mixtures of both isomers were not explored any further.

4.2.2   Effect of Temperature

During the preliminary synthesis detailed in the previous section, it was noted that the temperature was difficult to maintain at 90 °C, with this randomly fluctuating to temperatures as high as 103 °C. This is likely due to the exothermic nature of the addition reaction, with this having the knock-on effect of increasing the evaporation rate of the H_2O by-product.[107]

Due to the highly kinetic nature of the reaction, these two combined produce a runaway effect, making the reaction, and hence the products produced, very difficult to control. In turn, this prevents the reliable replication of the final pre-resin, and by extension, the rheological properties.[107] Hence, because of this, when investigating the use of these oligomers in the binding of CF tape when forming CF-composites, it was opted to both lower, and vary the temperature, in an attempt to provide more control over the kinetics of the reaction.

Following this, it was decided to lower the maximum temperature to 80 °C, as this will reduce the rate at which the polymerisation occurs, and by extension, the amount of excess heat produced. Experiments reported in the literature indicated that reactions performed at 40 °C needed > 4 hours for any appreciable formation to occur. Therefore, 60 °C was chosen as the lowest temperature. Due to constraints with the practical equipment available, this was only able to be done at intervals of 10 °C. However, despite this, some trends still emerged.

Based on comparison of the IR spectra obtained (Figure 48), the shoulder peak at 1595 cm^{-1} for the sample synthesised at 80 °C exhibits the highest degree of polymerisation, regardless of bridging mode. This is to be expected, as due to the kinetic nature of the reaction, a higher temperature will allow for a high level of condensation within a given time frame. This was also reflected in the macroscopic properties, with the resole synthesised at 80 °C showing a large solid fraction of particulate, which is associated with a higher degree of polymerisation. In the same vein, the experiment
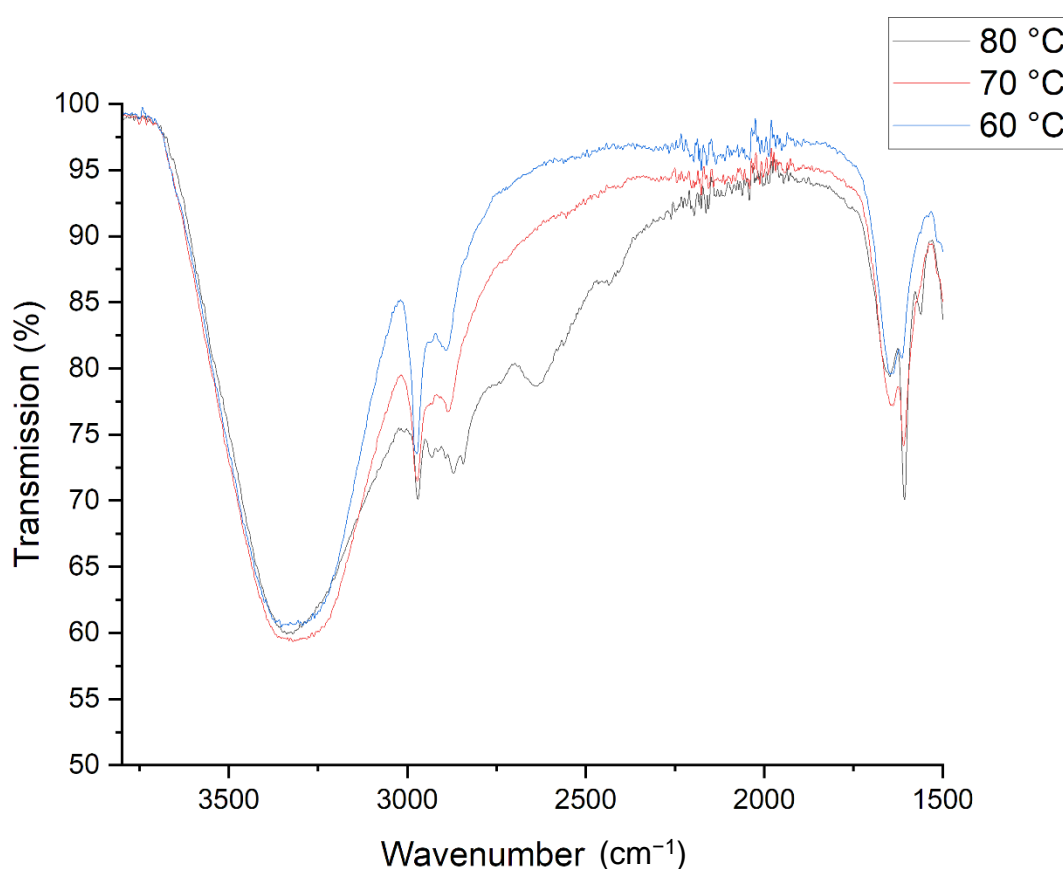
Figure 48: A comparison of the IR spectra obtained from 2-HMP based resole at diffrering temperatures.

performed at 60 °C has the smallest aromatic shoulder in the IR spectrum, and in turn, also possesses the largest peak at 1020 cm^{-1}, which corresponds to the 1° alcohol of the hydroxymethyl group. This is indicative of there being a large proportion of substituted *ortho-* and *para-* positions that have not undergone further condensation to form resole oligomers. This is most likely due to the substitution process of formaldehyde addition being appreciable at lower rates, yet the condensation processes do not become appreciable until higher temperatures. The resole formed at 70 °C was in the middle of these two extremes, and is therefore in keeping with the above analysis. Hence, overall, the temperature showed a slight effect on the type of bridging moiety formed, with the main effect being on the degree of polymerisation.

4.2.3 Effect of Base Concentration

Following the realisation that the reaction temperature had only a minor effect on the bridging mode formed, other potential factors were explored. As the reaction proceeds through a phenoxide intermediate that is produced via deprotonation with a base, the concentration present in the reaction mixture has a direct impact on the speed at which the polymerisation reaction begins. Moreover, as resole chains grow via a step growth mechanism. This has a further impact on the rate at which these chains grow, and, by extension, to what extent the polymerisation process occurs. Hence, it stands to reason that, at a given reaction time and temperature, a lower concentration of base will produce shorter oligomeric chains, providing another avenue of product control. In keeping with the alterations made following the initial investigation into the isomers, these reactions were carried out at 80 °C, and used 2 equiv. of formaldehyde, with the amount of base being varied from 0.20 to 0.60 equivalents. This was done for both the 2-HMP and 4-HMP isomers separately.

2-HMP based resole synthesised with above 0.50 equiv. of base produced a considerable amount of solid particulate, whilst this only occurred at above 0.55 equiv. with the 4-HMP based product under similar conditions. Whilst this posed issues when analysing the samples, as solution-state NMR can't be done on samples that contain solid particles, this still provided evidence of the differing levels of reactivity between the two

isomers, as the formation of solid particles is associated with high molecular weight species.

All samples produced IR peaks at 1150 and 1125 cm^{-1}, as well as 2980 – 2800 cm^{-1}, indicating that both methylene and ether bonds are present across the samples. For both 2-HMP and 4-HMP, the relative intensities of the methylene bands compared to that for ether generally decreased with an increase in the amount of base catalyst, with the maximum being at around 0.3 equiv. Below this threshold, there was a minor difference in the relative levels of bonding modes present. However, there was a distinct difference in the prominence of the aromatic peak at 1595 cm^{-1}, with this being much less distinct at 0.20 equiv. of base, and subsequently increasing in prominence to a maximum around 0.55 – 0.60 equiv. for both 2-HMP and 4-HMP samples. This was also reflected in the ^{13}C NMR spectrum, with 2-HMP based samples showing more intense peaks at $\delta_{iso} \approx 63$ ppm, corresponding to the ether bonding mode, with much smaller peaks at 30 – 35 ppm (methylene), meaning that there is a higher amount of ether bonding present relative to methylene. Moreover, the number of environments for these moieties, which is indicated by the number of peaks present, was much higher for the 2-HMP (Figure 49). This is also

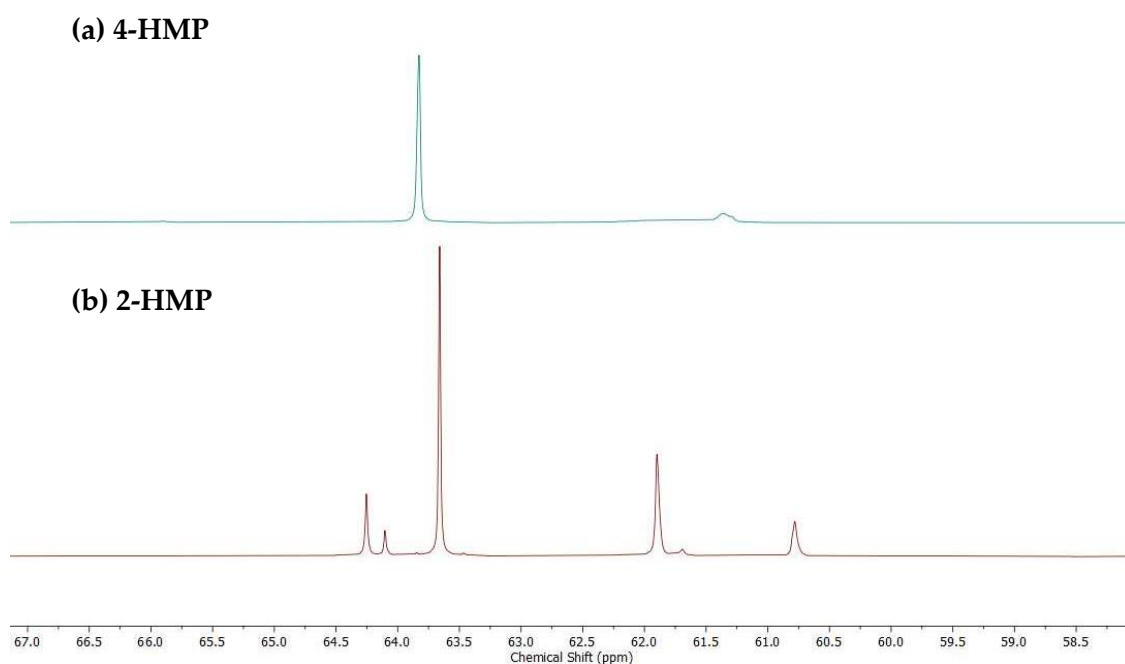*Figure 49: A comparison of the ^{13}C NMR spectra gained for resoles synthesised with both (a) 4-HMP and (b) 2-HMP. Note that the 2-HMP sample produced more numerous, as well as more intense ether peaks. Both of the samples depicted were synthesised using their respective HMP isomer, alongside 0.6 equiv. of NaOH and 2 equiv. for formaldehyde at 80 °C for 30 minutes.*

in line with the macroscopic changes in solid content described above, and is indicative of an overall higher level of polymerisation, irrespective of the bonding modes that caused it.

Interestingly, however, the relative levels of methylene vs. ether bonding was much higher across the 2-HMP based samples than for the 4-HMP samples. This is in contrast to the initial experiments outlined in Section 4.1.1, which showed the opposite trend between the isomers. One difference contrasting these two data sets is the temperature at which the reaction took place, with there being a 10 °C difference between the two. Due to the dominant driver of this reaction being kinetic in nature, this difference in temperature will impact how the overall transformation proceeds, with the level of this effect being dependant on the rate constant of the process, which in turn is reflected by the reactivity. As outlined in the introduction, 2-HMP is better able to undergo condensation at the free benzene positions, with this mechanism, when occurring with a hydroxymethyl group, being responsible for the formation of the methylene bonds. When considering the kinetic favourability of the formation of ether bonding, the lower temperature would hinder the formation of this moiety more than the formation of methylene bridges.[124] This is further compounded by the fact that the free benzyl position on 2-HMP is in the *para-* position, meaning that the condensation on the benzene ring is also more favoured.

Overall, the amount of base present when synthesising the resole was shown to have an effect on the relative amounts of ether and methylene bonds present, with this being true for both isomers. Moreover, it also demonstrated an influence on the amount of polymerisation between monomers of HMP, with this being much more pronounced for the 2-HMP isomer when compared to the 4-substituted isomer.

4.2.4 Effect of Formaldehyde Concentration

In order to ascertain the effect of differing amounts of formaldehyde on the structure of the produced resoles, a series were synthesised at 80 °C, with 0.3 equiv. of NaOH and the formaldehyde content varied from 1 – 2.5 equiv., with this being completed for both isomers. Subsequent analysis of these provided some interesting observations not observed in the other samples. For example, ^{13}C NMR analysis indicates

that resoles synthesised with less than 1.25 equiv. of formaldehyde still possess free *ortho/para* substitution sites.[145] IR analysis highlights a peak at 1650 cm^{-1} that decreases with lower formaldehyde amounts. This is to be expected, as the proportion of free benzene positions will begin to form an excess, allowing for the complete substitution of formaldehyde onto the phenolic ring.

Moreover, this also poses some potentially interesting effects when the resoles are subjected to curing. The free benzene positions noted in the NMR experiments are most likely free *ortho-*, as 2,6-HMP is incredibly reactive, and forms the fully substituted 2,4,6-HMP isomer incredibly quickly. This free position will also have a knock-on effect when samples are curing, as condensation between hydroxymethyl groups and these free positions are responsible for the formation of methylene bonds. As these will form in the cured sample, this is of extra importance to the ultimate aim of pyrolysing the samples to form a CFC network. Hence, reducing the formaldehyde content provides an important avenue of control when finding resoles that will produce the desired properties when making CFC. The overall effect of curing is investigated in the following section.

Samples prepared with just 1 equiv. still had some residual formaldehyde in the resole stage. 2-HMP synthesised examples showed a much higher level of polymerisation when compared with 4-HMP based systems, with aromatic peaks at 1610 and 1595 cm^{-1} being equal in intensity. Also, at these low concentrations of formaldehyde, the 2-HMP based example showed much more intense bands in the methylene region, and weaker ether peaks when compared with the 4-isomer. Interestingly, these bands were of equal intensity when the formaldehyde content was increased to 1.25 equiv., and subsequently beginning to reverse at higher concentrations. This observation is both in keeping with the results observed from other experiments conducted at 80 °C.

Overall, it was determined that a reduction in the formaldehyde content favoured the formation of methylene bridges, with this being particularly pronounced in the 2-HMP isomer. This was accompanied by an increase in the level of polymerisation, again with this being more evident in the 2-HMP isomer.

4.2.5 Effect of Curing

In order to ascertain the effect of the curing regime on the molecular structure of the binding agent, samples of the resoles synthesised for the above tests were subjected to the same regime as that when they were applied to the CF tape. The curing process takes place in two distinct steps: the first cure takes place at 130 °C for 4 hours, followed by a further 2 hours at 260 °C. At both stages, samples were taken for analysis via IR spectroscopy. Due to the high insolubility and chemical resistivity of the fully polymerised solid product, other forms of analysis were unable to be undertaken with the available instrumentation.

Following the first cure, IR peaks corresponding to the methylene and ether groups were both reduced in intensity, and shifted to values closer to their model values. For example, in all of the samples, the aromatic C-C peaks at 1610 cm^{-1} were no longer present, and only sharp peaks at 1595 cm^{-1} were present, indicating that the polymerisation process had been fully completed (Figure 50).[139] This transformation
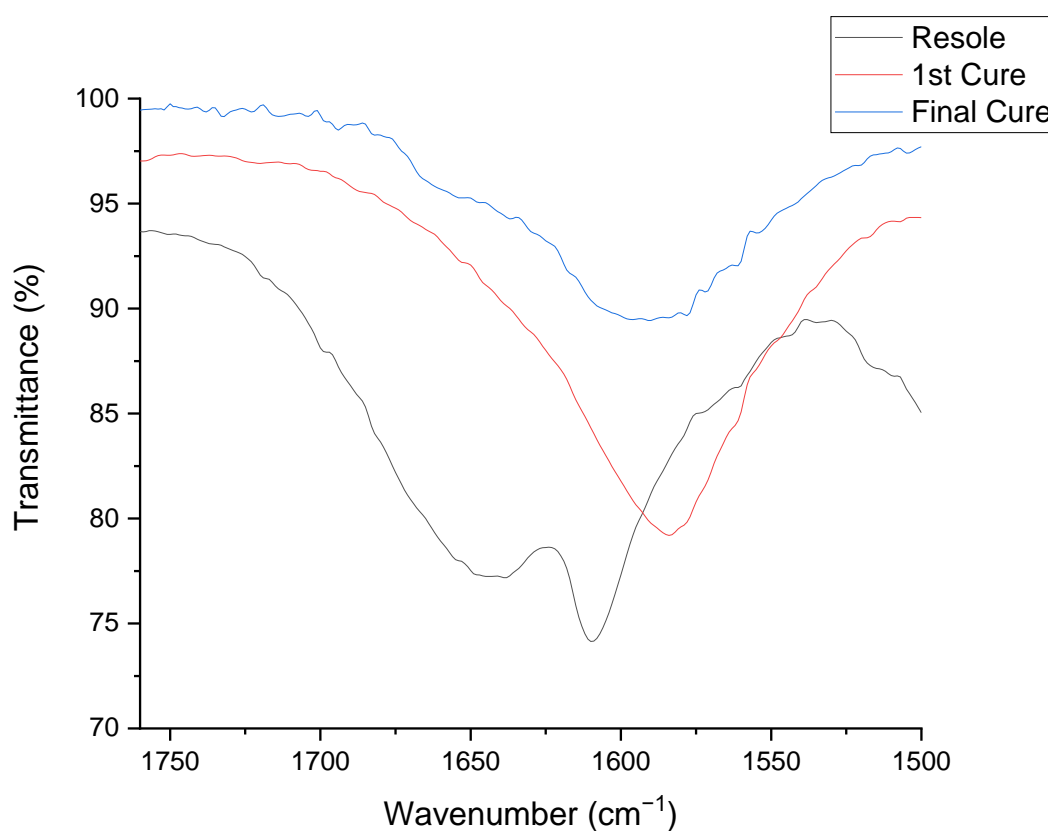

Figure 50: A comparison of the IR spectra obtained from the different curing stages of a resole sample, highlighting the drop in intensity and the shift in wavelength of the aromatic peak. Also shown is the disappearance of the formaldehyde peak at 1650 cm^{-1}. The sample depicted was synthesised using 4-HMP, with 0.6 equiv. of NaOH and 2 equiv. for formaldehyde at 70 °C for 30 minutes.
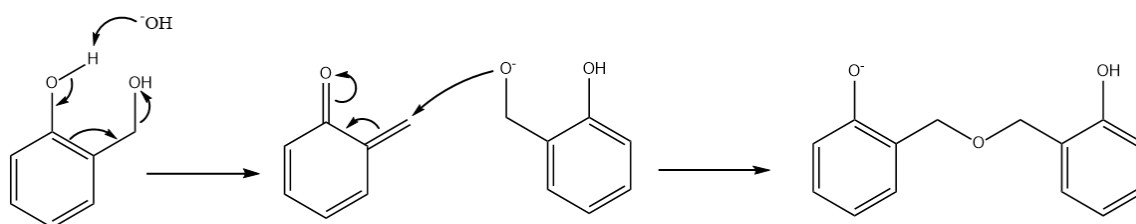
Figure 51: The generally accepted reaction mechanism for the formation of ether bonds via the ortho-quinone-methide structure.[105,106]

fully occurred following the first curing step, even when shorter chained resoles synthesised at 60 °C had been used, indicating that this step is responsible for the completion of the polymerisation process. Interestingly, there were few differences observed between the samples that had only been cured for the first step and fully cured samples, meaning that any chemical differences occurred in the first step. Minor differences were present between the two curing stages. The difference primarily consisted of lower intensity and less defined peaks (Figure 50). Generally speaking, the intensities of all the peaks was lower than for the resoles on their own, and there was a gradual reduction in the number of peaks observed. One such size reduction was observed for the broad peak between $3700 - 3200$ cm^{-1}, which corresponds to the amount of free -OH groups present in the sample. Accordingly, there was a drop in the relative intensity of the methylene stretches when compared to ether stretches at 1150 and 1125 cm^{-1}.

An increase in the relative amount of ether bonds has most likely occurred due to the elevated temperatures. Aside from being kinetically favoured, and therefore being more prevalent at temperatures above ~120 °C, a new reaction pathway becomes available via the *ortho*-quinone-methide species.[105] Based on model compound experiments, this species is believed to play a significant role in systems with *ortho*-hydroxymethyl groups (Figure 51). Whilst this trend was observed in all resoles to varying degrees, this was much more pronounced in 4-HMP samples, which is more likely to have a free *ortho*- substituted hydroxymethyl group. This isomer had free benzene positions that would allow for substitution with formaldehyde leaving a free hydroxy group. 2-HMP on the other hand, already has a hydroxy methyl position in the *ortho*- species. Hence, this would be more likely to have reacted in formation of the resole oligomer.

Interestingly, resoles produced with a reduced level of formaldehyde below 1.5 equiv. also had a less prevalent ether peak when compared to those for methylene. This may be due to the presence of free positions as detected via ^{13}C NMR. This provides further credence to the notion that a reduction in formaldehyde content during the formation of the resole may be beneficial to the final properties of the CFC. In the previous section discussing the effect of base concentration on the resole structure, it was determined that around 0.3 equiv. showed the highest level of methylene bonding. The data that was able to be collected following the curing stages was insufficient to draw any meaningful conclusions on the impact this may have.

Overall, during the curing stages, all of the chemical transformations take place during the initial step at 130 °C, with the second step providing no discernible structural differences. One difference that was noted between samples cured for one step, and those cured at both, were differences in macroscopic properties, with the fully cured samples being more tough and brittle, and hence difficult to grind into a powder. Out of all the samples, those manufactured with a formaldehyde content of below 1.5 equiv. had the least intense ether peaks when compared with those for methylene, as predicted by theoretical considerations. This is most advantageous when forming CFC, as an increase in methylene bonds will be able to form large networks of graphitised carbon.

4.3 CFC MANUFACTURE

In order to try and ascertain whether the resoles synthesised in the previous section would work within their intended role as a binding material, preliminary, *in-situ* tests were undertaken to assess their binding strength when used in conjunction with CF. As outlined in Section 3.3, two layers of CF were placed on top of each other, ensuring that an overlap of 1 cm was present, forming what is often known as a 'lap-joint'. The rheological properties of the resoles, such as high viscosity and level of tac (*i.e.*, 'stickiness') made accurate allocation of specific volumes of glue difficult to achieve. Hence, an excess of the resole was applied in order to ensure that the CF overlap was fully saturated, and that the maximum amount of glue was present. Finally, an external mass of 2 kg was applied to the uncured CF-glue matrix, and allowed to stand overnight. This was done to remove any possible air pockets that could have formed in the viscous

resole mixture, and ensure that all samples possessed the densest possible matrix. Alongside this, a commercial sample of glue was obtained (Graphibond 551-RN) and applied using the same method as outlined for the resole samples synthesised. Due to the semi-solid nature of the commercial glue, samples were diluted with IPA, at proportions of 35, 50 and 70 wt.% to allow for the adequate wetting of the CF strands. Finally, these were then cured according to the 2-step regime outlined in Section 4.2.5, and stressed under tension until failure, giving a measure of their ultimate tensile strength (UTS), quoted in kg. Due to the high cost and turnaround time associated with full stress-strain analysis, this was done using a rudimentary test apparatus. Commercial glue was also tested to provide a comparable benchmark when assessing the strength of the samples produced using the synthesised resoles.

Of the commercial mixes tested and the forces recorded, the highest was 35%V at 257 kg, this indicates that the level of dilution has an impact upon the final strength of the glue. Dilution was achieved using IPA as a solvent, as this has the lowest 3-phase contact angle with CF. Comparing the synthesised resins against the commercially sourced examples, it was found that all of those tested outperformed the commercial samples. The highest recorded was that done with 4-HMP at 70 °C and 0.3 equiv. of NaOH, indicating that a lower base has an impact, as well as lower temperature, as expected. Due to limitations with the test apparatus, strain measurements were unable to be made. As well as this, the maximum force that could be exerted was 500 kg, meaning that some pieces were unable to be stressed to their UTS. Hence, this was unable to be determined. This was further backed up by the fact that experiments completed at 60 °C failed to adhere the CF layers – most likely due to the product possessing short chains and a low viscosity.[107,146] Due to time constraints, more rigours testing was unable to be performed, and is therefore ongoing.

5 Conclusions

Overall, the new design of apparatus presented several issues that needed to be resolved in order to achieve the project aim of being a viable method of manufacturing PCD and other diamond-based materials. Following the initial synthesis of PCD products, it was determined via SEM and Raman analysis that graphitisation of the starting diamond grains was occurring. Subsequent PXRD and IR analysis of the pyrophyllite material used to construct the reaction chamber used in the apparatus confirmed that a loss of pressure was occurring whilst at the 1540 °C reaction temperature. This was identified by the lack of cristobalite present in the two samples, which is a degradation product of coesite, a high-pressure polymorph of SiO_2. This, in turn, evidenced that the pressure achieved during the experiments could not have exceeded 2.5 GPa, and that the conditions were outside of the thermodynamic range required for diamond synthesis. After researching possible causes of this, it was noted that the reaction temperature was in excess of the melting point of the cobalt, which was present as a binding material in the Co-WC anvils, thus causing it to melt and weaken their integrity.

As a result of this finding, the material used to construct the anvils was altered to pure tungsten. Analysis of the reaction chamber used in conjunction with the new anvils indicated the presence of cristobalite, a known degradation product of coesite. Hence, this was taken as preliminary evidence that the pressure achieved using the new tungsten anvils was likely in excess of 2.5 GPa, meaning that higher pressures were achieved relative to the original Co-WC anvils. Whilst this initial testing was conducted, and evidence was found that higher pressures were generated by the new design, further testing and analysis of the PCD material produced by this new design is needed to ascertain its suitability when synthesising diamond-based materials.

Alongside the main investigation into diamond-based materials, further experiments investigating the surrounding CFC anvil framework were undertaken. Overall, it appeared that a lower formaldehyde content is best for our intended use. Other factors such as the amount of base, and different temperatures were also investigated, and found to mainly affect macroscopic properties, such as the viscosity.

Whilst these are still of importance, especially when considering a resins ability to adequately wet the CF strands to form a dense network of glue and fibres, further analysis is needed to deduce any possible effects in relation to the intended role. When these were further used to bond CF strands together, it was found that the UTS achieved by some resins was in excess of 500 kg, outperforming a commercially available competitor by a factor of 2.

6 FUTURE RESEARCH

Based on the findings of the experiments outlined in Section 4, there are many potential avenues for future research. Alongside the troubleshooting of the current shortcomings identified in the apparatus, there is a great deal of potential research in using different binding metals and catalysts when producing PCD. Whilst the current research was briefly discussed in Section 1.6, there are still many potential elements that have yet to be formally screened for their potential use. In addition to this, very little research has been undertaken that utilises techniques such as DSC and TGA in the analysis of the binding materials performance with respect to aspects such as oxidation and graphitisation. These are common failure points of PCD when used in their industrial applications, and whilst there was a recent 2020 study that utilised these techniques when analysing PCD samples,[147] generally speaking, this area is largely unutilised within the literature. Moreover, by combining this with experiments centring on the binding materials themselves, there is considerable scope to gain an understanding of how to construct more resilient PCD materials.

Furthermore, due to the large scope this area possesses, more complete research into the formation of CFC networks using resoles would be incredibly advantageous, not only to the uses outlined in this report, but for many other applications too. With regards to the work put forth here, a more complete understanding of this topic could be achieved by investigating the pyrolysis step, and the effect of the resole composition on the molecular structure and macroscopic properties of the final CFC product. Moreover, there is massive scope to further investigate the use of alternative starting materials in the synthesis of resole resins, alongside optimisation of the reaction conditions. A notable example, is the incorporation of other hetero-atoms, such as boron, into the aromatic system.[91]

Examples found in the literature have shown a multitude of benefits when pyrolysing TR polymer networks to form CFC. For example, this has been shown to improve the ablation resistance (*i.e.*, a resistance to heat) of the final composite.[91,148] This is achieved by preferably binding to the hydroxymethyl site that causes the ether linkage during resin synthesis, thus eliminating this issue.[148] Benefits to the important initial

curing stage identified in this work have also been reported.[105,149] Essentially, as the B-O bond formed in these resins is much stronger than equivalent C-O found in HMP, any oxygen present during the curing process will bond with boron, forming B_2O_3, preventing the usual loss of carbon through emission of volatiles such as CO_2.[150] This is also of further benefit as molten B_2O_3, with a documented melting point of 450 °C, forms a protective film around the unstable graphitised edges helping the formation of the desired extended graphitic matrix.[151,152] This opens up avenues of research into the inclusion of rare-earth boride catalysts, which have long been known to be effective graphitisation catalysts.[153] Moreover, other factors that are well documented in phenolic resins, such as structure-rheology relationships, curing and pyrolysis dynamics and kinetics, how they behave when applied to CF, as well as general reaction optimisation, are much less known.

7 REFERENCES

1   J. F. Healy, *Pliny the Elder on science and technology*, Oxford University Press, Oxford, 1st edn., 1999.

2   J. W. Hershey, *The Book Of Diamonds: Their Curious Lore, Properties, Tests And Synthetic Manufacture*, Hearthside Press, New York, 1st edn., 1940.

3   P. J. Lu, N. Yao, J. F. So, G. E. Harlow, J. F. Lu, G. F. Wang and P. M. Chaikin, *Archaeometry*, 2005, **47**, 1–12.

4   J. F. Healy, *Pliny the Elder*, Penguin Books, Oxford, 2nd edn., 2004.

5   T. Yamanaka and S. Morimoto, *Acta Crystallogr. B*, 1996, **52**, 232–238.

6   F. P. Bundy and J. S. Kasper, *J. Chem. Phys.*, 1967, **46**, 3437.

7   H. T. Hall, *J. Chem. Educ.*, 1961, **38**, 484.

8   C. M. Sung and M. F. Tai, *Int. J. Refract. Metals. Hard. Mater.*, 1997, **15**, 237–256.

9   C. M. Sung and M. Sung, *Mater. Chem. Phys.*, 1996, **43**, 1–18.

10   R. A. Khmelnitskii, *Uspekhi Fizicheskih Nauk*, 2015, **185**, 143–159.

11   T. Tohei, A. Kuwabara, F. Oba and I. Tanaka, *Phys. Rev. B*, 2006, **73**, 064304.

12   H. Kanda, *Braz. J. Phys.*, 2000, **30**, 482–489.

13   R. C. Burns, J. O. Hansen, R. A. Spits, M. Sibanda, C. M. Welbourn and D. L. Welch, *Diam. Relat. Mater.*, 1999, **8**, 1433–1437.

14   T. Evans and Z. Qi, *Proc. R. Soc. A*, 1982, **381**, 159–178.

15   S. S. Li, H. Zhang, T. C. Su, Q. Hu, M. H. Hu, C. S. Gong, H. A. Ma, X. P. Jia, Y. Li and H. Y. Xiao, *Chin. Phys. B*, 2017, **26**, 068102.

16   O. D. Tucker, M. E. Newton and J. M. Baker, *Phys. Rev. B*, 1994, **50**, 15586–15596.

17   G. Davies, *J. Solid State Phys.*, 1976, **9**, L537–L542.

18   M. N. R. Ashfold, J. P. Goss, B. L. Green, P. W. May, M. E. Newton and C. V. Peaker, *Chem. Rev.*, 2020, **120**, 5745–5794.

19   A. T. Collins and P. M. Spear, *J. Phys. D Appl. Phys.*, 1982, **15**, 183–187.

20   S. R. Boyd, I. Kiflawi and G. S. Woods, *Philos. Mag. B*, 1994, **69**, 1149–1153.

21   L. Chen, X. Miao, H. Ma, L. Guo, Z. Wang, Z. Yang, C. Fang and X. Jia, *CrystEngComm*, 2018, **20**, 7164–7169.

22   J. A. Van Wyk and J. H. N. Loubser, *J. Solid State Phys.*, 1983, **16**, 1501.

23   A. T. Collins, *Diam. Relat. Mater.*, 2003, **12**, 1976–1983.

24   J. Walker, *Rep. Prog. Phys.*, 1979, **42**, 1605.

25   S. R. Boyd, I. Kiflawi and G. S. Woods, *Philos. Mag. B*, 1995, **72**, 351–361.

26   W. V. Smith, P. P. Sorokin, I. L. Gelles and G. J. Lasher, *Phys. Rev.*, 1959, **115**, 1546.

27   S. C. Lawson, D. Fisher, D. C. Hunt and M. E. Newton, *J. Phys. Condens. Matter*, 1998, **10**, 6171–6180.

28   K. Iakoubovskii and G. J. Adriaenssens, *J. Phys. Condens. Matter*, 2000, **12**, L77–L81.

29   J. A. Van Wyk, *J. Solid State Phys.*, 1982, **15**, 981–983.

30   A. T. Collins, *Diam. Relat. Mater.*, 2000, **9**, 417–423.

31   Types Of Natural Diamond Classification, http://www.glitteringstones.com/diamondclassification.htm, (accessed 16 May 2020).

32   M. P. Alegre, M. P. Villar, D. Araújo, E. Bustarret, T. Capron, O. A. Williams, G. Ferro and P. Siffert, in *AIP Conference Proceedings*, 2010, vol. 1292, pp. 133–136.

33   Y. N. Palyanov, I. N. Kupriyanov, Y. M. Borzdov and N. V. Surovtsev, *Sci. Rep.*, 2015, **5**, 14789.

34   A. T. Collins and P. M. Spear, *J. Solid State Phys.*, 1983, **16**, 963–973.

35   M. Hasegawa, T. Teraji and S. Koizumi, *Appl. Phys. Lett.*, 2001, **79**, 3068.

36   J. P. Goss, P. R. Briddon and M. J. Shaw, *Phys. Rev. B*, 2007, **76**, 075204.

37   T. Müller, C. Hepp, B. Pingault, E. Neu, S. Gsell, M. Schreck, H. Sternschulte, D. Steinmüller-Nethl, C. Becher and M. Atatüre, *Nat. Commun.*, 2014, **5**, 3328.

38   J. Boardman, in *The Cambridge Ancient History*, Cambridge University Press, Cambirdge, 2nd edn., 1982, pp. 31–32.

39   A. Wainwright, *The Western Fells*, Westmorland Gazette Ltd., Kendal, 1st edn., 1966.

40   J. P. Rafferty, Graphite, https://www.britannica.com/science/graphite-carbon, (accessed 14 May 2020).

41   D. W. Olson, GRAPHITE (NATURAL), https://www.usgs.gov/centers/nmic/graphite-statistics-and-information, (accessed 16 May 2020).

42   L. Boulet-Roblin, D. Sheptyakov, P. Borel, C. Tessier, P. Novák and C. Villevieille, *J. Mater. Chem. A Mater.*, 2017, **5**, 25574.

43   J. Sung, *J. Mater. Sci.*, 2000, **35**, 6041–6054.

44   N. Deprez and D. S. McLachlan, *J. Phys. D Appl. Phys.*, 1988, **21**, 101–107.

45   H. Lipson and A. R. Stokes, *Nature*, 1942, **149**, 328.

46   H. Huang, B. Zhao, W. Wei, Z. Si and K. Huang, *Int. J. Refract. Metals Hard. Mater.*, 2020, **92**, 105312.

47   I. Benedetti and F. Barbe, *J. Multiscale Model.*, 2013, **05**, 1350002.

48   L. P. P. Barreto, M. Mashhadikarimi, M. A. L. O. Rodrigues, D. P. Gurgel, U. U. Gomes, M. Filgueira and R. B. D. Medeiros, *Diam. Relat. Mater.*, 2020, **106**, 107867.

49   H. Jia, H. Ma, W. Guo and X. Jia, *Sci. China Phys. Mech. Astron.*, 2010, **53**, 1445–1448.

50   G. Li, M. Z. Rahim, W. Pan, C. Wen and S. Ding, *J. Manuf. Process.*, 2020, **56**, 400–416.

51   R. B. D. de Medeiros, L. P. de P. Barreto, D. P. Gurgel, M. Mashhadikarimi, R. da Silva Guimarães, M. Filgueira and U. U. Gomes, *Int. J. Refract. Metals Hard. Mater.*, 2021, **99**, 105587.

52   K. Gangwar and M. Ramulu, *Mater. Des.*, 2018, **141**, 230–255.

53   Y. Li, A. J. Bushby and D. J. Dunstan, *Proc. Math. Phys. Eng. Sci.*, 2016, **472**, 20150890.

54   X. Wu, L. Li, N. He, G. Zhao, F. Jiang and J. Shen, *Int. J. Refract. Metals Hard. Mater.*, 2018, **77**, 61–67.

55   R. Bertília and D. De Medeiros, Federal University of Rio Grande Do Norte Technology Centre, 2021.

56   R. B. Little and J. Roache, *Prog. Solid State Ch.*, 2008, **36**, 223–251.

57   F. Giolitti, J. W. Richards and C. A. Rouiller, *The Cementation of Iron and Steel*, McGraw-Hill Book Company, New York, 1st edn., 1914.

58   A. Lavoisier and Translated from French by R. Kerr, *Elements of chemistry: In A New Systematic Order; Containing All The Modern Discoveries*, Printed for T. & J. Swords, New York, 4th edn., 1801.

59   J. B. Hannay, *Nature*, 1894, **49**, 530–530.

60   S. Ferro, *J. Mater. Chem.*, 2002, **12**, 2843–2855.

61   J. E. Field, *The Properties of Natural and Synthetic Diamond*, Academic Press, London, 1993, vol. 28.

62   H. T. Hall, *Rev. Sci. Instrum.*, 1960, **31**, 125–131.

63   Y. N. Palyanov, I. N. Kupriyanov, A. F. Khokhryakov and Y. M. Borzdov, *CrystEngComm*, 2017, **19**, 4459–4475.

64   H. Xie, F. Yin, T. Yu, J. Wang and C. Liang, *Sci. Rep.*, 2014, **4**, 5930.

65   I. C. Lin, C. J. Lin and W. H. Tuan, *Diam. Relat. Mater.*, 2011, **20**, 42–47.

66   H. M. Strong and R. E. Hanneman, *J. Chem. Phys.*, 1967, **46**, 3668–3676.

67   K. E. Spear, A. W. Phelps and W. B. White, *J. Mater. Res.*, 1990, **5**, 2277–2285.

68   B. Xu, J. J. Cui, M. Sen Li, C. M. Li, F. M. Chu and L. M. Feng, *Chin. Phys. Lett*, 2005, **22**, 478–481.

69   L. Chen, X. Miao, X. He, L. Guo, S. Fang, Y. Wang, Z. Wang, C. Fang, H. Ma and X. P. Jia, *J. Cryst. Growth*, 2018, **498**, 67–70.

70   L. Sun, Q. Wu, D. Dai, J. Zhang, Z. Qin and W. Wang, *Sci. China Chem.*, 1999, **42**, 834–841.

71   R. Berman, F. Simon and J. Thewlis, *Z. Elektrochem.*, 1955, **59**, 333–338.

72   P. Atkins and J. De Paula, *Elements of Physical Chemistry*, Oxford University Press, Oxford, 6th edn., 2013.

73   K. J. Dunn and F. P. Bundy, *J. Appl. Phys.*, 1978, **49**, 5865–5870.

74   R. P. Sear, *CrystEngComm*, 2014, **16**, 6506–6522.

75   R. P. Sear, *J. Phys. Condens. Matter*, 2007, **19**, 3.

76   B. Xu, M. Li, L. Li, A. Xu and Y. Niu, *Mater. Sci. Eng.*, 2007, **454–455**, 293–299.

77   Y. P. Xie, X. J. Zhang and Z. P. Liu, *J. Am. Chem. Soc.*, 2017, **139**, 2545–2548.

78   R. S. Bradley, *J. Inorg. Nucl. Chem.*, 1971, **33**, 1969–1973.

79   X. Liu, X. Jia, X. Guo, Z. Zhang and H. Ma, *Cryst. Growth Des.*, 2010, **10**, 2895–2900.

80   D. Turnbull and J. C. Fisher, *J. Chem. Phys.*, 1949, **17**, 71–73.

81   I. Gibson, D. Rosen and B. Stucker, in *Additive Manufacturing Technologies*, Springer New York, New York, NY, 2015, pp. 107–145.

82   O. O. Bochechka, *J. Superhard Mater.*, 2018, **40**, 325–334.

83   J.-H. Chen and C.-H. Chen, in *2009 Fifth International Conference on Intelligent Information Hiding and Multimedia Signal Processing*, IEEE, 2009, pp. 13–16.

84   D. McNamara, P. Alveen, D. Carolan, N. Murphy and A. Ivanković, *Eng. Fract. Mech.*, 2015, **143**, 1–16.

85   J. W. Paggett, E. F. Drake, A. D. Krawitz, R. A. Winholtz and N. D. Griffin, *Int. J. Refract. Metals Hard. Mater.*, 2002, **20**, 187–194.

86   D. McNamara, P. Alveen, S. Damm, D. Carolan, J. H. Rice, N. Murphy and A. Ivanković, *Int. J. Refract. Metals Hard. Mater.*, 2015, **52**, 114–122.

87   A. Kumar Mallik, in *Some Aspects of Diamonds in Scientific Research and High Technology*, IntechOpen, 2020.

88   J. Zhang, F. Liu, J. Wu, Y. Liu, Q. Hu, J. Liu, A. Liang, Q. Wang and D. He, *Rev. Sci. Instrum.*, 2018, **89**, 075106.

89   H. Wang and D. He, *High Press. Res.*, 2012, **32**, 186–194.

90   C. Dong, K. Li, Y. Jiang, D. Arola and D. Zhang, *Opt. Express*, 2018, **26**, 531–543.

91   A. P. Luz, R. Salomão, C. S. Bitencourt, C. G. Renda, A. A. Lucas, C. G. Aneziris and V. C. Pandolfelli, *Open Ceram.*, 2020, **3**, 100025.

92   S. R. Sandler and W. Karo, *Polymer Synthesis: Volume 1 (Polymer Syntheses)*, Academic Press, 2nd edn., 1991.

93   A. Gardziella, L. A. Pilato and A. Knop, *Phenolic Resins: Chemistry, Applications, Standardization, Safety and Ecology*, Springer, 2nd edn., 1999.

94   *Encyclopedic Dictionary of Polymers*, Springer, 1st edn., 2007.

95   M. Chanda and S. K. Roy, *Industrial Polymers, Specialty Polymers, and Their Applications*, CRC Press, 1st edn., 2019.

96   A. Knop and L. A. Pilato, in *Phenolic Resins*, Springer Berlin Heidelberg, Berlin, Heidelberg, 1985, pp. 1–4.

97   P. H. R. B. Lemon, *Trans. Br. Ceram. Soc.*, 1985, **84**, 53–56.

98   P. Sridharan and S. Rajan, *Refract. J.*, 1987, **62**, 10–11.

99   E. V. Krivokorytov, A. G. Gur'ev and B. I. Polyak, *Glass Ceram.*, 1998, **55**, 144–
        147.

100   International plastics flammability handbook - CERN Document Server,
        https://cds.cern.ch/record/290851, (accessed 10 April 2021).

101   R. M. Aseeva and G. E. Zaikov, *Combustion of Polymer Materials*, Hanser Gardner
        Publications, 1986.

102   L. Costa, L. Rossi Di Montelera, G. Camino, E. D. Weil and E. M. Pearce, *Polym.
        Degrad. Stab.*, 1997, **56**, 23–35.

103   J. Gao, Y. Liu and L. Yang, *Polym. Degrad. Stab.*, 1999, **63**, 19–22.

104   A. P. Luz, C. G. Renda, A. A. Lucas, R. Bertholdo, C. G. Aneziris and V. C.
        Pandolfelli, *Ceram. Int.*, 2017, **43**, 8171–8182.

105   K. Lenghaus, G. G. Qiao and D. H. Solomon, *Polymer (Guildf.)*, 2000, **41**, 1973–
        1979.

106   G. G. Qiao, K. Lenghaus, D. H. Solomon, A. Reisinger, I. Bytheway and C.
        Wentrup, *J. Org. Chem.*, 1998, **63**, 9806–9811.

107   N. Kamarudin, D. Radiah, A. Biak, Z. Z. Abidin, F. Cardona, S. M. Sapuan, D. R.
        A. Biak, Z. Z. Abidin, F. Cardona, S. M. Sapuan, D. R. Awang Biak, Z. Zainal
        Abidin, F. Cardona and S. M. Sapuan, *Materials*, 2020, **13**, 2578.

108   G. Bhattacharjee, S. Neogi and S. K. Das, *Int. J. Ind. Chem.*, 2014, **5**, 1–6.

109   X.-M. Hu, Y.-Y. Zhao and W.-M. Cheng, *Polym. Polym. Compos.*, 2015, **36**, 1531–
        1540.

110   A. Cantarero, *Procedia Materials Science*, 2015, **9**, 113–122.

111   D. Tuschel, *Why are the Raman Spectra of Crystalline and Amorphous Solids
        Different?*, 2017.

112   D. S. Knight and W. B. White, *J. Mater. Res.*, 1989, **4**, 385–393.

113 E. J. Di Liscia, F. Álvarez, E. Burgos, E. B. Halac, H. Huck and M. Reinoso, *Mater. Sci. Appl.*, 2013, **04**, 191–197.

114 S. Prawer and R. J. Nemanich, *Philos. Trans. Royal Soc.*, 2004, **362**, 2537–2565.

115 J. W. Ager, D. K. Veirs and G. M. Rosenblatt, *Phys. Rev. B*, 1991, **43**, 6491–6499.

116 G. R. Fulmer, A. J. M. Miller, N. H. Sherden, H. E. Gottlieb, A. Nudelman, B. M. Stoltz, J. E. Bercaw and K. I. Goldberg, *Organometallics*, 2010, **29**, 2176–2179.

117 T. Holopainen, L. Alvila, J. Rainio and T. T. Pakkanen, *J. Appl. Polym. Sci.*, 1997, **66**, 1183–1193.

118 P. Dooling, *UK Community Renewal Fund (CRF) Dyman Advanced Materials*, 2022.

119 W. Betteridge, *Prog. Mater. Sci.*, 1980, **24**, 51–142.

120 L. A. Giannuzzi and F. A. Stevie, *Micron*, 1999, **30**, 197–204.

121 Y. Li, W. Qiu, F. Qin, H. Fang, V. G. Hadjiev, D. Litvinov and J. Bao, *J. Phys. Chem. C*, 2016, **120**, 4511–4516.

122 V. A. Drits, S. Guggenheim, B. Zviagina and T. Kogure, *Clays. Clay. Miner.*, 2012, **60**, 574–587.

123 X. Qin, J. Zhao, J. Wang and M. He, *Minerals*, 2020, **10**, 1–14.

124 T. L. Hicks and R. A. Secco, *Can. J. Earth Sci.*, 1997, **34**, 875–882.

125 M. Luo, Y. Li, S. Jin, S. Sang, L. Zhao, Q. Wang and Y. Li, *Ceram. Int.*, 2013, **39**, 4831–4838.

126 L. Wang, M. Zhang, S. A. T. Redfern and Z. Zhang, *Clays. Clay. Miner.*, 2002, **50**, 272–283.

127 S. Ono, T. Kikegawa, Y. Higo and Y. Tange, *Phys. Earth Planet. Inter.*, 2017, **264**, 1–6.

128 H. D. Holland and K. K. Turekian, *Treatise on Geochemistry*, Elsevier Inc., 2003, vol. 1–9.

129 D. L. Whitney, *Am. Mineral.*, 2002, **87**, 405–416.

118

130   F. R. Barrientos-Hernández, M. Pérez-Labra, A. Lobo-Guerrero, M. Reyes-Pérez, J. C. Juárez-Tapia, J. Hernández-Ávila, E. Cardoso-Legorreta and J. P. Hernández-Lara, *Adver. Mater. Sci. Eng.*, 2021, **2021**, 1–13.

131   L. Wang and Z. Zhang, *Chin. Sci. Bull.*, 1997, **42**, 140–144.

132   J. H. Rayner and G. Brown, *Clays. Clay. Miner.*, 1966, **25**, 73–84.

133   L. Wang, M. Zhang and S. A. T. Redfern, *Clays. Clay. Miner.*, 2003, **51**, 439–444.

134   J. Popović, E. Tkalčec, B. Gržeta, S. Kurajica and J. Schmauch, *Am. Mineral.*, 2007, **92**, 408–411.

135   J. R. Martínez, S. Palomares-Sánchez, G. Ortega-Zarzosa, F. Ruiz and Y. Chumakov, *Mater. Lett.*, 2006, **60**, 3526–3529.

136   J. Lewis, D. Schwarzenbach and H. D. Flack, *Acta Crystallogr. A*, 1982, **38**, 733–739.

137   C. Tan, K. Zhou, W. Ma, B. Attard, P. Zhang and T. Kuang, *Sci. Technol. Adv. Mater.*, 2018, **19**, 370–380.

138   V. Muñoz, P. Pena and A. G. T. Martínez, *Ceram. Int.*, 2014, **40**, 9133–9149.

139   N. Gabilondo, M. Larrañaga, C. Peña, M. A. Corcuera, J. M. Echeverría and I. Mondragon, *J. Appl. Polym. Sci.*, 2006, **102**, 2623–2631.

140   M. B. B. Hocking, in *Handbook of Chemical Technology and Pollution Control*, Academic Press Inc., Oxford, 3rd edn., 2006, pp. 689–712.

141   T. G. Mayerhöfer, A. V. Pipa and J. Popp, *ChemPhysChem*, 2019, **20**, 2748–2753.

142   M. Thébault, A. Kandelbauer, E. Zikulnig-Rusch, R. Putz, S. Jury and I. Eicher, *Eur. Polym. J.*, 2018, **104**, 90–98.

143   J. Si, J. Li, S. Wang, Y. Li and X. Jing, *Compos. Part A Appl. Sci. Manuf.*, 2013, **54**, 166–172.

144   M.-F. Grenier-Loustalot, S. Larroque, D. Grande, P. Grenier and D. Bedel, *Polymer (Guildf.)*, 1996, **37**, 1363–1369.

145   J. Paju, T. Pehk and P. Christjanson, *Proc. Estonian Acad. Sci.*, 2009, **58**, 45.

146   M. Thébault, A. Kandelbauer, U. Müller, E. Zikulnig-Rusch and H. Lammer, *Eur. J. Wood Wood Prod.*, 2017, **75**, 785–806.

147   X. Sha, W. Yue, H. Zhang, W. Qin, D. She and C. Wang, *Diam. Relat. Mater.*, 2020, **104**, 107753.

148   M. O. Abdalla, A. Ludwick and T. Mitchell, *Polymer (Guildf.)*, 2003, **44**, 7353–7359.

149   S. Wang, X. Jing, Y. Wang and J. Si, *Polym. Adv. Technol.*, 2014, **25**, 152–159.

150   S. Wang, X. Jing, Y. Wang and J. Si, *Polym. Degrad. Stab.*, 2014, **99**, 1–11.

151   Y. Zhong, X. Jing, S. Wang and Q. X. Jia, *Polym. Degrad. Stab.*, 2016, **125**, 97–104.

152   S. Wang, C. Bian, B. Jia, Y. Wang and X. Jing, *Polym. Degrad. Stab.*, 2016, **130**, 328–337.

153   A. Ōya and H. Marsh, *J. Mater. Sci.*, 1982, **17**, 309–322.

154   R. T. Downs and D. C. Palmer, *Am. Mineral.*, 1994, **79**, 9–14.